INTRAOPERATIVE BRAIN SHIFT ESTIMATION USING VESSEL SEGMENTATION REGISTRATION AND TRACKING

By

Siyi Ding

Dissertation

Submitted to the Faculty of the

Graduate School of Vanderbilt University

in partial fulfillment of the requirements

for the degree of

DOCTOR OF PHILOSOPHY

in

Electrical Engineering

May, 2011

Nashville, Tennessee

Approved:

Professor Benoit M. Dawant

Professor Michael I. Miga

Professor Reid C. Thompson

Professor Bobby Bodenheimer

Professor J. Michael Fitzpatric

ACKNOWLEDGEMENTS

This dissertation would have been impossible without the great support and assistance from my committee members and colleagues in the Medical Image Processing (MIP) lab and Biomedical Modeling Lab (BML). Many of them have helped me in different aspects and encouraged me consistently throughout all these years to complete this work.

First of all, I would like to express my deepest appreciation to my advisors, Dr. Benoit Dawant and Dr. Michael Miga. Dr. Dawant offered me a great opportunity to study at Vanderbilt University since 2005. From that time, he teaches me image processing techniques, as well as the methodology to deal with research problems. He shows me how to break down the research problems and tackle them one by one, which benefits me most. In the past five years, he spent lots of evenings and weekends to help me on papers. When there are challenges ahead, he always encourages me to try out new ideas. When there are difficulties on the way, he always gives his hand. He is an advisor who advises, a mentor who guides, and a coach who demonstrates using his own behavior. I could not ask for more as a student. Dr. Miga gave me lots of excellent lectures on finite element modeling. This helped me a lot to understand my research problems and backgrounds of our project. He always had good ideas and kept on giving me very valuable suggestions on every weekly meeting, five years in a row. His insights, and dedication to our project, are essentially the cornerstone of this project. It is no doubt that this dissertation will go nowhere without his enthusiasm and guidance.

Special thanks to Dr. Thompson and Dr. Fitzpatrick for their fully support of my research. Without their consistent support, I would have not accomplished this study. Dr. Thompson provided me invaluable data set in this whole world. His hardworking attitude inspired me to work harder and think more. Dr. Fitzpatrick taught me Medical Image Registration course, which is one of the core techniques in this dissertation. What I have learned from him will definitely benefit my whole research career.

Finally, I want to address warm acknowledgement to Dr. Bodenheimer for his great support on my dissertation. One course he taught me, special topics on graphics, truly broaden my horizon. I still remember the nights I spent to accomplish a project involving image segmentation using level sets at my first year. His valuable suggestions since my proposal stage really helped me a lot and I sincerely thank him for his time and advices to me.

I also want to thank for the Harold Sterling Fellowship from the graduate school of Vanderbilt, and NIH Grant #R01 NS049251-01NSF. They helped me financially throughout my life as a graduate student.

Finally, I would like to express my gratitude to my parents. Their infinite love helps me through a lot. I also want to thank my beloved fiancée, Qing Xu, who is always by my side, having faith in me constantly, and encouraging me to achieve more. All of them mean a lot to me. I love them.

Siyi Ding, Mar. 2011

TABLE OF CONTENTS

Page

LIST OF TABLES

LIST OF FIGURES

Figure **Page**

CHAPTER I

INTRODUCTION

The latest review [1] from the National Cancer Institute (NCI) shows that, in the United States, there were approximately 126,329 people (66,622 male and 59,707 female) alive on January 1, 2007 who had brain or other nervous system cancer. The same report also estimated that 22,070 people would be diagnosed with brain cancer in 2009 and that 12,920 of them will die of this disease. Tumor resection achieved during brain surgery is a common technique used in course of treatment. These surgeries can be very invasive and carry a significant risk to the patient. Indeed, malignant structures can be localized in close proximity to sensitive structures such as critical sensory and motor areas or blood vessels. In addition to that, cancerous tissue is not always easily discernible from normal tissue. To address this issue, image-guided systems have been developed over the years in an attempt to assist surgeons to perform complete tumor resection while avoiding touching sensitive areas.

A typical image-guided neurosurgery system (IGNS) presents preoperative images to neurosurgeons in all angles so that they can precisely locate tumor and brain structures and effectively plan the operation to minimize the damage to the brain. Such preoperative images are usually of high quality and hard to acquire during the procedure.

However, it is almost impossible for the patient's head to be in the same orientation in the operating room as it is in the scanner and a substantial amount of brain deformation occurs during the procedure due to the resection itself, loss of Cerebrospinal Fluid (CSF) or the administration of drugs [2-4]. In the medical imaging literature, intraoperative brain deformation is commonly referred to as brain shift. Due to this brain shift, images acquired preoperatively do not accurately represent the state of the brain during the procedure. To take advantage of all the information preoperative imaging provides to the surgical team, these images need to be adjusted to conform to the actual shape of the brain. A number of techniques have been proposed over the years, which will be reviewed succinctly in the next following sections. In this dissertation, we present a set of methods that can be used with a laser range scanner to estimate cortical displacement. These displacements can be used, in turn, to drive mathematical models capable of estimating brain displacement in deeper regions.

1.1. Background on Intraoperative Brain Shift Estimation

A number of imaging techniques have been employed to estimate intraoperative brain shift. These include intraoperative MR (iMR) [12-16], intraoperative Computed Tomography (iCT) [17-20] , intraoperative Ultrasound (iUS) [21-33], stereo imaging [34-37], or Laser Range Scan (LRS) images [38-43]. In this section, these imaging systems are reviewed together with the corresponding computational methods used to estimate brain shift.

1.1.1 Methods developed to estimate brain shift using iMR

Intraoperative MR images can either be acquired by using interventional scanner directly in the operation room (OR) [12-15, 28] or moving patients back and forth between the OR and an adjacent scanning room [16]. Interventional MRs are not only expensive but they also require expensive non-magnetic surgical instruments. In addition, to permit better accessibility to the patients during the operation, open magnets are often used. These scanners typically have poor spatial resolution and the images they generate often suffer from substantial geometric distortions. As a result interventional MRs have not been widely adopted in brain surgeries. The alternative, which is to move the patient out of the OR for scanning, complicates the surgical procedure and introduces up to 10 minutes overhead for each scan. It is also not very commonly used.

Even when intraoperative MR images are acquired, their spatial resolution is often lower than the spatial resolution of standard diagnostic scanners. Registering pre- and intra-operative images is thus advantageous and various algorithms have been developed to achieve this. In [15], the intra- and pre-operative images are aligned by maximizing their Mutual Information (MI) with a rigid transformation. Ferrant et al. [6, 14] proposed a nonrigid surface matching algorithm to track the shift of key surfaces and then further extrapolate volumetric deformation using a linear finite element elastic model. In [13], a block matching algorithm was proposed to estimate a sparse deformation field, and then a dense deformation field was computed by an iterative hybrid method. This method was later extended to preoperative fMRI and DT-MRIs in [15].

1.1.2 Methods developed to estimate brain shift using iCT

The first iCT scanner in the United States was made at the University of Pittsburgh for minimally invasive brain surgery in 1981 [20]. Recently, a mobile CT scanner, equipped with wheels for intraoperative and ICU applications, was developed at Harvard [17]. In 2007, BrainSuite iCT [18], a system integrating Siemens' Miyabi CT scanner with BrainLab's computer-aided surgery equipment, was installed in the United States for the first time. The total investment for fielding this system ranges from 2 to 5 million dollars. It is approximately half of an iMR system but it remains a substantial capital investment, which may not be affordable for the vast majority of the hospitals in the US and over the world.

Recently, a portable low dose intraoperative CT called xCAT ENT [19] has been introduced. The dimensions of the scanner are 32" x 47" x 60", which is smaller than traditional CT scanner, and it is equipped with wheels to be effortlessly rolled into position directly behind the patient's head by one person. It can produce CT images with slice thickness as low as 0.4mm. The scanning time is around 20s for 600 frames and reconstruction time is about 60sec/300 slices with a radiation dose of 57.6mAs. This scanner is good indeed for providing additional guidance for the surgeon with good resolution in a short time but soft tissue contrast is not as good as with diagnostic scanners.

1.1.3 Methods developed to estimate brain shift using iUS

Using ultrasound is much less expensive than using MR, but this usually yields

images with relatively poor quality. To date there are three types of registration algorithms that have been used to register intraoperative ultrasound with preoperative MR images [22, 28, 30, 31, 33].

The first type relies on the image intensity or gradient values. As US tends to enhance the boundaries between anatomical structures, its intensity resembles the gradient more than the raw intensity of MR images. To better associate the intensity of MR with that of US, Roche et al. [32] proposed a similarity metric named the Bivariate Correlation Ratio (BCR), which generalizes the correlation ratio and considers both gradient and intensity information of MR images.

The second kind of method searches for a transformation that maximizes the co-joint probability of voxels being included in hyperechogenic structures in both the preoperative MR and intraoperative US images. The probability map is constructed using both the mean curvature of the preoperative MR image and manual segmentation of the pathological tissues in the MR image. In [23], it has been shown that this method is superior to registration based on mutual information, normalized mutual information, or the correlation ratio. However, the validation was performed on three intraoperative data acquired after opening of the dura and did not involve any tumor resection case. In addition, the requirement of manual segmentation of pathological tissues makes this method difficult to integrate into the clinical flow.

The last but the most common method is to register MR with iUS images based on homologous features [22, 24, 25, 29-31]. In [22] preoperative MR is first registered with iUS image. Then the brain shift was measured by human delineated homologous features such as the falx or tumor boundaries. Reinertsen et al. [31] registered vessels

segmented in preoperative MRA volumes with vessels visible in intraoperative Doppler US images. The authors compared three different registration schemes (1) a rigid registration based on manually selected points, (2) a rigid registration based on vessel points extracted automatically, and (3) a non-rigid registration based on vessels. In the non-rigid registration, a modified ICP approach [45], in which outliers are eliminated through a least trimmed squares approach, is used to establish point correspondence, followed by the estimation of a Thin-Plate Splines (TPS) transformation. It was shown that the non-rigid registration only improves results marginally over the rigid registration, suggesting little deformation occurred between the pre- and intra-operative images in their studies. However, it is not clear whether any of their intraoperative US were acquired after resection, which is the case in our study. The tumor resection introduces large deformations of the cortical surface in our data, which requires the non-rigid registration of images collected before and after tumor resection.

1.1.4 Methods developed to estimate brain shift using stereo images

Nakajima et al. proposed to register preoperative data with intraoperative video images as early as 1997 [45]. In their work, vessels segmented in preoperative MR images were registered to surface vessels visible in the intraoperative video images and the system was tested on images acquired after opening of the dura. Sun et al. extended this approach by using a pair of cameras [37]. They demonstrated the capability of tracking the shape of the cortical surface after opening of the dura on two neurosurgical cases. More recently Delorenzo et al. [34, 35] have used a pair of stereo images and registered them with preoperative images based on a combination of intensity and

manually segmented sulcal features. To correct calibration errors, the registration and camera calibration are performed simultaneously in their algorithm. Their method was applied to patients undergoing stage 1 epilepsy surgery, which only involves the opening of the dura. The more challenging problem, measuring brain shift during tumor resection, is not addressed in their studies. Moreover, to the best of our knowledge, they have not developed any automatic algorithm to extract vessels from those stereo images.

1.1.5 Methods developed to estimate brain shift using LRS

At our institution, a laser range scanner with an integrated high resolution digital camera is used [39-43] to capture the visual appearance as well as the three-dimensional geometry of the brain surface during surgery. Briefly described (more detailed information are provided in Chapter III), the LRS captures a 2D picture of the field of view and a 3D point cloud (i.e., a set of surface points). The scanner also provides a mapping between the two, such that a textured point cloud can be generated. The scanner can also be tracked [46]. This means that a 3D point acquired at time t_1 can be transformed into the coordinate system at time t_2 even if the scanner position changes in the t_1- t_2 interval, as often happens during surgical cases. Tracking brain motion thus only requires establishing a correspondence between points acquired at time t_1 and time t_2. The LRS used in these studies is somewhat unique in that it captures both geometric and intensity information from the object of interest.

Preliminary studies have explored brain shift estimation during craniotomy using LRS data. In [41], several rigid registration methods were applied on phantom data to examine the accuracy and robustness of the proposed framework. Also, registration

performed on one in vivo case has shown the feasibility of acquiring data in the OR with this system. Results indicate that a method called SurfaceMI, which used intensity information, is better than ICP [47] and other point based registration for registration of preoperative MR image to the intraoperative LRS surface.

In the work presented herein, we focus on the registration of intraoperative data acquired at different time instead of registration from preoperative MR image to intraoperative LRS surface. In other words, we have extended our study from craniotomy to tumor resection. In Chapter III, we propose a method to do registration from pre- to post-tumor resection LRS scans. It has been evaluated using ten in vivo data from the OR and shown to lead to an RMS error that is smaller than 1mm.

In addition to the work performed at our institution, Audette et al. [38] also performed 3D non-rigid surface registration on phantom data obtained by LRS. This method requires initial manual alignment of the surfaces, and to the best of our knowledge, it has not been tested on clinical data so far.

A central part of the work presented in this dissertation, is to investigate methods to estimate the large brain shift occurring during tumor resection, mainly via registration of pre- and post-resection data. Preliminary results using intensity-based registration has shown the feasibility of aligning 3D LRS scans via registration of 2D images [42, 43]. However, only one in vivo case with a small tumor resection was tested using this method. With more in vivo data collected, it became apparent that intensity-based registration alone would not work for cases with bigger resections. The main challenges include the hole created by the resection itself, sagging of the brain caused by this hole, some tissue underneath the skull appearing in the field of view after resection, and

bleeding. All these issues modify the appearance of the images. Therefore, methods that rely on extracting homologous features visible in the images need to be developed. In the type of images we deal with, vessels are the most prominent features, so in this dissertation we have developed and tested registration methods based on them.

1.1.6 Brief review of vessel segmentation from optical images

To develop vessel-based registration, it is necessary to have a robust vessel segmentation algorithm. Segmenting vessels from LRS images shares lots of commonalities with segmenting vessels from retinal images in that both LRS and retinal images are optical images, both of them contain vessels with variable width, and both of them suffer from artifacts introduced by lighting conditions. Since no vessel segmentation techniques on LRS images have been reported in literature, a brief review on the segmentation of blood vessels from retinal images is presented here. Briefly described, these methods fall into the following categories: match filtering [49-54], tracking based methods [55-58], multithreshold probing [51, 59], morphology based techniques [60, 61] and clustering [58] or supervised learning method [62-66].

Lalonde et al. tracked a 'twin point' along the vessel boundary within an edge map [56]. Cree et al. tracked the vessel by fitting a two-dimensional physical model of vessel profile to a local region of the vessel [55]. This category of tracking algorithms does not fit well with LRS images since the vessels in the image are not always connected. In fact, they are just parts of different veins, arteries, and capillaries, which happen to appear on the opening of cortical surface and are not necessarily connected to each other.

Some researchers applied supervised learning methods to retinal vessel segmentation. Sinthanayothin et al. [64] used a neural network trained by the backpropagation learning algorithm. Niemeijer et al. [62] trained a k-nearest neighbor classifier to classify the feature vectors constructed from multiscale Gaussian filtering and the original level of green channel image. Staal et al. obtained better results [66] by using ridge profiles and applying a feature selection algorithm. Soares et al. [65] adopted the Gabor wavelet transform to construct a five dimensional feature vector and used Bayesian classifier. Ricci et al. [63] used a line operator to construct a three dimensional feature vector and adopted a support vector machine. Methods of this kind differ in the construction of feature vectors and the choice of classifier, but the main idea remains the same, which is to find the best discriminant features to separate the vessels from the background.

As far as matching filter based methods is concerned, Chaudhuri et al. proposed a directional 2D matched filter as early as 1989 [49]; Koller et al. proposed a nonlinear multiscale line filter based on the second derivative of Gaussian function [52] in 1995. One of the matched filter methods, which utilizes the elongated structure of vessels is called multiscale vesselness filter. This was proposed by Frangi et al. [67], who used the eigenvalues of the image's Hessian matrix to construct a vesselness measurement for each scale. Frangi's idea was inspired by the work of Lorenz [53], and Sato [54], who introduced a 3D multi-scale line enhancement filter to segment curvilinear structures in medical images. The filter is based on the second order directional derivatives of smoothed images using Gaussian kernel at multiple scales with adaptive orientation selection using the Hessian matrix. They demonstrated the segmentation of brain vessels

from MRI/MRA, bronchi from a chest CT, and liver vessels from an abdominal CT using this method. Later this approach has been used and extended by numerous authors (see for instance [50, 68, 69] and others).

The matched filter based method using Hessian matrix is of particular interest for LRS images because it is fast and easy to use. But we noticed that even if LRS images share similarities with retinal images, the vessels in retinal images have much better intensity homogeneity than LRS images. The abrupt intensity change inside the vessel in LRS images, which is caused by reflection of blood, produces fake edges inside the vessels and causes trouble for all the methods that use edge or gradient information. Moreover, since the cortical surface can be very irregular after tumor resection, the lighting will cause more artifacts than what is typically visible in the retinal images, which is always a smooth spherical surface. Part of our work will thus involve developing specific methods that will permit the robust segmentation of LRS images.

1.1.7 Brief review of methods developed to track nonrigid motions

As will become clear in later chapters, automatic registration of LRS images acquired before and after resection is not an easy task even if vessels can be segmented. This is so because the large discrepancy caused by the resection makes finding homologous features automatically extremely challenging. We will solve this problem by using intraoperative video, as the high frame rate in these sequences makes changes between frames smaller and thus it is possible to track these images automatically. The field of image tracking is very large and a complete coverage of the literature published in this area is outside the scope of this dissertation. But, some representative examples

include kernel-based methods such as mean-shift [70], which locate stationary points of a density function given discrete data sampled from that function. Contour-based methods, such as active contours, proposed by Kass et al. [71] are also common. Modified versions of this approach have been used to track non-rigid structures such as blood cells [72] and much attention has been paid to the human heart and the tracking of the left ventricle in both 2D and 3D [73-76]. Another kind of method, i.e., active shape models [77], which incorporates some prior knowledge of the object shape, has been used for motion tracking. For example, to track the silhouette of a walking pedestrian [78], or organs [79]. Some authors even have extended the active shape model to include the modeling of temporal shape variations [80]. Here, since the vasculature we are tracking does not move in specific motion patterns, active shape models do not seem to be a sound approach. As we need to do for the segmentation of vessels in the LRS images, we will develop methods that are adapted to the type of images we are dealing with.

1.2. Goals and Contributions of This Dissertation

The goal of this dissertation is to develop a set of new methods that can be used to estimate intraoperative cortical surface shift through tracked laser range scan (LRS) data and microscope video sequences. This set of methods includes novel vessel segmentation algorithms, new registration methods for pre- and post-resection LRS data and new tracking algorithms for microscope video sequences recorded during a tumor resection surgery. Using the techniques developed in this dissertation, we have built a framework that will allow accurate measurement of brain shift in the operating room.

The contributions of this dissertation are summarized below:

First, we have tested whether it is feasible to register the pre- and post-resection LRS images using manually delineated vessels. Based on this, experiments have been performed to compare a 2D/3D feature-based registration and a 3D feature-based registration. We have shown that the registration of 2D images acquired with a tracked laser range scanner is sufficient to compute the 3D displacement of pixels visible in the images.

Second, a semiautomatic method has been developed to extract homologous vessels in pre- and post-resection LRS images and register them. This reduces human interventions for vessel extraction, and facilitates the feature-based registration method to be used in the OR. Specifically, experts specify pairs of starting and ending points for each vessel segment. Then, an algorithm has been developed to connect those pairs of points quickly and automatically. The computed vessel centerlines, which are homologous features because the selected ending points are homologous, can be well registered using the proposed feature-based registration method.

Third, an automatic segmentation approach has been developed to extract vessels from the intraoperative images, which are then used to register the images. This could eliminate a significant amount of interaction time that is otherwise required to extract the vessels.

Fourth, a method has been proposed and developed to track vessels in a single video sequence obtained from the microscope in the OR. The tracking of video sequences could be used to help relate pre- and post- tumor resection LRS image acquired at large time intervals despite the big differences visible in these images. In turn, this would permit the automatic estimation of cortical shift.

At last, a software program that assists in inter-video tracking has been developed to track multiple intraoperative video sequences. As the shift between video sequences is relatively big and nonrigid, it is still necessary to provide a graphical interface that allows users to give proper human guidance so that high precision tracking can be ensured.

The reminder of this dissertation is organized as follows. Chapter II shows using a 2D approach is preferable than a 3D approach when using vessels extracted from the LRS images. Chapter III presents a semiautomatic method to extract vessels from pre- and post- brain tumor resection laser range scan image. It details the validation of this method for ten patients. Chapter IV proposes a method to extract vessels fully automatically from laser range scan images. Because pre- and post- resection vessels are too different to be registered fully automatically, Chapter V presents a method to collect and track intraoperative video sequences. It also provides a detailed validation study performed on 21 video sequences. Chapter VI addresses the inter-video registration issue. A program has been created to facilitate human interaction for this purpose.

CHAPTER II

ESTIMATION OF INTRA-OPERATIVE BRAIN SHIFT USING A TRACKED LASER RANGE SCANNER

Siyi Ding[1], Michael I. Miga[2], Reid C. Thompson[3], Prashanth Dumpuri[2], Aize Cao[2], Benoit M. Dawant[1]

[1]Vanderbilt University, Department of Electrical Engineering, Nashville, TN, 37212

[2]Vanderbilt University, Department of Biomedical Engineering, Nashville, TN, 37212

[3]Vanderbilt University Medical Center, Department of Neurosurgery, Nashville, TN, 37212

[This manuscript has been published in *Proceedings of the 29th Annual International Conference of the IEEE-EMBS,* Lyon, France, Aug23-26, 2007, pp. 848-851.]

Abstract

Intraoperative brain shift limits the usefulness of image-guided neurosurgery systems (IGNS), which are based on preoperative images. Methods that are being developed to address this problem need intraoperative measurements as input. In this chapter, we present an intraoperative surface shift measurement technique that relies on a tracked 3D laser range scanner. This scanner acquires both 3D range data and 2D images, which are co-registered. We compare two methods to derive displacements at every point in the field of view. The first one relies on the registration of the 2D images; the second relies on the direct 3D registration of the 3D range data. Our results, based on five data sets, show that the 2D method is preferable.

2.1 Introduction

How to measure and compensate for brain shift during surgical procedures is an active area of research in image-guided neurosurgery (IGNS). Studies have shown that the brain could deform more than two centimeters during surgery due to a number of reasons ranging from the procedure itself (e.g. resection), gravity, or the administration of drugs. Deformations of this magnitude greatly reduce the usefulness of IGNS navigation systems, which are based on preoperative images. To address these issues, approaches have been proposed in recent past. These typically involve deforming preoperative images using intraoperative information [7]. At our institution, we rely on finite element models to perform the deformation [81]. The intraoperative displacement of surface points is necessary to guide the deployment of boundary conditions for these models.

Several approaches are possible to compute this displacement, ranging from localizing homologous points during the surgery using a tracked probe to stereo images [2]. In our system, we use a tracked laser range scanner, which provides us with dense data sets [82]. The laser range scanner captures a 2D picture of the field of view and a 3D point cloud. The scanner also provides a mapping between the two, such that a textured point cloud can be generated. The 3D coordinates of any point and its corresponding coordinate in the field of view 2D image can thus be computed. The scanner is also tracked, which means that the 3D coordinates of a point acquired at time t_1 can be related to the coordinates of a point acquired at time t_2 even if the scanner position changes in the t_1-t_2 interval, as is the case in our application. The problem thus consists in establishing a correspondence between points acquired at time t_1 and time t_2. If this correspondence is established, displacements can be computed. In previous work [42, 43] we have reported a method to establish such a correspondence. This method, which relied on an intensity-based non-rigid registration method to register the 2D pictures, is appropriate for cases in which the tumor is small and the majority of the cortical surface remains within the visual field. Based on extensive experience in the operating room, we have realized that many of these assumptions are significantly challenged during neurosurgical cases involving tumor resections.

In this chapter, we present alternative approaches to establish this correspondence and we evaluate the results we have obtained with these approaches on 5 patients.

2.2 Methods

2.2.1. Data acquisition

A high resolution commercial LRS (RealScan3D USB, 3D Digital Inc., Bethel, CT, USA) system is used in this study. The device is capable of generating 500000 points with a resolution of 0.175mm. The 3D position of each point on the scan is calculated via triangulation. At the same time, a digital camera (Canon Optix 400) acquires a texture image (2D picture) with a resolution up to 2592 by 1944 pixels. The texture image and the 3D point cloud are registered. A complete data set thus includes a set of image pixels with coordinates (u, v) and a series of points with coordinates (x, y, z). The (u, v) coordinates of any (x, y, z) point can be computed and vice-versa. Because the density of the point cloud is lower than the pixel density, obtaining x, y, and z coordinates for a pixel typically requires interpolation.

The following protocol, which was approved by the Vanderbilt IRB, was used to acquire data from consented patients. After opening of the dura, the LRS system, which is mounted on an adjustable arm or a monopod, is placed within 20-30 cm of the patient. A pre-resection scan is taken, which takes on the order of 1minute. The system is removed from the field and the procedure proceeds normally. After tumor extraction, a post-resection scan is acquired by moving the scanner back into place above the craniotomy. The scanner is tracked and a digitization stylus is tracked during the whole process by an Optotrak Certus system (NDI, Waterloo, Ontario, Canada). Because the scanner is tracked, the pre- and post-resection positions do not need to be exactly the

same. More details about the data acquisition procedure can be found in [40].

Fig.II.1 shows a patient in the OR with the tracked laser range scanner positioned on the top of the craniotomy. The IREDs used for tracking the device, which are attached to the scanner, are also visible.

Fig.II.1: View of the operating room with the tracked laser range scanner positioned approximately 30cm above the craniotomy.

2.2.2. Registration protocol

Establishing a correspondence between points in the pre- and post-resection scans can be viewed as a registration problem. Several approaches are possible with the data set at our disposal. The first approach is to register the 2D images. Because each of the 2D images is registered to its own point cloud, the 3D displacement of any point within the images can be obtained once the 2D images are registered. Panel (a) of Fig.II.2

schematizes this approach, which has been used in [42, 43]. The second approach is to work directly on the point cloud and to view the problem as a 3D registration problem. This approach has been investigated by Cao et al. [39]. In this work, 3D features were manually identified in the 3D point clouds and registered to each other. Displacements computed at the selected features were then interpolated over the entire 3D point cloud. This approach is schematized in panel (b) of Fig.II.2.

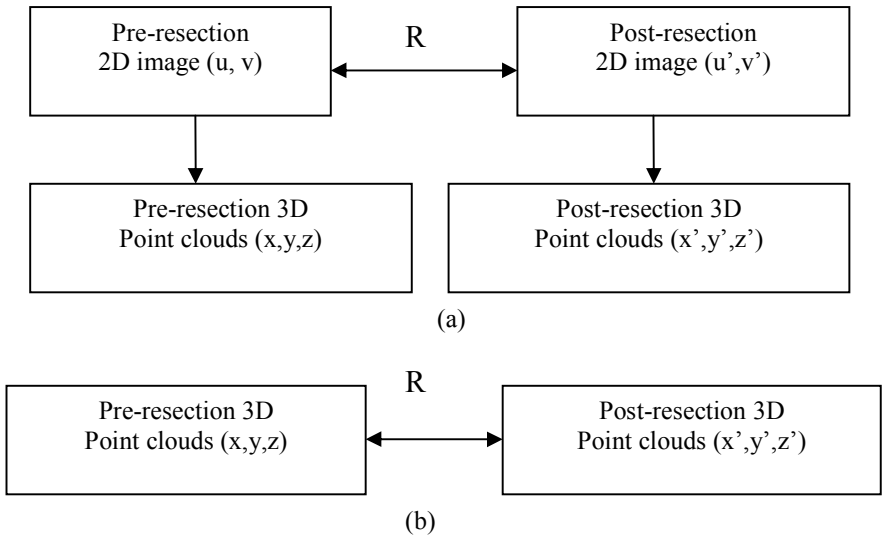

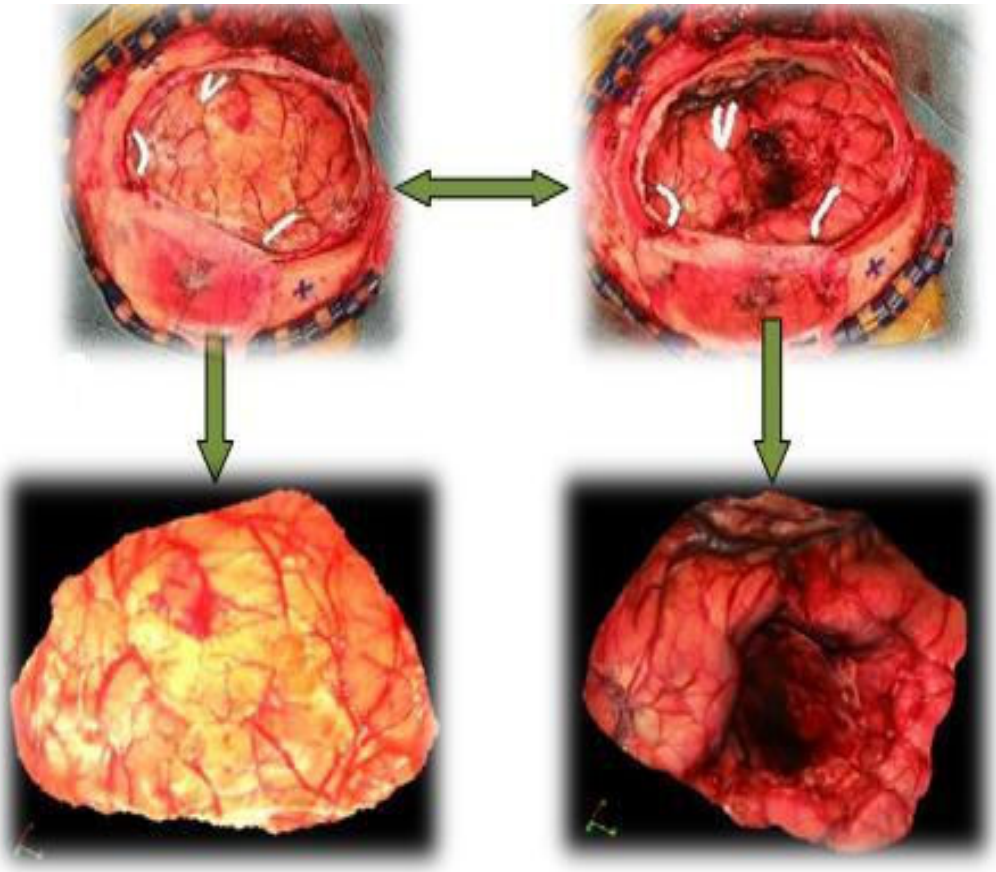

(c)

Fig.II.2: (a) and (b) schematize two approaches that can be used to establish a correspondence between pre- and post- resection scans. Panel (c) shows an actual case. The top two images are the 2D pictures, the bottom two are the textured 3D point clouds.

In the work presented herein, we compare results obtained with the 2D and the 3D approaches. As discussed above, the images included in the current study involve large tumors and therefore large resections, which induce relatively large brain displacements. Because of this, segments of the brain visible in the preoperative images may not be visible in the postoperative images and vice-versa. All these factors make purely intensity-based registration method, such as the one proposed in [48], less robust. Instead, we rely on feature-based methods. First, pre- and post-resection images are brought into rough alignment using a 2D projective transformation computed with four points marked

on the skull around the craniotomy, which are visible in both pre- and post-resection images. Next, vessels are manually delineated in both images (see lines visible in Fig.II.2. (c)). These vessels are then registered to each other using the robust point matching (RPM) algorithm proposed by Chui et al. [83]. This algorithm takes as input two sets of points and iteratively computes a correspondence between these points and the transformation that registers them. The two sets of points do not need to have the same cardinality and the algorithm can deal with the problem of outliers. The transformation computed based on the points is then applied to the entire image volume. As is done in the work of Chui et al., thin-plates splines (TPS) are used as interpolants.

In the 2D approach, the 2D images are registered first. Once this is done, the correspondence between each 2D image and its corresponding point cloud is used to compute 3D displacements at every point. Finally, deformed textured surfaces (3D point clouds) are generated. Because 3D coordinates are known for points on an irregular grid, 3D displacements are interpolated using the FastRBF toolbox developed by FarField technology [84].

In the 3D case, the 3D coordinates of the manually selected points are first computed (interpolation is also required here) and the two sets of 3D points are registered using the 3D version of the RPM technique. The transformation computed in this way is applied to the entire 3D texture surfaces.

2.3. Experiments and Results

Five data sets have been acquired according to the protocol described above.

Tumor size for these cases ranged from 2.8cm^3 to 193.4 cm^3. In each case, vessels were manually delineated in both the pre- and post-resection images. Representative post-resection image with delineated vessels can be seen in Fig.II.3. The 2D and 3D registration methods were then applied to these data sets.

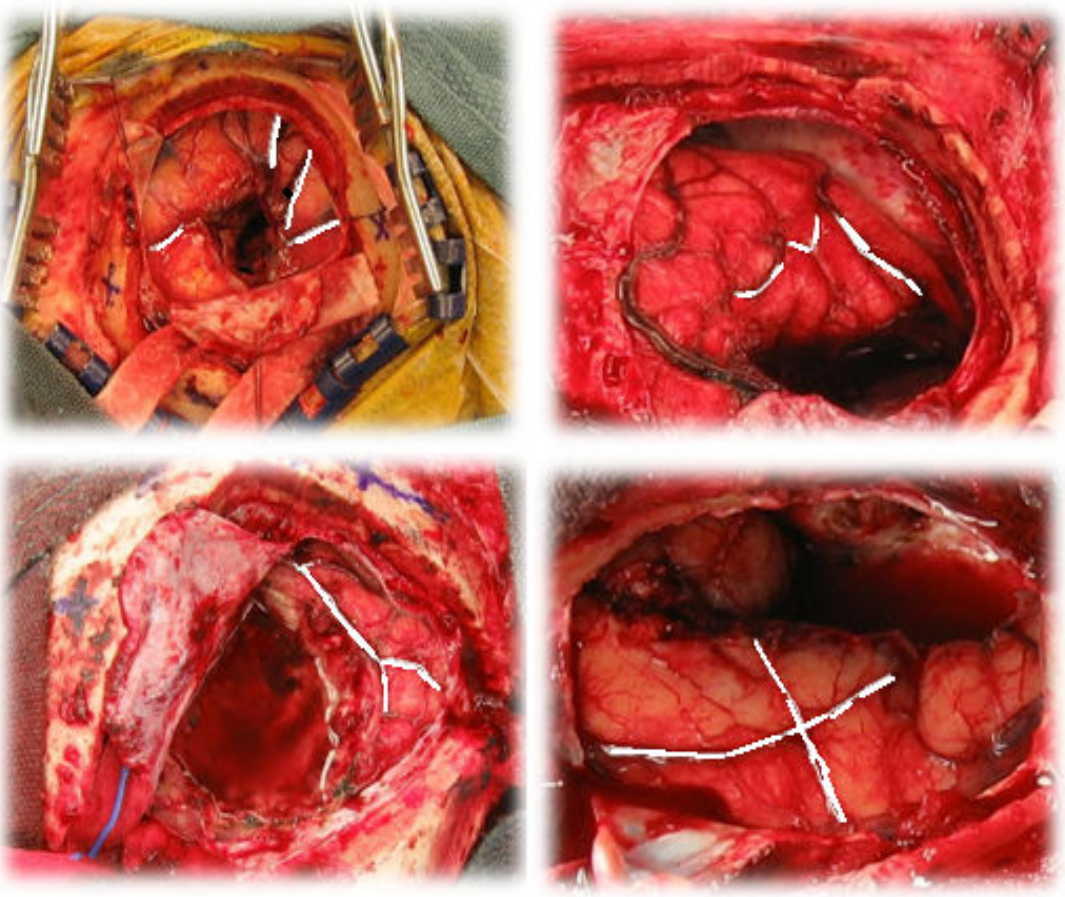

Fig.II.3: Representative post-resection image with delineated vessels.

Fig.II.4 illustrates qualitatively the type of results that were achieved. Panel (a) shows the pre- and post-resection textured surface (top surface and bottom surface, respectively). This figure illustrates both the overall brain sag that has occurred between the two acquisitions and the void left by the resection (the intrusion visible in the middle of the bottom surface). Brain sag in this case, which is not unusual, is on the order of 8-

15mm.

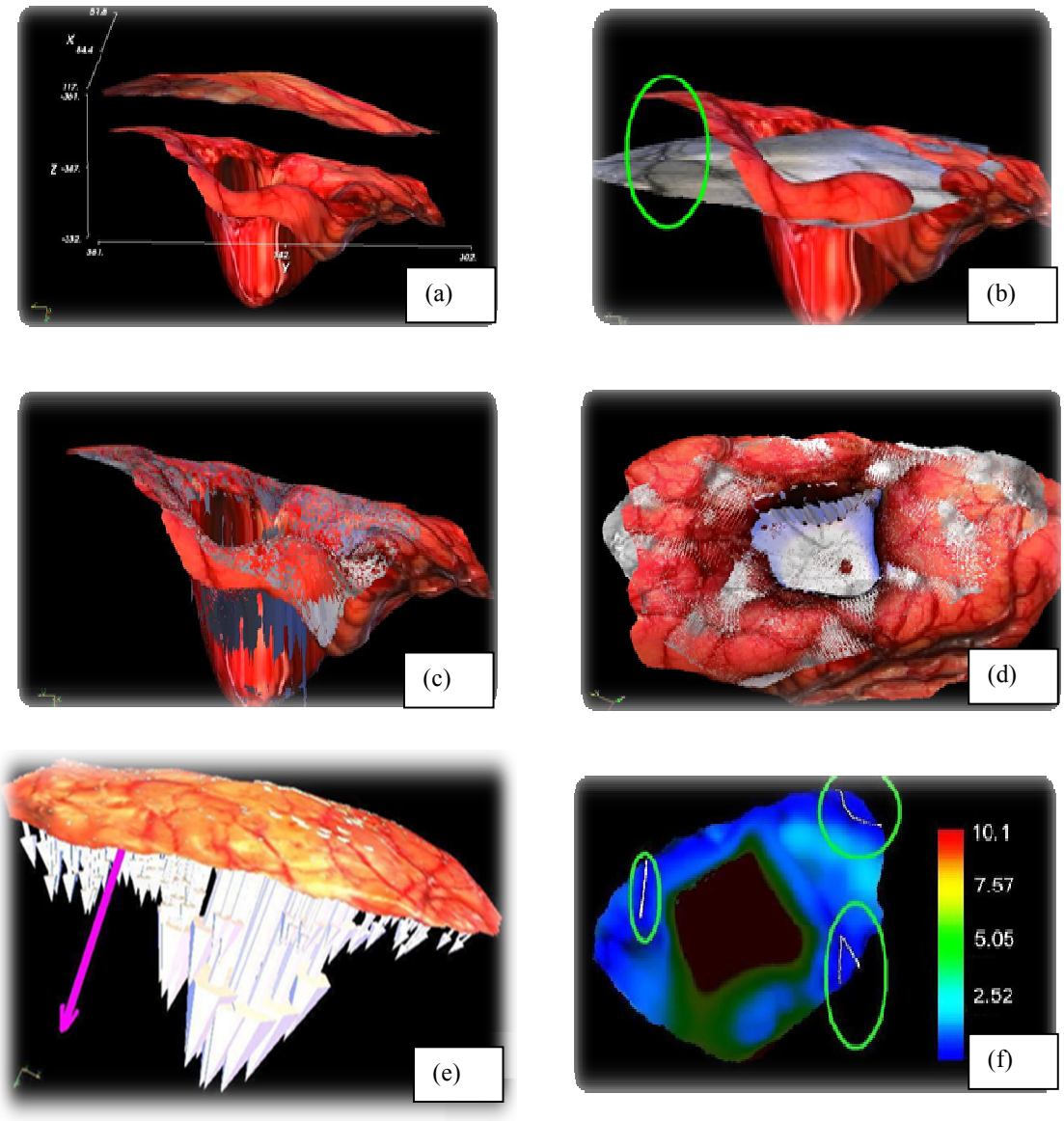

Fig.II.4: Panel (a) shows the pre- and post- LRS (after tumor resection) in the same physical space. Panel (b) shows the registration result using 3D method. Panel (c) shows the registration result using 2D method. Panel (d) shows the same as panel (c) but view from a different angle. Panel (e) shows the deformation field of the 2D method, and the purple arrow represents the gravity direction. Panel (f) shows the difference between the two deformation fields` magnitude map.

Panels (b) and (c) show the final registration results obtained with the 3D and the 2D methods, respectively. In both cases, the pre-resection texture surface has been registered to the postoperative textured surface. The pre-resection surface has been colored in gray to facilitate visualization. Panel (d) shows the same thing as panel (c) but

from a different angle.

Focusing on panels (b) and (c), it is apparent that the 2D approach produces results that are superior to those obtained with the 3D approach. Panel (e) shows the displacements vectors computed with the 2D approach. In this plot, the length of the arrows is proportional to the computed displacements; their direction is derived from the computed deformation field. The direction of gravity is shown with the gray arrow. These results are consistent with previously reported brain shift studies that show that the majority of the displacement occurs in the direction of gravity [85].

Panel (f) shows the difference in the magnitude of the displacements computed with the 2D and the 3D approaches. The lines drawn on the figure are the vessels that were used for computing the registrations. In this figure a light shade of gray indicates a larger value than a darker shade. As expected the displacement difference is zero at the vessels but is substantial away from the vessels (up to 10 mm).

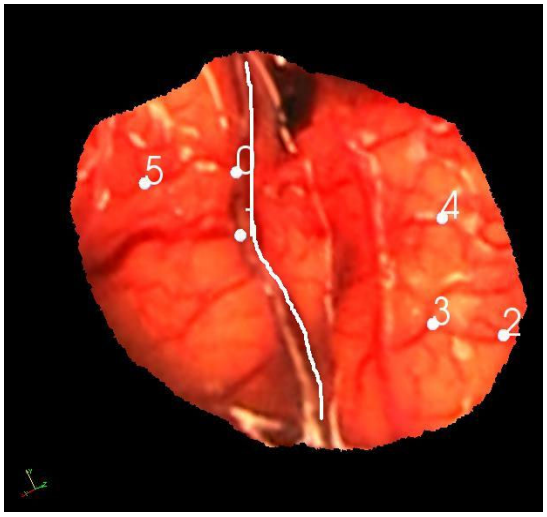

Fig.II.5: Brain shift and target points

To quantitatively test and evaluate both approaches, a number of homologous points have been selected manually on each pair of images. Typically, these point sets

consist of vessel bifurcations that could be visualized in the images. The number of points selected for each pair of images ranged from 6 to 11, depending on the vessels that could be seen. When possible, the points were selected such that they would cover the entire field of view. Fig.II.5 shows one example in which six points have been selected. The figure also shows one of the vessels that were used to compute the registration. For each pair of images the Euclidean distance between the homologous points after registration was computed and averaged, and defined as Target Registration Error (TRE)[86]. The results we have obtained with the five set of test images are reported in Table.II.1. This table also reports the average displacement computed at the points with the 2D method.

Table.II.1: Comparison of TRE

Patient#	Number of target points	Estimated average shift	TRE(mm)	
			3D RPM	2D RPM
1	6	22.4	5.4	3.2
2	6	14.7	3.0	2.7
3	6	1.9	0.2	0.2
4	6	3.1	1.1	1.0
5	11	13.8	3.3	2.7
Mean± STD	7± 2.2	9.6± 8.6	2.6± 2.0	1.9±1.2

2.4. Discussion

It may appear counter-intuitive that a 2D method produces more accurate results than a 3D method. The difference between the two approaches is caused by the interpolation method that is used. In both cases, registration is computed based on sparse

features (lines drawn in the images). The transformations computed with these sparse features are then applied to the entire field of view. When the 2D approach is used, images (2D pictures) are registered and displacements are computed using the associated 3D point clouds. More formally, (u. v) -> (u', v') => (x, y, z) -> (x', y', z'). The point (x', y', z') is obtained by interpolating the 3D point cloud locally. As a consequence, this point falls on the textured surface. In the 3D case, the situation is different. The 3D coordinates of the vessels are used to compute the transformation. This 3D transformation is then applied to the entire field of view to create a transformed textured surface. Therefore, displacements away from the features used to compute the transformation can be arbitrary. The 2D registration approach is thus more constrained than the 3D one, which explains its superior performance.

Our results show that intraoperative brain shift can be very substantial and that preoperative images need to be transformed to provide surgeons with reliable information. Results we have obtained with the tracked laser scanner approach indicate that this is a viable solution, but the method still requires a fair amount of user interaction to identify homologous structures. In the following chapters, we present methods aiming at automating the process. This is, however, a challenging problem because of the large difference between the pre- and post-resection images.

CHAPTER III

SEMIAUTOMATIC REGISTRATION OF PRE- AND POST- BRAIN TUMOR RESECTION LASER RANGE SCAN DATA: METHOD AND VALIDATION

Siyi Ding[1], Michael I. Miga[2], Jack H. Noble[1], Aize Cao[2], Prashanth Dumpuri[2], Reid C. Thompson[3], Benoit M. Dawant[1]

[1]Vanderbilt University, Department of Electrical Engineering, Nashville, TN, 37212

[2]Vanderbilt University, Department of Biomedical Engineering, Nashville, TN, 37212

[3]Vanderbilt University Medical Center, Department of Neurosurgery, Nashville, TN, 37212

[This manuscript has been published in the *IEEE Transactions on Biomedical Engineering,* vol. 56, pp. 770-780, Mar. 2009.]

Abstract

This chapter presents a semi-automatic method for the registration of images acquired during surgery with a tracked laser range scanner (LRS). This method, which relies on the registration of vessels that can be visualized in the pre- and the post-resection images, is a component of a larger system designed to compute brain shift that occurs during tumor resection cases. Because very large differences between pre- and post-resection images are typically observed, the development of fully automatic methods to register these images is difficult. The method presented in this chapter is semi-automatic and only requires the identification of a number of points along the length of the vessels. Vessel segments joining these points are then automatically identified using an optimal path finding algorithm that relies on intensity features extracted from the images. Once vessels are identified, they are registered using a robust point-based nonrigid registration algorithm. The transformation computed with the vessels is then applied to the entire image. This permits to establish a complete correspondence between the pre- and post- three-dimensional LRS data. Experiments show that the method is robust to operator errors in localizing homologous points and a quantitative evaluation performed on 10 surgical cases shows submillimetric registration accuracy.

3.1. Introduction

How to measure and compensate for brain shift during surgical procedures is an active area of research in image-guided neurosurgery (IGNS). Studies have shown that the brain could deform more than two centimeters during surgery due to a number of

reasons ranging from the procedure itself (e.g. resection), loss of cerebrospinal fluid (CSF), or the administration of drugs. Deformations of this magnitude greatly reduce the usefulness of standard IGNS navigation systems, which are based on preoperative images. To address these issues, approaches have been proposed, which rely on biomechanical models to predict the deformation of intraoperative images during the procedure, as a low-cost alternative to intraoperative magnetic resonance imaging [5-11]. But, all of these methods require some type of intraoperative brain movement measurements as input.

Methods, which have been proposed to estimate brain movement intra-operatively include intraoperative MR images [12, 13], ultrasound [28, 30, 31], stereo images [34, 37], or laser range scanners [38-43, 46]. Intraoperative MR images can either be acquired with interventional scanners, which are in the operating room [12, 13], or by moving the patient to an adjacent room in which the scanner is located [16]. Large fixed-coil interventional MRs are expensive, require special equipment, and limit surgeons' access to the operating field [28]. Smaller open magnets typically suffer from poor resolution and geometric distortions. Because of this, it is unlikely that this type of intraoperative imaging will become widely available. An alternative is to build operating rooms adjacent to the scanning room. During the procedure, the patient can be moved back and forth between the rooms and scans acquired. This, however, complicates the procedure and can add up to 10 minutes for each scan [16]. Ultrasound (US) is a cheaper solution but it suffers from relatively poor image quality. Nevertheless it has been used by several groups to register pre- and intra-operative images (see for instance [28, 30, 31],[22, 87]). In [28], the authors estimate brain shift around the tumor by computing a rigid body

registration between the tumor delineated in the preoperative MR volume and in 3D US volumes acquired before and after opening of the dura but prior to resection. Reinertsen et al. [31] rely on vessels segmented in preoperative MR angiography volumes and in vessels visible in intraoperative Doppler ultrasound images. The authors state that two US volumes are acquired. The first one prior to opening of the dura and the second one during the procedure but no details are provided on whether or not these images were acquired after resection. The authors compare registration results obtained with (1) a rigid body transformation computed with points selected manually, (2) a rigid body transformation computed with vessel points extracted automatically in the MR and US images, and (3) a non-rigid transformation computed with the vessel points. To compute the non-rigid transformation, they use a modified iterative closest point approach [47], in which outliers are eliminated through a least trimmed squares approach. Once correspondence is established, thin-plate splines are used to compute the transformation. Results show that the non-rigid transformation improves things only marginally over the rigid-body transformation computed with manually selected points, thus suggesting that in the data set used in that study little deformation happened between the pre- and intra-operative images. Video images have been proposed to register pre- and intra-operative data as early as 1997 by Nakajima et al. [45]. In this work, vessels segmented in preoperative MR images were registered to surface vessels visible in the intraoperative video images and the system was tested on images acquired after opening of the dura. This approach was extended by Sun et al. [37] who used a pair of cameras. They demonstrate their ability to track the shape of the cortical surface after the opening of the dura on two neurosurgical cases. A similar approach is followed by Skrinjar [36]. More

recently, DeLorenzo et al. [34, 35] have used a pair of stereo images and they register preoperative images with intraoperative video images using a combination of sulcal and intensity features. They propose a method by which registration and camera calibration are performed simultaneously and they show that this approach permits to correct calibration errors. In this work, sulcal grooves were segmented by hand and the system was applied to patients undergoing stage 1 epilepsy surgery. This is a procedure, which requires the opening of the dura for the placement of an array of intracranial electrode on the surface of the brain but it does not require resection. At our institution, a tracked laser range scanner with an integrated high resolution digital camera is utilized to capture the visual appearance as well as the three-dimensional geometry of the brain surface during surgery. Briefly described (more detailed information are provided in [40]), the tracked laser range scanner captures a 2D picture of the field of view and a 3D point cloud (i.e., a set of surface points for which the x, y, and z coordinates are known). The scanner also provides a mapping between the two, such that a textured point cloud can be generated. The 3D coordinates of any point and its corresponding coordinates in the field of view 2D image can thus be computed. The scanner is also tracked, which means that the 3D coordinates of a point acquired at time t_1 can be related to the coordinates of a point acquired at time t_2 even if the scanner position changes in the t_1- t_2 interval, as happens often during surgical cases. Tracking brain motion thus only requires establishing a correspondence between points acquired at time t_1 and time t_2. If this correspondence is established, the 3D spatial coordinates of a point at time t_1 and its spatial coordinates at time t_2 can be obtained, which permits computing its 3D displacement.

As discussed above, a number of methods have been proposed to measure brain

shift during surgery but, to the best of our knowledge, none of these methods have been extensively evaluated on data sets acquired before and after tumor resection. Clinical evaluation has been largely limited to measuring cortical or tumor shift following craniotomy or opening of the dura. Although difficult, this is considerably less challenging than attempting to measure shift during the case after resection because resection creates a void, which, in turn, substantially alters the shape of the brain. Because parts of the brain sag to fill in the void, portions of the brain not visible in the pre-resection images can enter the field of view and become visible in the post-resection images. Parts of the brain visible in the pre-resection images can also slide under the skull and become obscured in the post-resection images. Bleeding, which changes the contrast of the images further complicates the task. Due to these difficulties, methods proposed so far to measure intraoperative brain movement are unlikely to succeed. For instance, simply tracking the surface of the cortex to measure sagging or bulging does not provide information on the displacement of the points parallel to the cortical surface. The resolution of US images only permits identifying relatively large vessels. As discussed by Reinertsen et al.[30, 31], this leads to transformations that are accurate close to these large vessels but less so further away from the vessels, thus suggesting the need for intraoperative imaging techniques that have the spatial resolution required to visualize small cortical vessels. Intensity-based methods as the ones we have proposed in earlier work [42, 43] are also not robust enough to deal with the very large differences observed in clinical images.

To address these issues, in Chapter II we have proposed a method based on manually delineated vessels and its potential was shown on a limited number of cases.

Here we expand on this work. As others have done [30, 31, 45], we use vessels to register the images but our work differs in several important ways. First, we use a tracked laser range scanner that provides us with simultaneous high resolution 2D and 3D information. DeLorenzo et al. [35] have shown the importance of on-line calibration when using stereo cameras. The algorithm they proposed achieve this but is time-consuming (more than 20 min. on a modern PC). Our approach does not require on-line calibration. Second, we use a semi-automatic method for the extraction of the vessels in the image. This method is inspired by work of Wink et al. [88]. In this approach vessels are enhanced using the vesselness filter proposed by Frangi et al. [67]. A minimum cost path is then found between starting and ending points given by users. Wink et al. used a multi-scale search method to follow vessels with a constant width. We use a scalar cost function based on maximal vessel response but we add a term that favors paths that are in the center of the vessels as suggested by Bitter et al. [89]. This method is fast, robust to user input error, and permits identifying large and small vessels over the entire field of view. Speed and robustness are important because the system will need to be used by surgeons under time pressure in the operating room. Third, we use the robust point matching algorithm proposed by Chui and Rangarajan [83] to match the vessels as opposed to a modified iterative closest point approach proposed by [47]. Finally, we validate our approach on 10 intraoperative tumor resection data sets. This is a unique data set in which optically tracked pre- and post-resection 2D and 3D information has been acquired.

The rest of the chapter is organized as follows. Section 3.2 describes the methods and presents the data used in the study. It concludes with a description of the validation

methods used to evaluate our approach. Results obtained on 10 tumor resection cases are presented in Section 3.3. Conclusions and suggestions for future work are detailed in Section 3.4.

3.2. Method

3.2.1. Data and data acquisition protocol

A high resolution commercial LRS (RealScan3D USB, 3D Digital Inc., Bethel, CT, USA) system is used in this study. The device is capable of generating 500,000 points with a resolution of 0.15mm-0.2mm at the approximate range used during neurosurgery. The 3D position of each point on the scan is calculated via triangulation. At the same time, a digital camera (Canon Optix 400) acquires a texture image with a resolution up to 2592 by 1944 pixels. The texture image and the 3D point cloud are registered. A complete data set thus includes a series of points with coordinates (x, y, z) with a corresponding set of image pixel coordinates (u, v).

The following protocol, which was approved by the Vanderbilt Institutional Review Board, was used to acquire data from consented patients. After opening of the dura, the LRS system is placed within 20-30 cm of the patient using an adjustable arm or a monopod. A pre-resection scan is taken, which takes on the order of 1-2 minutes including setup. This includes moving into the field, collecting the data, and withdrawing

from the field. After tumor extraction, a post-resection scan is acquired by moving the scanner back into place above the craniotomy. Because the scanner is tracked, the pre- and post-resection scan positions do not need to be exactly the same. More details about the data acquisition procedure can be found in [40].

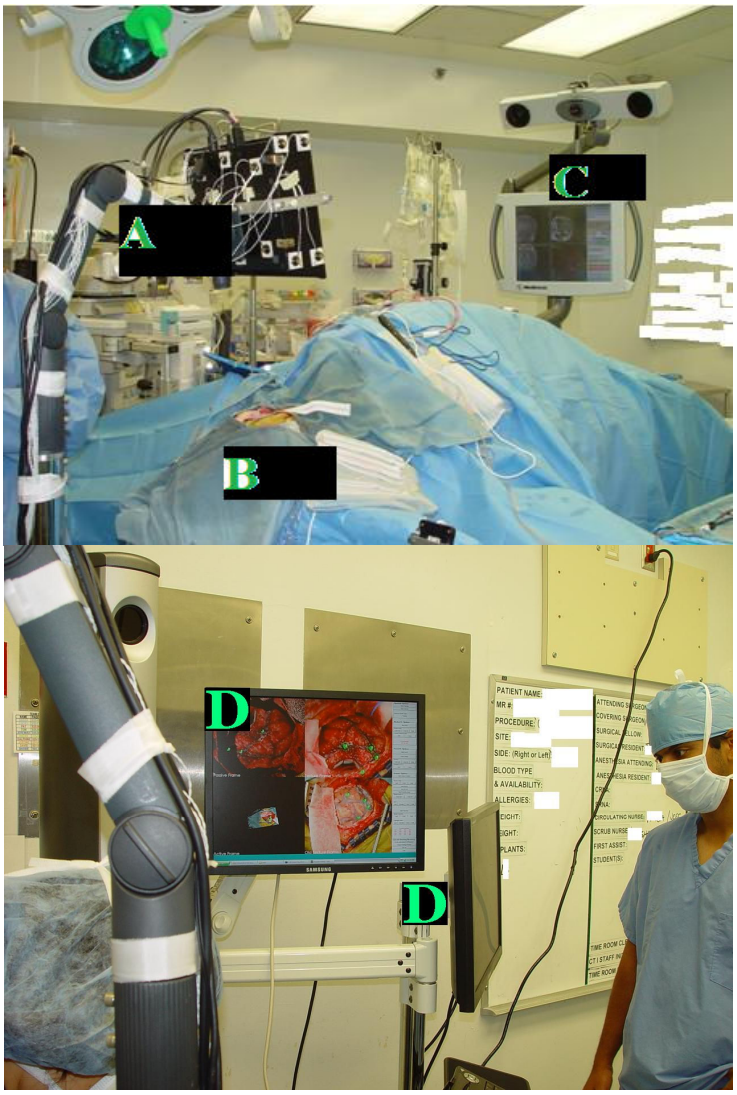

Fig.III.1: The top panel shows the tracked laser range scanner (A) positioned on top of the patient (B). The traditional IGNS system (C) can be seen on the right of the image. The bottom panel shows the user interface (D) developed in house to permit data collection.

The first image in Fig.III.1 shows a patient (B) in the OR with the tracked laser range scanner (A) positioned on the top of the craniotomy. The traditional IGNS (C) can

be seen on the opposite side of the scanner. The second image in Fig.III.1 shows the panel we have developed (D) for data collection and processing.

Fig.III.2, which shows typical pre- (left panels) and post-resection (right panels) images, illustrates the complexity of the task at hand. In this figure, the top panels are the 2D digital images of patient #2 acquired with the camera and the bottom panels are the textured point clouds, i.e. the 3D surfaces acquired with the laser scanner. Pre- and post-resection images are acquired with the scanner in a different position and orientation, and the resection has created a large hole in the middle of the image that induces substantial brain deformation. Blood and the lighting conditions also change the appearance of the images. Additionally, the brain shifts with respect to the craniotomy during the procedure. As a consequence, parts of the brain visible in the first image slide under the skull and are hidden in the second image. The same phenomenon makes parts of the brain hidden under the skull in the first image appear in the second.

3.2.2. Extraction of the vessels centerline

Fig.III.2 suggests that the most reliable features that can be extracted from the pre- and post-resection images are the centerlines of these vessels. Preliminary results presented in Chapter II also suggest that registration based on these features leads to accurate results. But in Chapter II, the centerlines were extracted manually. This is both lengthy and inaccurate. Here the process is largely automated with a method based on a minimum-cost path algorithm [90]. This algorithm requires the computation of a cost matrix, performed automatically, and the manual selection of one starting and one ending

point for each vessel segment to be used for registration. The next section describes the method used to create the cost matrix.

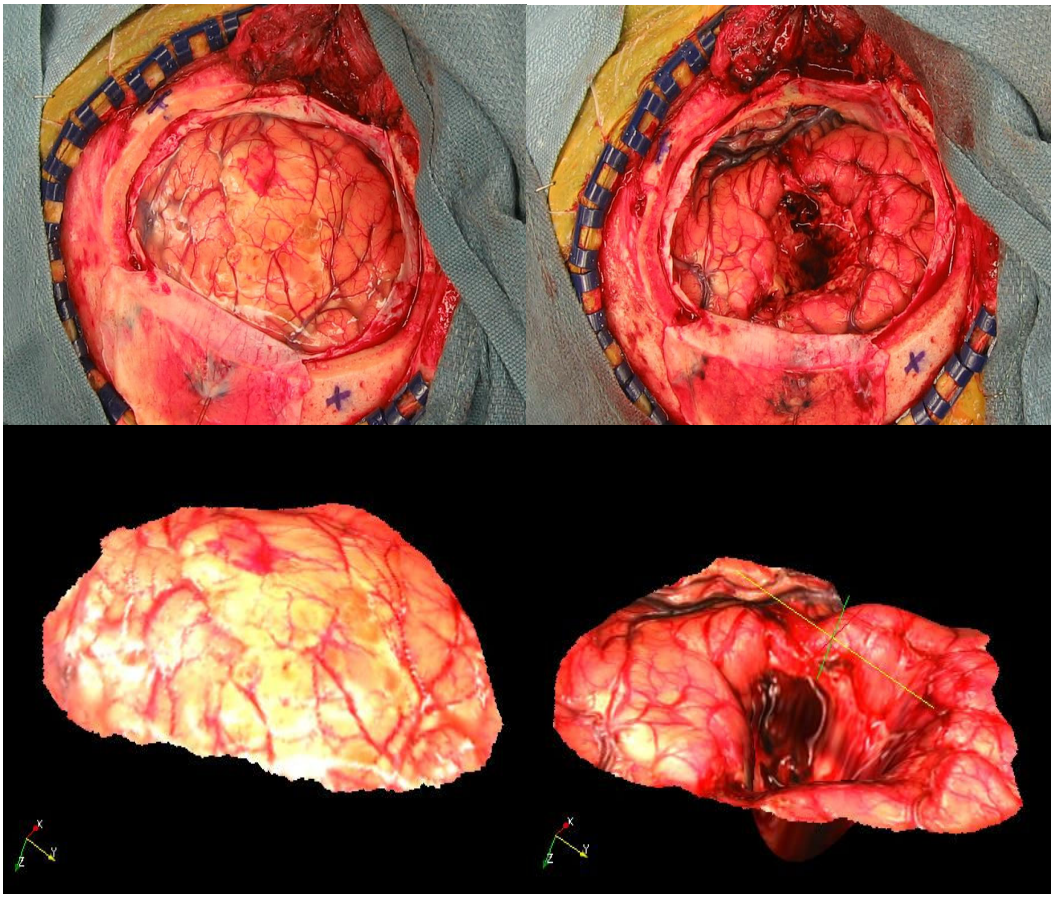

Fig.III.2: Representative example of a pre- and post-resection image pair. The top panels are the 2D images, the bottom panels are the textured point clouds of patient #2 reported in the study.

3.2.3. Creation of the cost matrix

The cost matrix determines the minimum cost path and is computed using two terms derived from the images. The first one is related to the vesselness of a point in the image as defined by Frangi et al. [67]. The second one is based on a distance map

computed on an edge image. In their work, Frangi et al. propose a multi-scale filter based on the Hessian of the image used to enhance tubular structures. The approach they proposed is to (1) convolve the image with Gaussian filters with various standard deviations, (2) compute the Hessian of the smoothed images, defined as

$$\nabla^2 I(x) = \begin{bmatrix} I_{xx}(x) & I_{xy}(x) \\ I_{yx}(x) & I_{yy}(x) \end{bmatrix} \tag{1}$$

with I_{ij} the second spatial derivative of the image in the *i* and then *j* directions, and (3) compute the eigenvalues of the Hessian. An analysis of the eigenvalues determines the type of structure a particular pixel belongs. Pixels, which pertain to tubular-like structures that are bright on a dark background, will satisfy the following conditions:

$$\begin{cases} 0 \approx |\lambda_1| << |\lambda_2| \\ \lambda_2 < 0 \end{cases} \tag{2}$$

Based on this observation, the vesselness filter, Frangi et al. proposed, is as follows:

$$V(i,j) = \begin{cases} 0 & \text{when } \lambda_2(i,j) > 0 \\ \exp(-\frac{\lambda_1(i,j)^2}{2\lambda_2(i,j)^2\beta^2})(1-\exp(-\frac{\lambda_1(i,j)^2 + (\lambda_2(i,j))^2}{2c^2})) \end{cases} \tag{3}$$

The first term in this equation is large when λ_1 is small and λ_2 is large. The second term, which is called the "second order structureness", is large for non-background pixels. To detect vessels of various dimensions, the filter is applied to images that have been convolved with Gaussian filters whose standard deviation is changed from small to large. The vesselness filter responds to small vessels in an image blurred with a Gaussian filter with a small standard deviation. It responds to large vessels in an image

blurred with a Gaussian filter with a large standard deviation. The coefficient β and c are chosen experimentally. Here, these were chosen as 0.5 and 0.05 of the maximum intensity value in the image, respectively. In this application, six standard deviations are used, ranging from one pixel to six pixels and the cost term associated with the vesselness feature is defined as:

$$C_v(x,y) = \sum_{k=1}^{6} w_k V_k(x,y) \tag{4}$$

in which the value of the weight w_k is -0.5 for the standard deviation that produces the largest response and zero for all the others.

Fig.III.3 shows typical results obtained with this approach. The input image is shown in the top left panel; the cost image is shown in the top right panel. While the vesselness filter clearly enhances the vessels, the figure also shows that the centerline of the vessels is not localized precisely. The filter also responds to structures that are not vessels. To address this issue, a second term is added to the cost matrix. First, an edge image is computed using a canny edge detector, then a distance map is computed from the edge image. In this distance map, intensity values are zero on the edges and increases when moving away from the edges. The middle left panel in Fig.III.3 shows the edge image. The distance map image is shown in the middle right panel; in this image, darker intensity values correspond to larger distances. To better visualize the distance term of the cost function, the bottom left panel shows the distance map masked by a binary map obtained by thresholding the vesselness image using threshold 0.96.

The overall cost matrix is computed as

$$C(x,y) = C_v + w_d D(x,y) \tag{5}$$

in which w_d is equal to -0.5. The Canny edge detector of MATLAB 7.0 (The MathWorks, Inc., Natick, MA) was used in which the high threshold is selected automatically depending on image characteristics. The low threshold is set to 0.4 times the high threshold. The overall cost matrix thus weighs equally the vesselness and the distance features. The resulting cost image is shown in the bottom right panel of Fig.III.3. As this image shows, the centerline of the vessels tends to correspond to pixels with the lowest intensity values.

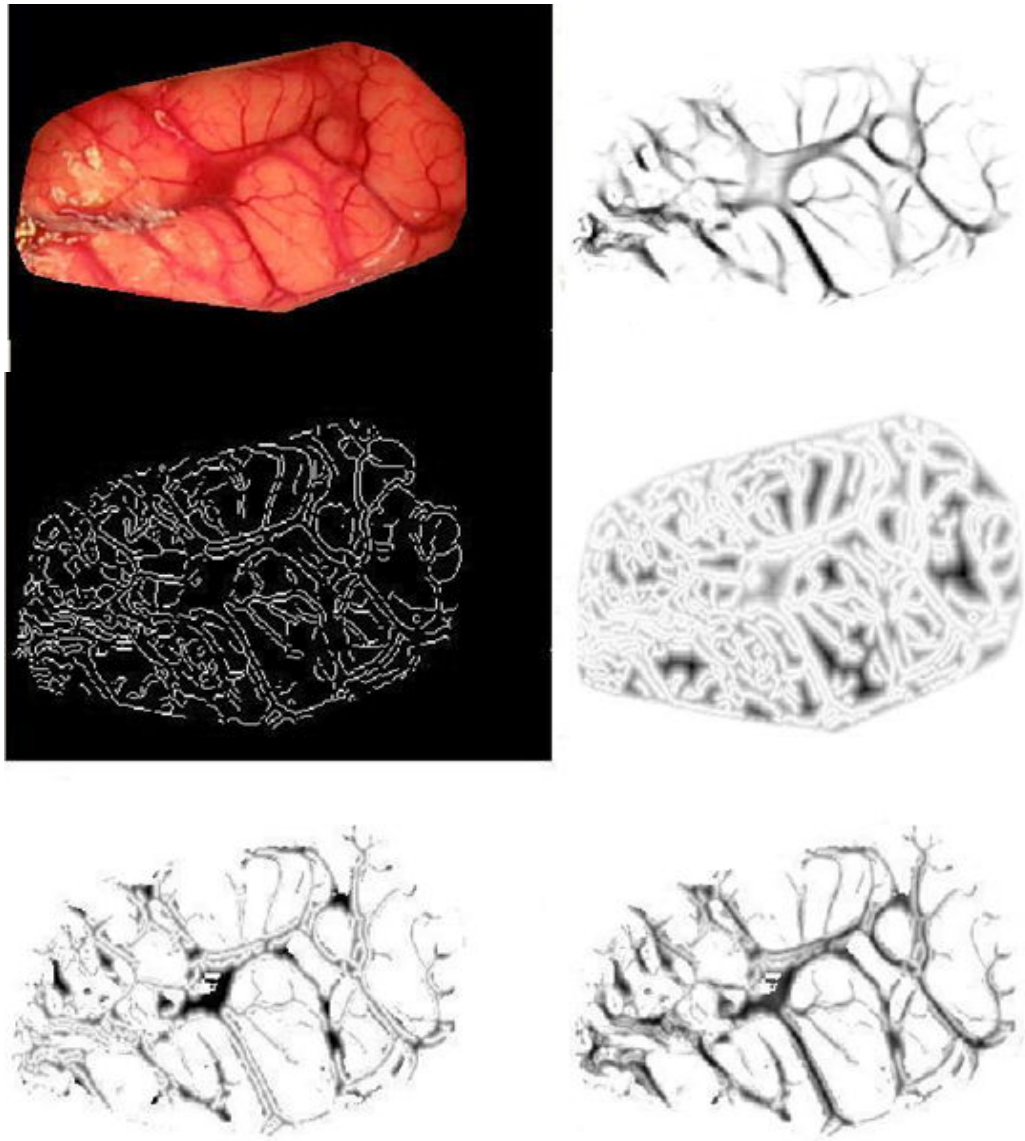

Fig.III.3: Illustration of the cost matrix used to find vessels. The top left panel shows the original image of patient #7 reported in the study. The top right panel shows the vesselness image. The middle left panel is the edge map. The middle right panel shows the distance map computed from the edge map. The bottom panel left shows the distance map masked by a vessel mask obtained by thresholding the vesselness image using threshold 0.96. The bottom right panel shows the final cost matrix.

3.2.4. Centerline extraction

Vessel segmentation is then achieved semi-automatically. A graphical user interface has been developed, which permits visualizing pre- and post-resection images side-by-side. Roughly homologous starting and ending points are localized for vessel segments visible in these images by the end user. When a pair of starting and ending points has been identified, the minimum-cost path between these points is computed automatically using Dijkstra's shortest path algorithm [90].

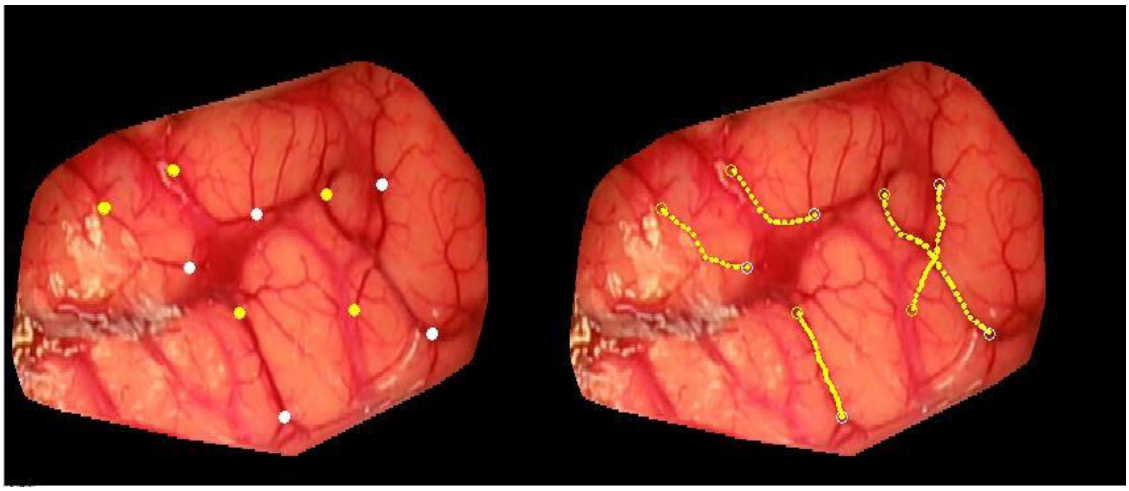

Fig.III.4: This shows an example of centerlines extraction from a pre-resection image of patient #7. Yellow and white point on the left image are starting and ending points, respectively. The computed centerlines are shown in yellow on the right panels.

Fig.III.4 illustrates the process. The left panel shows one of the images acquired with the system (the cortical surface has been manually extracted from the original images). The selected starting and ending points are shown in yellow and white, respectively on the left panel. The vessels extracted by the minimum cost path algorithm are shown on the right. In its current state, the system requires the user to select one pair of starting and ending points at a time. When the pair is selected, the vessel segment that joins them is computed. Computation of an optimal path between a starting and an ending

point takes less than one second on a 3GHz Intel Core 2 Duo Machine. The process is repeated until vessel segments that cover the useable portion of the image are segmented. This figure also shows that the method can be used to segment large or small vessels. Experiments have shown that vessels as small as 0.175mm in diameter can be extracted.

3.2.5. Vessel registration

Once vessels have been segmented, they are non-rigidly registered. This is done with the robust point matching proposed by Chui and Rangarajan [83] and their MATLAB implementation [91] was used. This algorithm alternates between a fuzzy assignment step and a registration step to register point sets. Here, all the vessel centerlines detected in the previous step form two sets of points (one set of points in the pre-resection image and the other in the post-resection image). Each point in one of the sets, say set two is assigned to one or several points in the other set. Once the assignment is done a transformation that registers the points in set two to the corresponding points in set one is computed. If a point in set two is assigned to more than one point in set one, a virtual point computed as the weighted centroid of these points is used to compute the transformation. The fuzzy assignment is computed with the softassign algorithm proposed by Gold et al. [92]:

$$m_{ai} = \frac{1}{T}\exp\left(-\frac{(x_i - f(v_a))^T (x_i - f(v_a))}{2T}\right) \tag{6}$$

in which $V : \{v_a, a = 1,2,...,K\}$ and $X : \{x_i, i = 1,2,...,N\}$ are the two sets of points. $\boldsymbol{f}$ is the transformation used to register the two sets of points. T is called the temperature

parameter, which is introduced to simulate physical annealing. Following the recommendations given in [92], an initial value of 0.5, which is reduced from iteration to iteration, is used here. Thus, equation (6) establishes a fuzzy correspondence between points in set $\boldsymbol{V}$ and points in set $\boldsymbol{X}$. Because the value of T decreases over time, the fuzziness of the assignment decreases as the algorithm progresses. The major advantage of this fuzzy assignment is that it permits handling data sets with different cardinality and it also permits to handle outliers. At each iteration, after the correspondence is determined, a thin-plate spline based non-rigid transformation $\boldsymbol{f}$ is computed, which solves the following least squares problem:

$$\min_{f} E(f) = \min_{f} \sum_{a=1}^{K} \left\| \mathbf{y_a} - f(\mathbf{v_a}) \right\|^2 + \lambda \iint \left[\frac{\partial^2 f}{\partial x^2} + 2\left(\frac{\partial^2 f}{\partial x \partial y}\right) + \frac{\partial^2 f}{\partial y^2} \right] dxdy \tag{7}$$

in which $\mathbf{y_a} = \sum_{i=1}^{N} m_{ai} \mathbf{x_i}$ can be considered as a virtual correspondence for v_a. λ is a regularization parameter, the value of which is changed over time. The algorithm starts with a transformation that is very smooth (heavily regularized). As the algorithm evolves and correspondence improves, the regularization constrain λ is progressively relaxed.

3.2.6. Overall registration procedure

Fig.III.5 illustrates the overall process used to register the pre- and post-resection images and to compute the brain shift that has occurred during the procedure. In this figure, the top panels show the images, as acquired with the LRS. As seen before, these

images contain more than the cortical surfaces. The four points visible on the skull (black crosses) are fiducial points drawn on the skull by the neurosurgeon. These are used to compute a projective transformation to initialize the process; this transformation is called $\boldsymbol{T_I}$. The cortical surfaces are then extracted manually and shown in (c) and (d).

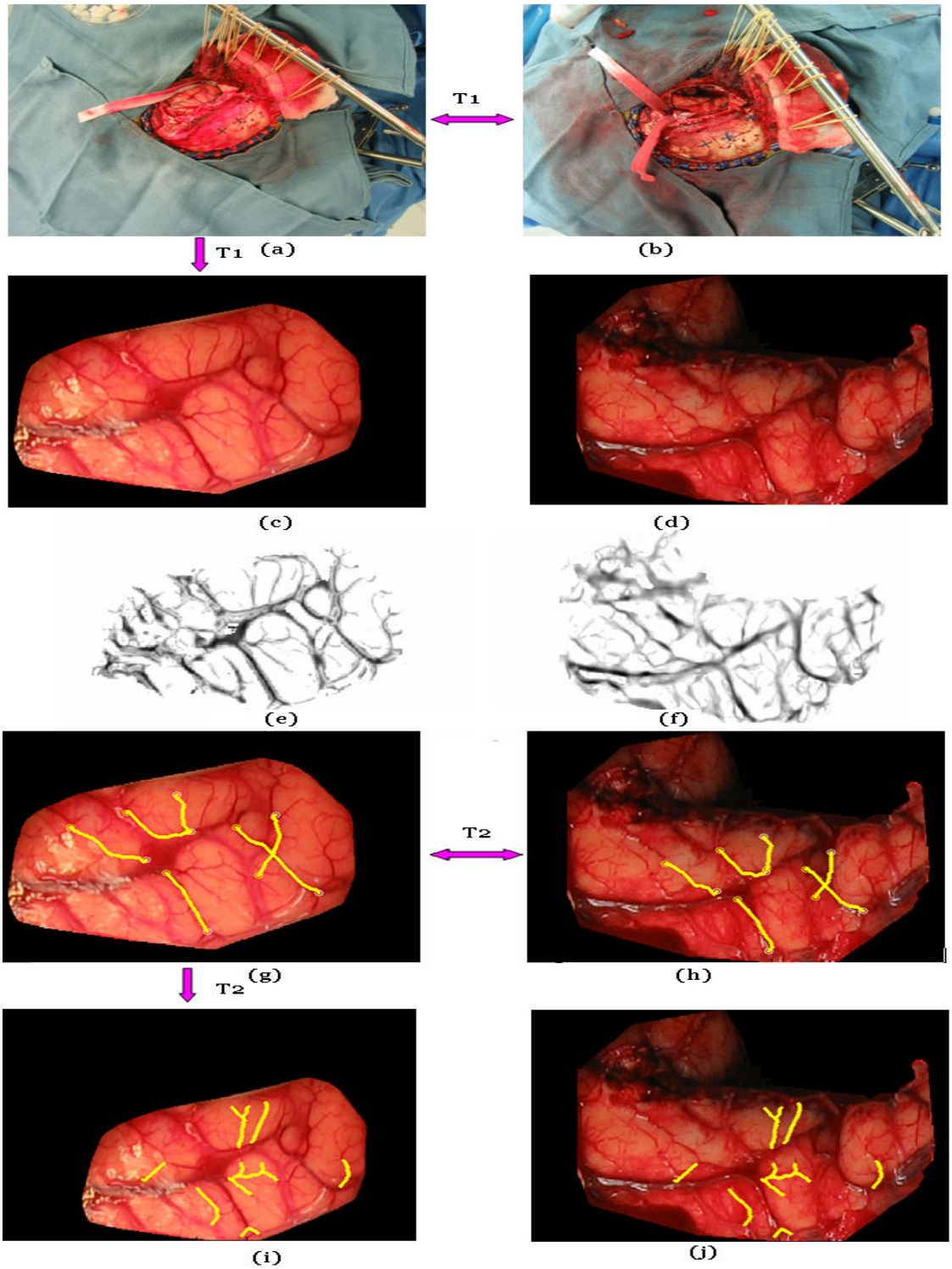

Fig.III.5: Illustration of the various steps involved in the registration process. The top panels are the original images of patient #7. These are registered with a projective transformation (T1). The brain surface is extracted from the original images manually (c) and (d)). The feature maps are computed ((e) and (f)). Corresponding vessels are detected and the non-rigid transformation T2 is computed ((g) and (h)). T2 is applied to the image in panel (g) to generate the registered images ((i) and (j)).

Next, the feature maps are computed on the pre- and post-resection cortical images ((e) and (f)). Starting and ending points are identified manually and vessel centerlines are extracted ((g) and (h)). Using the centerlines, the transformation that registers the two cortical images is computed; this transformation is called $\boldsymbol{T_2}$. Panel (i) shows the pre-resection image registered to the post-resection image. A group of vessels were drawn in (i) and copied to (j), which shows a good correspondence with the vessels in image (j).

An additional transformation $\boldsymbol{T_3}$ (see Chapter II) not shown here relates a point in the image to a 3D coordinate. The shift at any point in the image is computed as the difference in the 3D coordinates of this point in the pre-resection scan and its corresponding 3D coordinates in the post-resection scan.

3.2.7. Validation Strategy

The method that has been used to validate the approach relies on the selection of homologous points. A number of points have been selected manually on the pre- and post-resection images. These are points that are relatively easy to identify in both images, which include vessel intersections, end points, etc. The number of homologous points varies from case to case, depending on what is visible in the images. Using the registration transformations described above, the points in the pre-resection images are projected onto the post-resection image and a registration error, which is called Target Registration Error (TRE) [86], is computed as

$$TRE_i = \sqrt{(T(\mathbf{X_i}) - \mathbf{Y_i})^T (T(\mathbf{X_i}) - \mathbf{Y_i})} \quad (8)$$

in which $\mathbf{X_i}$ and $\mathbf{Y_i}$ are the points selected in the pre-resection and post-resection images, respectively. The transformation T is the transformation obtained by concatenating all the elementary transformations discussed previously.

3.3. Results

3.3.1. Vessel centerline extraction with and without distance term

Fig.III.6 illustrates the effect of the distance term in the cost function used to detect the vessel centerlines. The left panel shows the entire image and the right shows a zoomed version of the region within the box. In the right panel, the white points are the path obtained with the vesselness feature alone. The green points are the path obtained when both the vesselness and the distance term are used. Clearly, the additional distance term favors points that are on the centerline. The effect of this term is more important for large vessels than for small ones.

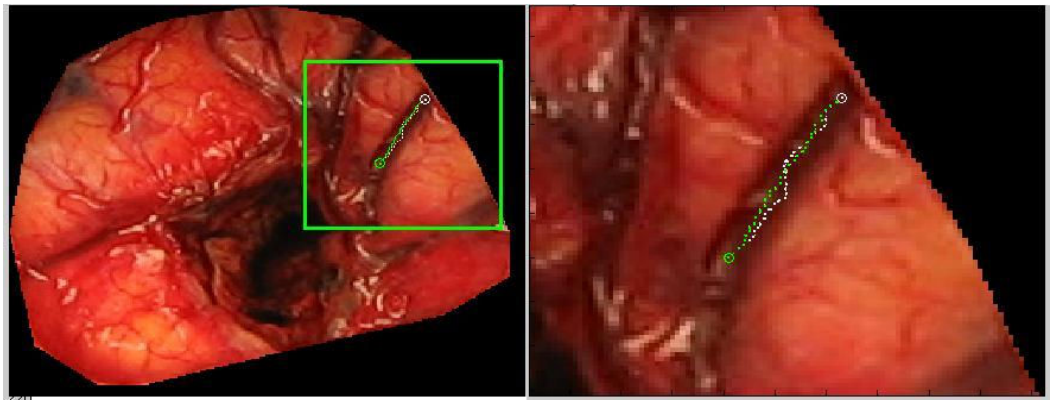

Fig.III.6: Difference in centerline extraction without (green points) and with (white points) the distance term using patient #3 data.

3.3.2. Sensitivity of the process to the selection of the points

The main manual input required by the algorithm is the selection of the starting and ending points in the pre- and post-resection images. To test the sensitivity of the algorithm to the selection of these points the following experiment was performed. One typical pre- and post- resection set of images was selected. In these images, a series of starting and ending points were manually picked. The position of the starting and ending points was then perturbed using random numbers drawn from Gaussian distributions with zero mean and standard deviation ranging from 2 to 5 pixels. For each standard deviation, the process was repeated a 100 times. For each set of points, the transformation that registers the pre- and post-resection images was computed. An additional registration in which the position of the points was not perturbed was computed and used as a baseline.

The difference between the baseline displacement and the displacement obtained with each of the transformations was computed pixel by pixel and averaged for each

standard deviation. Fig.III.7 shows average difference maps obtained for the various standard deviations used in this sensitivity study.

These results show submillimetric differences for standard deviations up to 3 pixels. When the standard deviation increases, some parts of the image experience an error that reaches 1 mm over regions that are far away from any vessels. This is because the transformation is not constrained over these regions. In practice, it is therefore important to select vessels, which cover as much of the field of view as possible.

The left panels in this figure show displacements that correspond to 2, 3, 4, and 5 pixels. It illustrates the fact that a displacement of 3 pixels in the x and y direction is easily noticeable. It also shows that even if the starting and ending points are not selected correctly, most of the trajectory between the points is the same. Thus, only a few of the feature points used for registration are different, which makes the process robust to operator error.

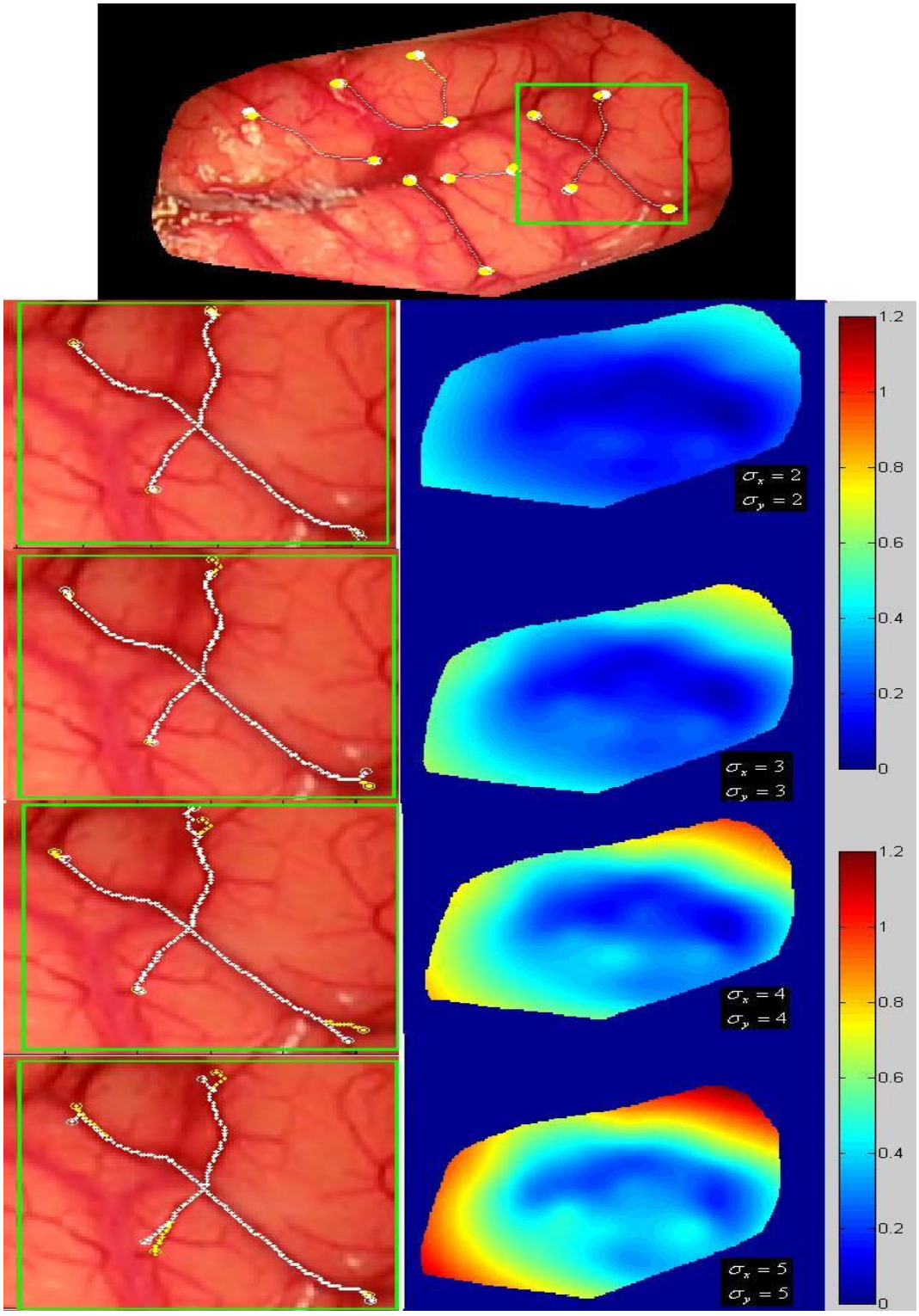

Fig.III.7: Effect of starting and ending points displacement on the registration. Top panel: original image of patient #7. The other panels show the region within the green square magnified (on the left) and the difference maps on the right. From top to bottom, the standard deviation used to perturb the points was increased from 2 pixels to 5 pixels.

3.3.3. Qualitative results

Fig.III.8 shows a pre- and a post-resection surface in the physical space. In this figure white and green homologous points have been selected on the pre- and post-resection images, respectively. The tip of the arrows is the position to which the white dots have been moved using the registration transformations. As can be seen these are close to the corresponding green points.

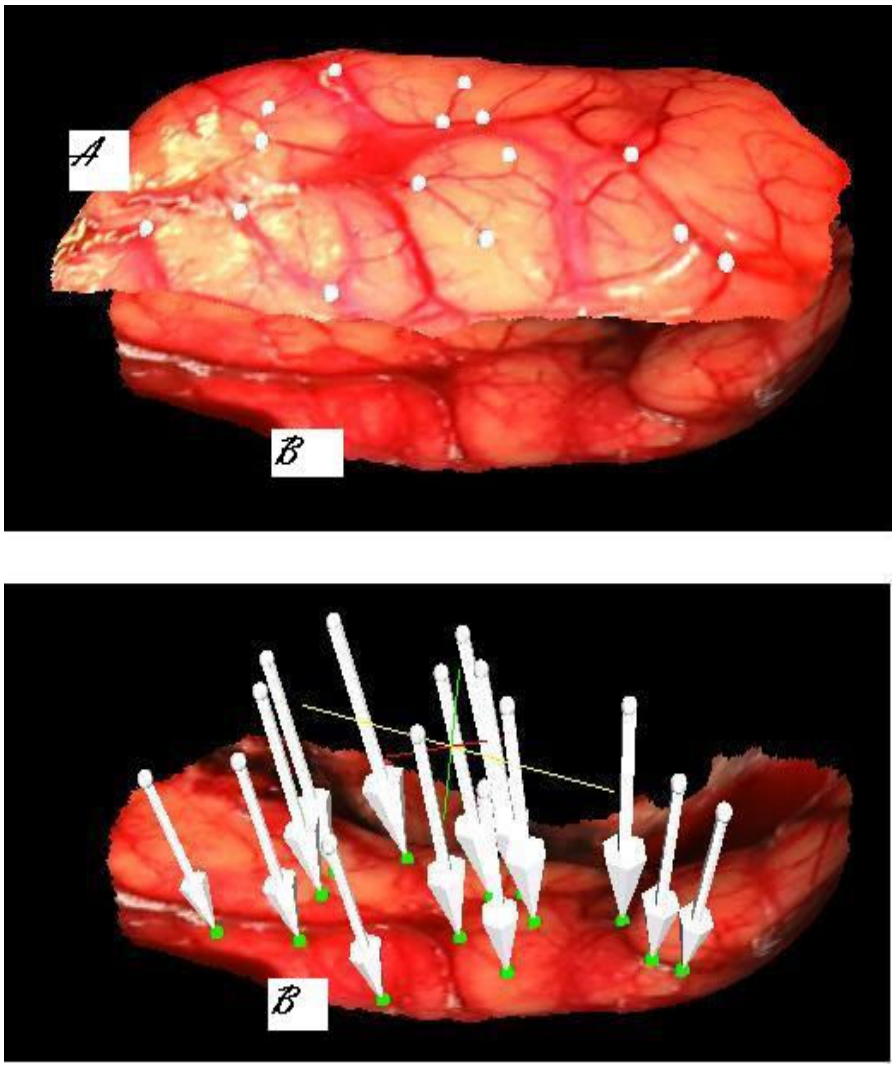

Fig.III.8: Top panel, texture surface obtained before resection (A) and texture surface **obtained after resection (B) of patient #7. The white points on the pre-resection scan and the green points in the post-resection scan were selected manually as corresponding points. On the bottom panel, the white arrows show where each white point has been mapped onto the post-resection scan.**

Fig.III.9 presents another set of results in which the pre- and post-resection textured surfaces ((A) and (B)) are shown. The color-coded and gray-level surfaces are the pre-resection and post-resection scans, respectively. The top left panel shows these surfaces before registration. The top right and bottom left both show the surfaces after registration ((C) and (B)). The bottom right panel shows a checkerboard image of the registered pre- and post-resection images indicating, at least visually, the quality of the registration.

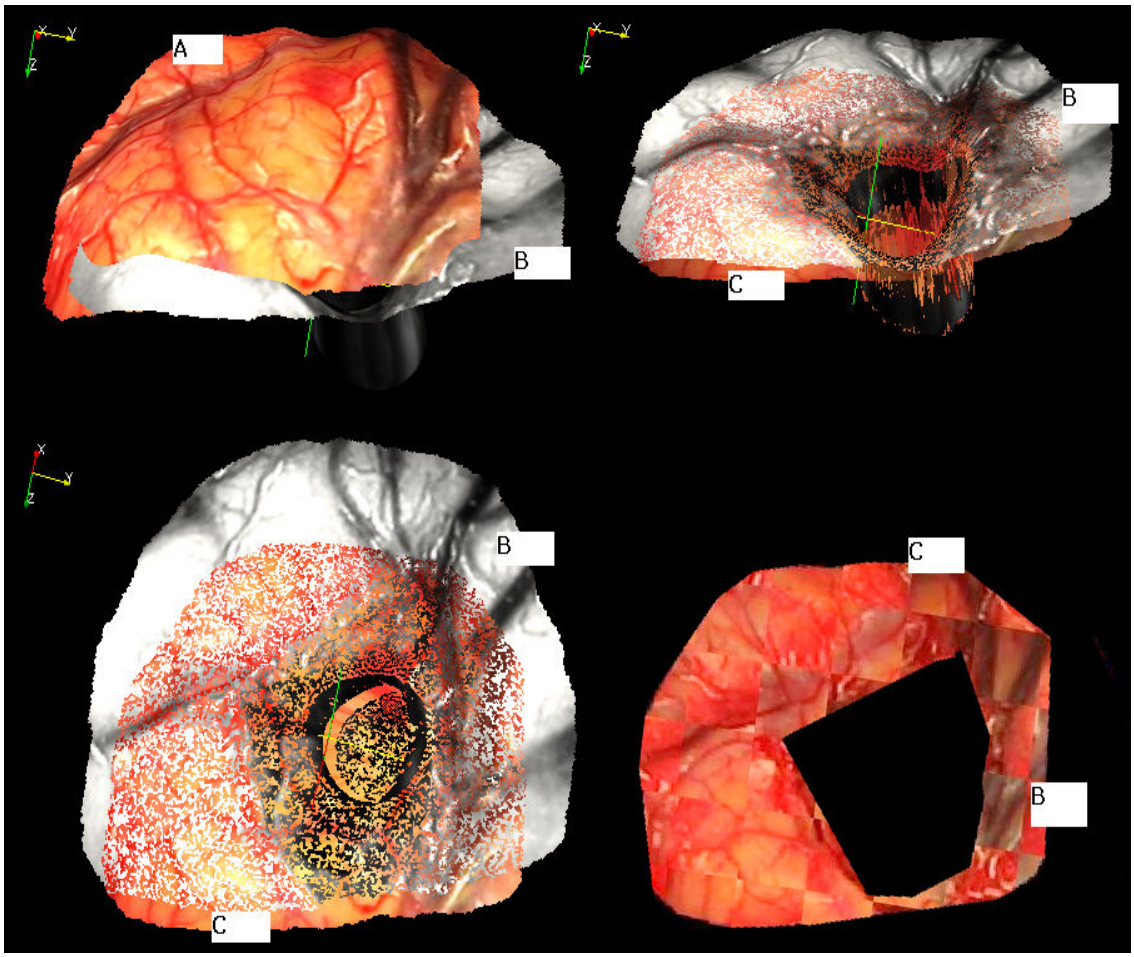

Fig.III.9: The top left panel shows the pre- (color) (A) and post-resection (gray) (B) textured surface of patient #3. The top right panel shows these two surfaces registered to each other using the proposed method. (C) is the deformed pre-resection surface. The bottom left panel shows the same but from a different angle. The bottom right panel shows a checkerboard image generated with the registered pre- and post-resection textured images, which indicates a good registration between the two.

Interaction time to select homologous points varies between 30 and 60 seconds, depending on the number of line segments being selected. Computation of optimal paths, which, as discussed before takes about one second per path, can be computed while manual selection for new vessel segments is ongoing. As currently implemented, the computation of the registration transformations take between 1 and 5 minutes, depending on the number of points in each of the two points sets used by the RPM algorithm.

3.3.4. Quantitative results

Table.III.1 presents quantitative results obtained with 10 patients (4 men and 6 women). In addition to the mean and max TRE values for each case, it lists the volume of the tumor, the size of the craniotomy, and the measured surface shift. Lesion size was measured from preoperative MR images acquired for each subject. Mean cortical surface shift were calculated as average distance of human selected homologous target points on textured laser range scans. The maximal cortical surface shift is the largest shift among target points. These results show an average TRE, which is submillimetric, and average surface displacements on the order of 1cm with a maximum value of 2.7cm.

Homologous points used to validate the results are selected on vessels or at the intersection of vessels because these are the only easily discernible features in the images. Some of these points may also be included or are in close proximity to points that have been used for the registration. In this application, this problem is difficult to avoid because of the difficulty of selecting homologous points in uniform areas. One also notes

that, because the robust point matching algorithm is used, (1) a strict correspondence between points in the two images is not established and (2) the thin-plate spline transformation does not match the point pairs exactly. There is thus a non-zero registration error, even for points included in the set used for the computation of the transformation itself. Furthermore, in practice, care is taken to select vessel segments that cover the useable portion of the image, thus constraining the transformation. It is therefore reasonable to assume that the error values that are being reported are representative of the errors over the entire image but that a slightly larger error could be observed over regions in which feature points are not selected.

Table.III.1: Average target registration errors and estimated brain's surface shift for 10 tumor resection cases

Patient #	Age (yr) /Sex	Crani-otomy Dia-meter (cm)	Lesion Size (cm^3)	Number of targets	Maximum TRE (mm)	TRE (mm)	Maximum shift (mm)	Mean shift (mm)
1	22 /F	7.7	5.2 x 6.2 x 6.0	15	2.79	1.13	27.51	23.57
2	52 /M	8.3	4.9 x 5.6 x 5.0	15	2.24	1.06	20.68	15.13
3	58 /M	4.7	3.7 x 3.5 x 4.1	9	1.77	0.75	10.34	8.50
4	77 /M	5.0	3.4 x 3.6 x 2.0	6	2.73	1.28	10.81	9.15
5	57 /F	3.5	1.0 x 1.4 x 2.0	6	0.84	0.44	3.45	1.89
6	56 /F	4.5	4.7 x 3.2 x 4.0	18	2.49	0.92	5.59	2.72
7	75 /F	6.1	5.0 x 5.0 x 5.0	15	2.92	0.62	15.27	13.01
8	23 /F	6.4	4.0 x 3.0 x 3.0	18	2.02	0.88	3.92	2.97
9	46 /F	4.3	3.0 x 3.0 x 3.0	9	1.94	0.70	9.40	8.07
10	26 /M	9.0	6.9 x 4.0 x 4.0	15	1.97	0.91	12.45	8.99
Ave-rage	49	5.95 ± 1.87	76.96 ± 61.37	13 ± 5	2.17 ± 0.62	0.87 ± 0.25	11.94 ± 7.58	9.40 ± 6.60

Fig.III.10 plots the TRE value for 126 points vs. their distance to the closest point included in the set of points used to compute the transformations. This figure shows a weak but nevertheless significant ($r = 0.35$) correlation between TRE and distance to feature.

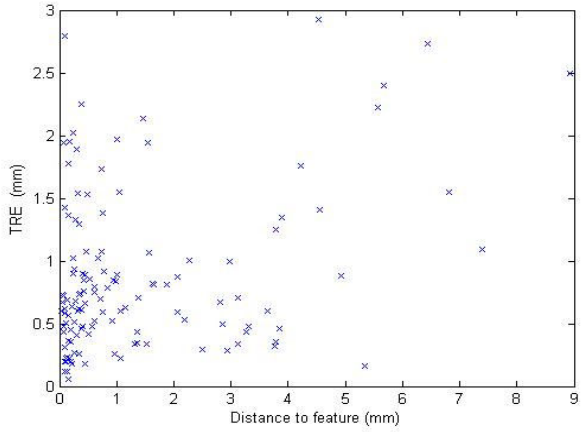

Fig.III.10: Plot of TRE error versus the distance to closest feature point used to compute the registrations.

3.3.5. Discussions and conclusions

Accurate estimation of brain shift occurring during surgery is critical for image-guided neurosurgery. Mathematical models capable of predicting shift occurring away from the surface are currently being developed [93] but these models need intraoperative brain measurements as input. A number of methods have been proposed over the years to measure brain shift, which occurs when the dura is opened, but this is the first study that extensively reports on measurement made after tumor resection. Tracked probes are a possible solution to acquire this information but this method often leads to sparse information as homologous points need to be identified on the cortical surface before and after resection. Furthermore, drastic changes in the appearance of the brain surface between pre- and post-resection makes the selection of homologous points a challenging task. The tracked laser range scanner approach presented in this dissertation is minimally

disruptive as it only requires moving the scanner in and out of the field to acquire data sets, which takes on the order of one minute. The laser range scanner also generates dense data sets, potentially providing the model with displacement values over the entire exposed surface. The key issue to accurate estimation of surface displacements is the registration of the laser range scanner data sets. Because the 3D point clouds are registered to high resolution 2D images, this problem can be solved by registering the 2D images. It has been shown in Chapter II that registering the 3D data sets via the 2D images does, in fact, produce results that are superior to those obtained when registering the 3D point clouds directly. The major difficulty to be addressed is the difference observed in the images before and after resection in most clinical cases. Except when tumors are very small, resection produces differences in the images that are such that intensity-based methods are ineffectual. Preliminary results in Chapter II on a smaller data have shown that a promising alternative is to register images using vessels delineated in the images. But delineating manually vessels in pre- and post-resection images is relatively difficult, time consuming, prone to errors, and not practical in the operating room. In this chapter, a practical solution is proposed. The feature maps can be computed rapidly, pre- and post-resection images presented to the physicians and starting and ending points identified. Because the system computes a minimum cost path between starting and ending points, very accurate selection of the points is not critical. The results that have been obtained on tumor resection cases demonstrate the accuracy of the process with an overall submillimetric TRE. The data gathered from the 10 patients included in the study also show significant brain shift. The average observed brain shift is about one centimeter with a standard deviation of 6.6 mm. Shifts greater than one centimeter have

been observed in 3 of the 10 cases, thus corroborating the need for intraoperative updating of preoperative information.

With the MATLAB implementation of the RPM algorithm [91], computing the transformation that registers the images and applying that transformation to the image takes between one and five minutes, depending on the number of points used and the size of the images. Since this method will be part of the user interface of a comprehensive system designed for intraoperative brain shift correction, it has been re-implemented in the C++ programming language and it now takes less than 1 minute. In the next chapter, we propose a method that could automate the vessel selection process further.

CHAPTER IV

AUTOMATICAL SEGMENTATION OF VESSELS IN PRE- AND POST-TUMOR RESECTION LASER RANGE SCAN IMAGES

Siyi Ding[1], Michael I. Miga[2], Reid C. Thompson[3], Ishita Garg[2], Benoit M. Dawant[1]

[1]Vanderbilt University, Department of Electrical Engineering, Nashville, TN, 37212

[2]Vanderbilt University, Department of Biomedical Engineering, Nashville, TN, 37212

[3]Vanderbilt University Medical Center, Department of Neurosurgery, Nashville, TN, 37212

[This manuscript has been published in *Proceedings of SPIE: Medical Imaging*, Orlando, FL, USA, vol. 7261, 2009.]

Abstract

Measurement of intraoperative cortical brain movement is necessary to drive mechanical models developed to predict sub-cortical shift. At our institution, this is done with a tracked laser range scanner. This device acquires both 3D range data and 2D photographic images. 3D cortical brain movement can be estimated if 2D photographic images acquired over time can be registered. In Chapter II and Chapter III, we have developed a method, which permits this registration using vessels visible in the images. But, vessel segmentation required the localization of starting and ending points for each vessel segment. In this chapter, we propose a method, which automates the segmentation process further. This method involves several steps: (1) correction of lighting artifacts, (2) vessel enhancement, and (3) vessels' centerline extraction. Result obtained on 5 images obtained in the operating room suggests that our method is robust and is able to segment vessels reliably.

4.1. Introduction

Estimating cortical surface shift accurately during surgery is of great importance in image guided neurosurgery. Although interventional MR method can be used, they are expensive and therefore not widely available. Tracked ultrasound-based methods are an alternative but they suffer from relatively poor spatial resolution. Vessel- and sulci-based registration methods have been proposed to estimate brain shift after opening of the dura from video images as early as 1997 by Nakajima et al. [45]. In their work, vessels segmented in preoperative MR images (using a threshold) were registered to surface

vessels from the intraoperative video images. However, the vessels were manually segmented from the video images. This approach was extended by Sun et al. [37] who used a pair of cameras. They demonstrate their ability to track the shape of the cortical surface after the opening of the dura on two neurosurgical cases. A similar approach is followed by Skrinjar et al. [36]. More recently, Delorenzo et al. [34, 35] have used a pair of stereo images and they register preoperative images with intraoperative video images using a combination of sulcal and intensity features. They propose a method by which registration and camera calibration are performed simultaneously and they show that this approach permits to correct calibration errors. In their work, sulcal grooves were segmented by hand and the system was applied to patients undergoing stage 1 epilepsy surgery. This is a procedure, which requires the opening of the dura for the placement of an array of intracranial electrode on the surface of the brain but it does not require resection.

As discussed above, a number of methods have been proposed to measure brain shift during surgery but, to the best of our knowledge, these have not been evaluated on data sets acquired after tumor resection. Previous clinical evaluation has been largely limited to measuring cortical or tumor shift following craniotomy or opening of the dura. Although difficult, this is considerably less challenging than attempting to measure shift during the case after resection because the resection alters the appearance of the images substantially. Indeed, the resection creates a hole in the images and induces brain sagging. As a result, parts of the cortex visible through the craniotomy before the resection become invisible after the resection, and vice versa. Furthermore, bleeding that occurs during the procedure alters the image contrast. To address these issues we have proposed

a method based on manually extracted vessels, which is described in Chapter II.

At our institution, we use a tracked laser range scanner, which acquires simultaneously 2D images and 3D point clouds.

Through calibration, these data sets are registered. The 3D coordinates of any points in the 2D image are thus available. Intraoperative brain displacement measurement can thus be achieved by registering 2D images acquired over time during the procedure. We are particularly interested in measuring brain displacement after tumor resection.

In Chapter II, we have shown that using cortical vessels visible in the pre- and post- tumor resection images is a possible solution to register the images based on manually extracted vessels. We expanded this work by proposing a semi-automatic vessel extraction method in Chapter III. This method requires labeling of homologous starting and ending points for each vessel segment for both pre- and post- resection images. A minimal-cost path algorithm is then used to connect these points automatically. In this chapter, we present our efforts to further automate the task and we focus on the automatic segmentation of the vessels. Challenges that need to be overcome include lighting conditions that create reflections and the appearance of blood, which reduces the contrast between the vessels and brain tissue. The method we propose consist in three steps: (1) correction of lighting artifacts, (2) vessel enhancement, and (3) vessel segmentation. These are detailed in section 4.3. Section 4.4 presents segmentation results we have obtained on a number of pre- and post-operative images.

4.2. Data Acquisition

In this study, a high resolution commercial LRS (RealScan3D USB, 3D Digital Inc., Bethel, CT, USA) system is used. This device is capable of generating 500,000 points with a resolution of 0.15mm-0.2mm at the approximate range used during neurosurgery. The resolution varies slightly according to the distance between the camera and the patient. The 3D position of each point on the scan is calculated via triangulation. At the same time, a digital camera (Canon Optix 400) acquires a texture image with a resolution up to 2592 by 1944 pixels. The texture image and the 3D point cloud are registered. A complete data set thus includes a set of image pixels with coordinates (u, v) and a series of points with coordinates (x, y, z). The (u, v) coordinates of any (x, y, z) point can be computed and vice-versa. In this study, the obtained texture images will be used to segment cortical surface vessels.

The following protocol, which was approved by the Vanderbilt Institutional Review Board, was used to acquire data from consented patients. After opening of the dura, the LRS system, which is mounted on adjustable arm or a monopod, is placed within 20-30cm of the patient. A pre-resection scan is taken, which takes on the order of 1 minute. This includes moving into the field, and collecting the data. The system is removed from the field and the procedure proceeds normally. After tumor extraction, a post-resection scan is acquired by moving the scanner back into place above the craniotomy. Because the scanner is tracked, the pre- and post-resection positions do not need to be exactly the same. More details about the data acquisition procedure can be found in [40]. Fig.IV.1 shows a patient in the OR with the tracked laser range scanner positioned on the top of the craniotomy.

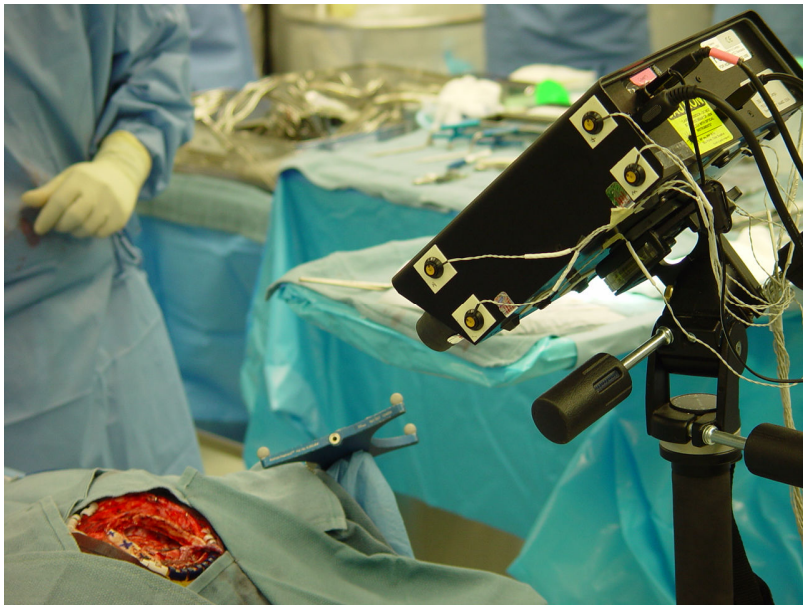

Fig.IV.1: shows a laser range scanner acquiring data in the operating room. The height and angle of the scanner are both adjustable. A built-in digital camera inside the scanner acquires high resolution digital images immediately after the range data has been acquired.

4.3. Method

As discussed in the previous section, images acquired intra-operatively are affected by two major sources of artifacts: lighting and bleeding. Lighting artifacts area caused by the reflection of the intraoperative lights on the surface of the brain. Bleeding, which occurs during the procedure, affects the contrast in the images and makes vessels more difficult to segment. In this chapter, we propose a three-step approach to segmenting surface vessels. These steps are (1) correction of the lighting artifacts, (2) enhancement of the images, and (3) segmentation.

4.3.1. Correction of lighting artifacts

Elimination of lighting artifacts involves first localizing regions in the image, which are affected. This is done via clustering of the points in the RGB space. The images are classified into several classes using an unsupervised K-means clustering algorithm, which aims at minimizing

$$V = \sum_{i=1}^{k} \sum_{x_j \in S_i} (x_j - \mu_i)^2 . \tag{9}$$

The 3D feature vector x_j is constructed using values in the R, G and B channels. S_i is the label of class i, and k is the number of classes. μ_i is the centroid of each class. Since there are only background, tissue, vessels, and artifacts in our image, four points are randomly chosen as centroids for each class and iteratively updated until converge. Every point in the image is assigned to the class, which has a center closest to its own. This unsupervised clustering method is not good enough for segmenting the vessels or the tissue but the class with the brightest centroid captures the artifact pixels. This is shown in Fig.IV.2. Panel (a) shows one original intraoperative image; the very bright regions are regions affected by the lighting artifact. Panel (b) shows the clustering results. The brightest pixels correspond to regions that have been identified as being affected by reflection and that need to be corrected. The other three classes are not used in subsequent steps.

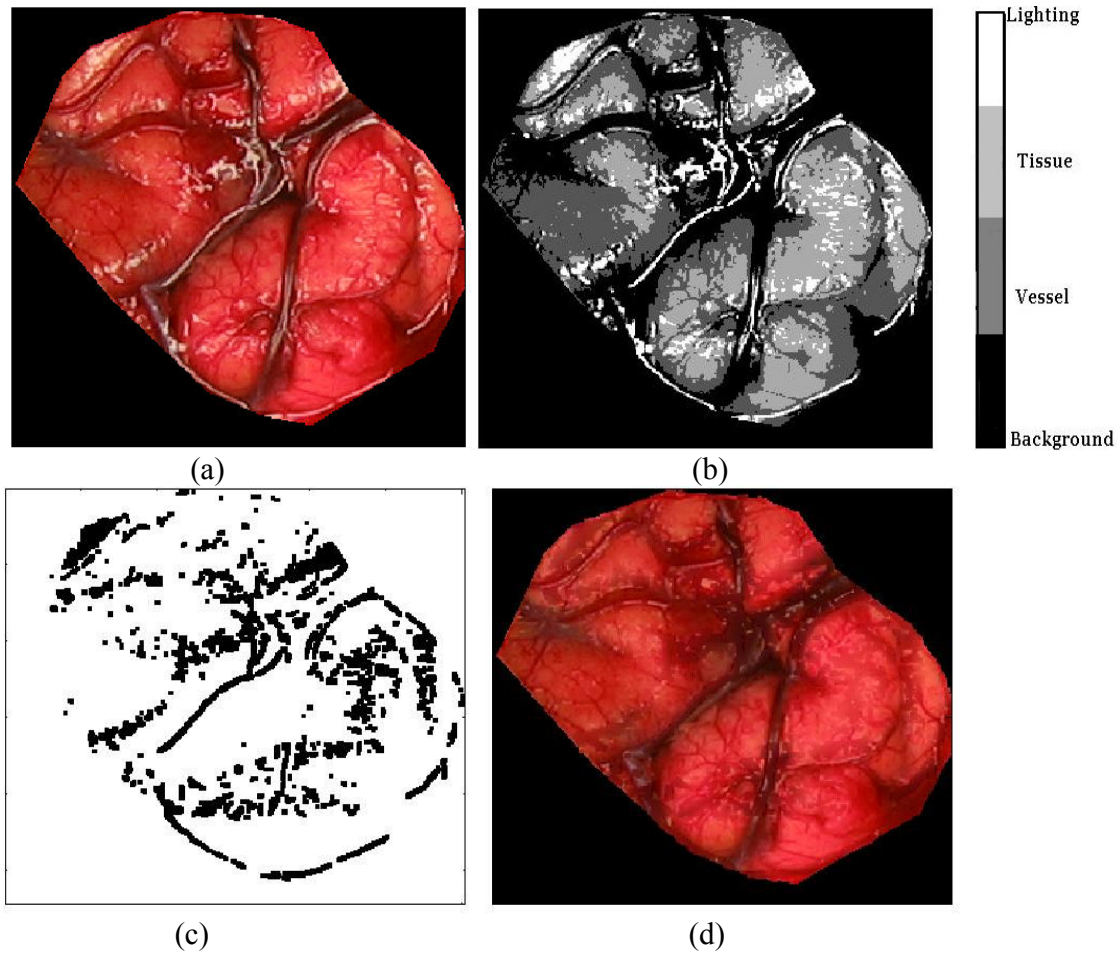

Fig.IV.2: shows the results after clustering and the results after correction of artifacts. Panel (a) shows one intraoperative image, which is degraded by lighting artifacts. Some of the pixels affected by these artifacts are inside the vessels, and some of them are outside the vessels; Panel (b) is the labeled map obtained with k-means clustering, and the very bright regions are dilated by 3 pixels and shown in (c); (d) is the image after artifacts correction.

The artifact regions are then expanded by dilating them by three pixels to incorporate edge pixels, which may not have been classified as artifact. Panel (c) in Fig.IV.2 is the artifact regions after dilation. Finally, the R, G, B values of the pixels in these regions are replaced by new R, G, B values obtained by extrapolating the R, G, and B values using surrounding pixels. Panel (d) shows the results after correction. Most of the lighting artifacts are automatically identified and removed in this image. The quality of the image is greatly improved for later processing.

4.3.2. Vessel enhancement

Vessels in the image are enhanced using a line searching algorithm akin to the line detection filter proposed in [94]. Here, we do not use the filter to segment the vessels but to reduce intensity variations within the vessels and to eliminate very small vessels for which finding a homologous vessel in another image may be difficult.

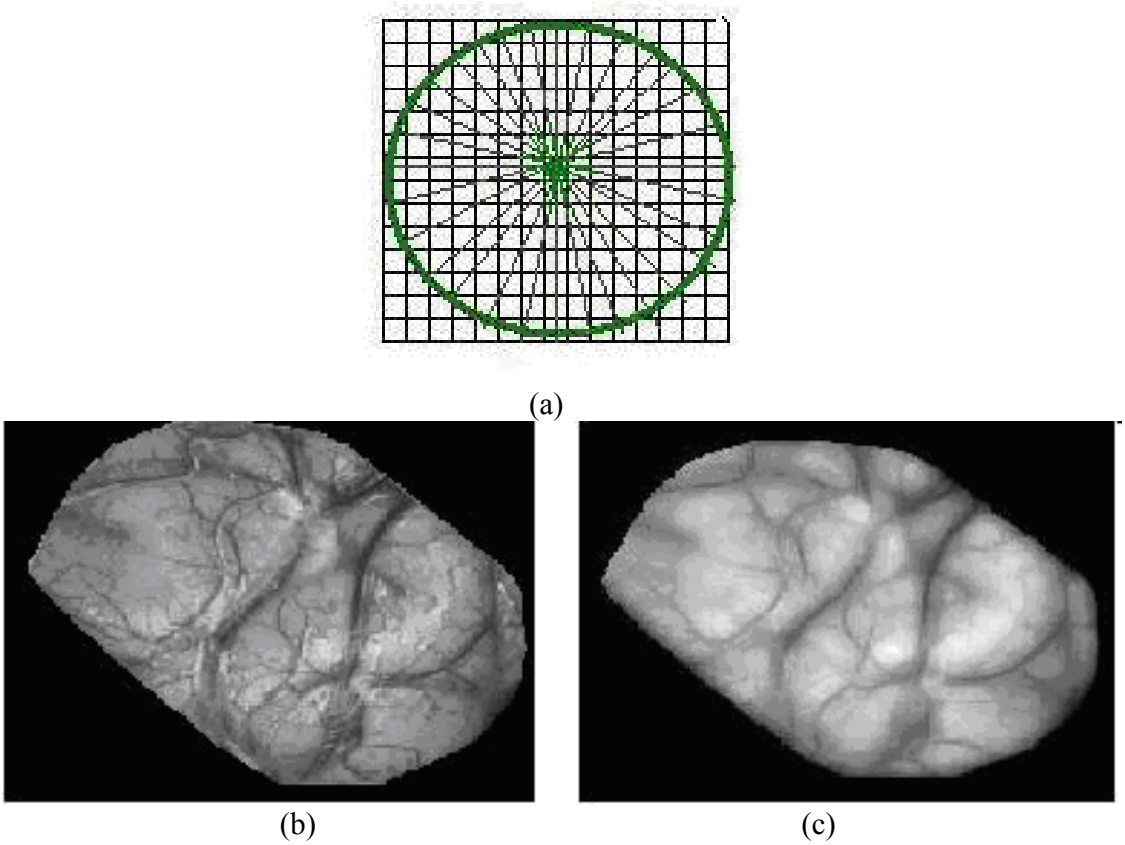

(a)

(b) (c)

Fig.IV.3: Panel (a) illustrates the neighborhood and searching directions used for vessel enhancement. The center of the circle is the pixel of interest. Panel (b) shows an intraoperative image before vessel enhancement. Panel (c) shows the result after vessel enhancement.

To filter the image, a circular window of radius w is first placed on a foreground pixel. Straight lines oriented in increment of α degrees are then defined (see Fig.IV.3 (a)). The average intensity along these lines is computed and the line with the smallest average

values is identified. For each pixel in the foreground of the image, the direction of the vessels is the direction of the line with the lowest mean value (vessels are dark in our images), and the intensity value of the pixel on which the window is centered is substituted by this minimal mean intensity value.

Values of $w = 7$ and $\alpha = 15^{\circ}$ were chosen experimentally.

4.3.3. Vessel segmentation

4.3.3.1. Multiscale vesselness

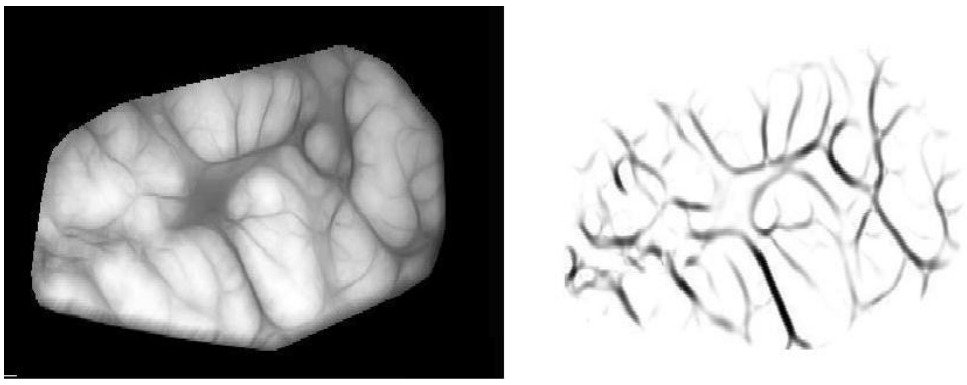

(a) (b)

Fig.IV.4: Panel (a) shows one intraoperative image after vessel enhancement; Panel (b) shows the vesselness map.

Vessels in the enhanced images are segmented in two steps (more details can be found in Chapter III). First, the images are filtered with the vesselness filter propose by Frangi et al. [67]. In their work, they propose a multi-scale filter based on the Hessian of the image, which can be used to enhance tubular structures. The approach they propose is to (1) convolve the image with Gaussian filters with various standard deviations, (2)

compute the Hessian of the smoothed images, defined as

$$\nabla^2 I(x) = \begin{bmatrix} I_{xx}(x) & I_{xy}(x) \\ I_{yx}(x) & I_{yy}(x) \end{bmatrix}, \tag{10}$$

in which I_{ij} is the second spatial derivative of the image in the i and then j directions, and (3) compute the eigenvalues of the Hessian. An analysis of the values of these eigenvalues permits to determine the type of structure a particular pixel belongs to. Pixels, which pertain to tubular-like structures that are bright on a dark background, will satisfy the following conditions:

$$\begin{cases} 0 \approx |\lambda_1| << |\lambda_2| \\ \lambda_2 < 0 \end{cases}. \tag{11}$$

Based on this observation, the vesselness filter Frangi et al. proposed, is as follows:

$$V(i,j) = \begin{cases} 0 & \text{when} \quad \lambda_2(i,j) > 0 \\ \exp(-\dfrac{\lambda_1(i,j)^2}{2\lambda_2(i,j)^2\beta^2})(1-\exp(-\dfrac{\lambda_1(i,j)^2 + (\lambda_2(i,j))^2}{2c^2})) \end{cases}. \tag{12}$$

The first term in this equation is large when λ_1 is small and λ_2 is large. The second term, which is called the "second order structureness", is large for non-background pixels. To detect vessels of various dimensions, the filter is applied to images that have been convolved with Gaussian filters whose standard deviation is changed from small to large. The vesselness filter responds to small vessels in an image blurred with a Gaussian filter with a small standard deviation. It responds to large vessels in an image blurred with a Gaussian filter with a large standard deviation. The coefficient β and c are chosen experimentally. Here, β was chosen *as* 0.5, and c was chosen as 0.05 times the maximum intensity value in the image. In this application, we use six scales with variances ranging

from one to six pixels. The response of the filter at the scale with the maximum response is used as the filter's output

$$V(x, y) = \sum_{k=1}^{6} w_k V_k(x, y), \tag{13}$$

in which the value of the weight w_k is -1 for the standard deviation that produces the largest response and zero for all the others. This produces a gray scale image *V(x,y)* in which tubular structures are enhanced. The darker the pixel is, the more likely it belongs to a vessel structure.

4.3.3.2. Centerline extraction

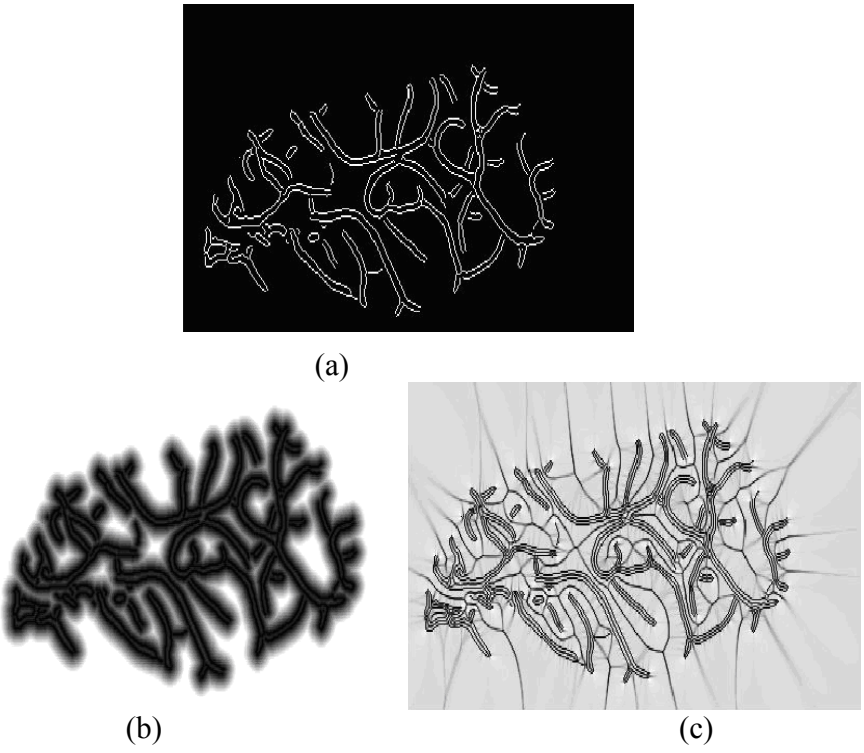

(a) (b) (c)

Fig.IV.5: Panel (a) shows the edge map of the image shown in Fig.IV.4 (b); Panel (b) shows the distance map of (a); (c) is the magnitude of the gradient of (b).

Next, we detect edges in the vesselness image using a Canny edge detector to create a binary edge map *E(x,y)* as shown in Fig.IV.5. (a). A distance map is then created

from this image using a fast marching method [95]. In the distance map shown in Fig.IV.5 (b), pixels on the vessels' edges are local minima and pixels on the vessels' centerlines are local maxima; the gradient of the distance map is thus small for these pixels, as shown in Fig.IV.5. (c). In this image, black corresponds to small values of the gradient magnitude.

Centerline pixels are localized by first taking the gradient of the distance map and keeping the voxels in the gradient image below a threshold (here we have an experimentally determined value of 0.7) to create a binary image *S(x,y)*. The edge image *E(x,y)* is then subtracted from this image and shown in Fig.IV.6 (a). This results in an image which contains all the pixels that are localized midway between two edges. Some of these pixels are inside the vessels, others outside. To eliminate outside pixels, those pixels with a vesselness value lower than 0.1 are eliminated. This creates the result shown in Fig.IV.6 (b). Finally, we apply an eight connected component labeling algorithm. Regions, which are smaller than 5 pixels are eliminated.

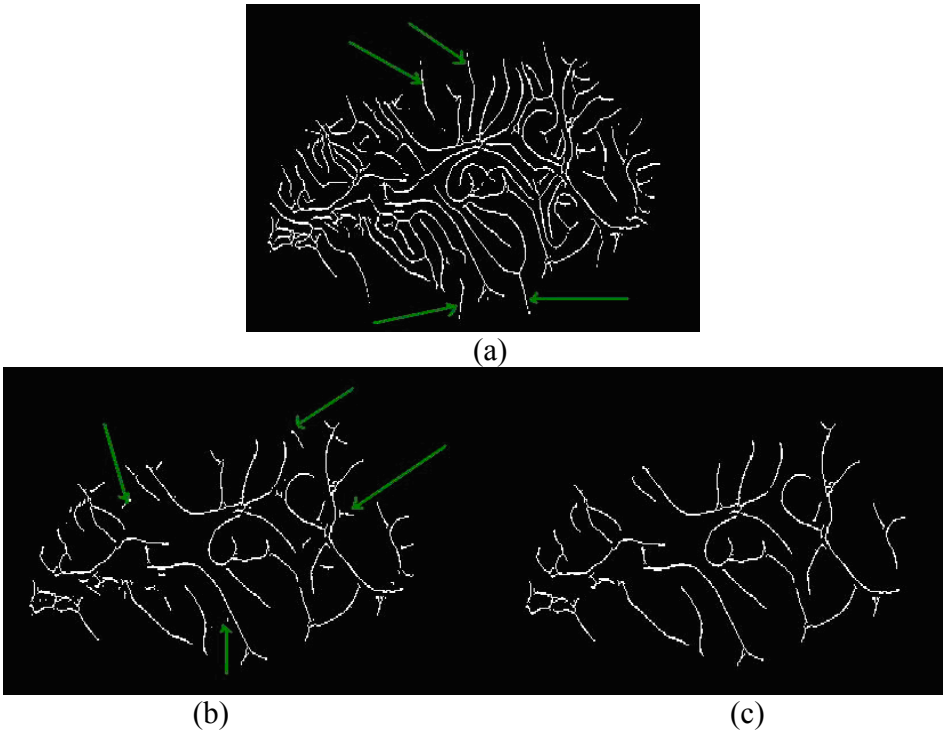

(a)

(b) (c)

Fig.IV.6: Panel (a) shows S(x,y), which is obtained from thresholding the image in Fig.IV.5 (c), after the edge map E(x,y) has been subtracted. Panel (b) shows a better image than Panel(a), because we eliminate the pixels with very low vesselness value, some of which are pointed by green arrows in (a). (c) is the final results after eliminating small connected regions, some of which are pointed by green arrows in (b).

4.4. Results

The proposed automatic vessel segmentation method has been tested on clinical digital images obtained intra-operatively. Fig.IV.7 shows representative results. Panel (a) shows the original vesselness image obtained from the image shown in Fig.IV.2 without any pre-processing. Panels (b) shows the same when the lighting artifact is removed. Panel (c) shows the results when the lighting artifact is removed and the vessels are enhanced. As seen in this figure, removal of the lighting artifact helps in preserving the

integrity of the vessels. Without correction, some of the large vessels are split in two because they reflect the light. The vesselness map obtained after vessel enhancement is clearly less noisy than the map obtained without enhancement. Panels (d) and (e) show the vesselness map for another intraoperative image without and with lighting artifact removal, respectively.

Fig.IV.8 illustrates the results obtained without (panel a) and with (panel b) lighting artifact removal and vessel enhancement overlaid on the original image. As can be seen, the artifact and vessel enhancement method we propose improve the segmentation of the large vessels and reduces the number of spurious vessels. As can also be seen, this comes at the expense of the number of small vessels that can be segmented. This is, however, not a significant issue for our application because it is difficult to establish a correspondence between small vessels in the pre- and post-resection images. Registration between these images will thus be based on the largest vessels.

Fig.IV.9 shows the final results on four images obtained intra-operatively. The left panels show pre-resection images, and the right panels show post-resection images. Note the holes left by the resection of the tumor.

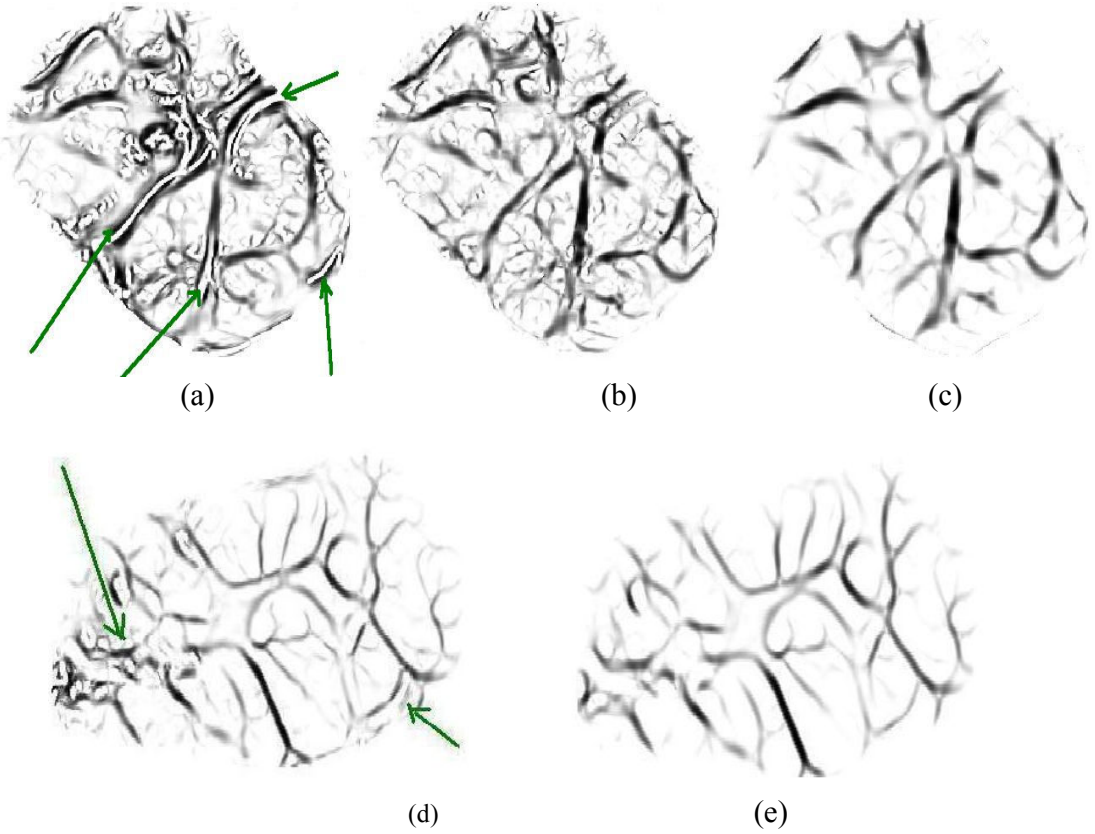

Fig.IV.7: Panels (a) and (d) show results when the vesselness filter is applied to the original images; Panels (b) and (e) show the vesselness images obtained by applying the vesselness filter on the image after lighting artifact correction. Panel (c) shows the vesselness image after both lighting artifact removal and vessel enhancement.

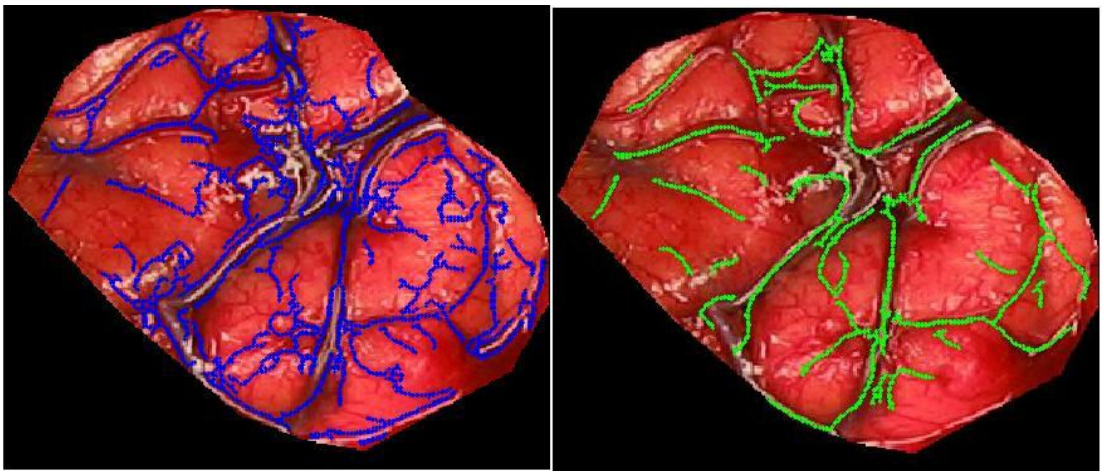

Fig.IV.8: The left panel shows vessels extracted without lighting artifact removal and vessel enhancement. The right panel shows vessels extracted using the method proposed in this chapter.

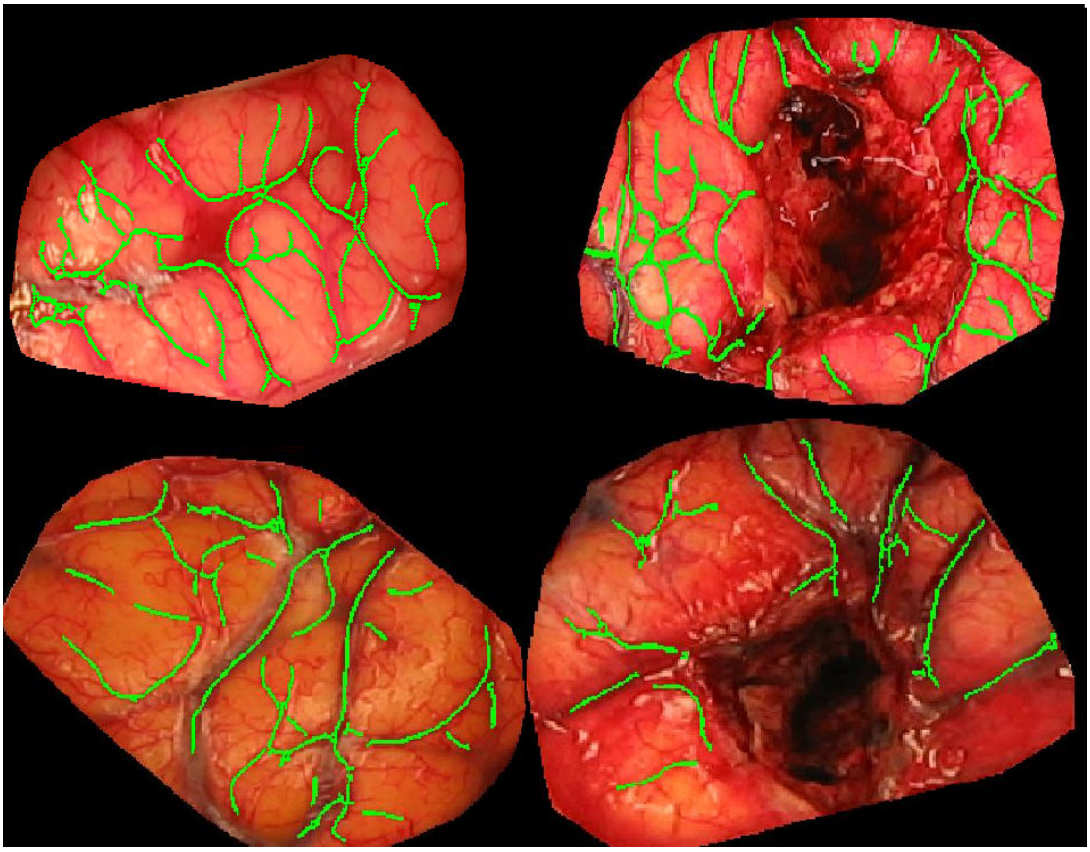

Fig.IV.9: This figure shows the extracted vessels overlaid on the original images. The left two images were acquired before tumor resection; the right two images were obtained after tumor resection.

4.5. Conclusion

Updating preoperative tomographic information is critical for image guided surgery. Systems designed to solve this problem typically rely on mechanical models driven by intraoperative measurements. Clinical acceptance of these systems will require solutions, which are fast, robust, and minimally intrusive. Acquiring images with our tracked laser range scanner is fast (on the order of one minute) and minimally intrusive because the scanner can be moved in and out of the operating field. The work presented

in this chapter indicates that automatic segmentation of cortical vessels is achievable. However, since automatically detected vessels in pre- and post- resection LRS images may be too different to be registered automatically, we will introduce microscope video sequences in the next two chapters. Since the pre-resection LRS image may be taken at about the same time as the first frame of a pre-resection video sequence, we could register the pre-resection LRS image to the first frame of the pre-resection video sequence easily. Then, if we could track each of the video sequence, as introduced in Chapter V, and register between video sequences, as demonstrated in Chapter VI, we will be able to integrate all the transformations and apply it to the pre-resection LRS image, it will make the deformed pre-resection LRS image very close to post-resection LRS image. Thus, automatic registration between this two are realistic, and the major purpose of this dissertation, automatic intraoperative brain displacement measurement, will be achieved.

CHAPTER V

TRACKING OF VESSELS IN INTRAOPERATIVE MICROSCOPE VIDEO SEQUENCES FOR CORTICAL DISPLACEMENT ESTIMATION

Siyi Ding[1], Michael I. Miga[2], Amber I. Simpson[2], Thomas S. Pheiffer[2], Reid C. Thompson[3], Benoit M. Dawant[1]

[1]Vanderbilt University, Department of Electrical Engineering, Nashville, TN, 37212

[2]Vanderbilt University, Department of Biomedical Engineering, Nashville, TN, 37212

[3]Vanderbilt University Medical Center, Department of Neurosurgery, Nashville, TN, 37212

[This manuscript has been submitted to *the IEEE Transactions on Biomedical Engineering.*]

Abstract

This chapter presents a method designed to track automatically cortical vessels in intraoperative microscope video sequences. The main application of this method is the estimation of cortical displacement occurring during tumor resection procedures. The method works in three steps. First, models of vessels selected in the first frame of the sequence are built. These models are then used to track vessels across frames in the video sequence. Finally, displacements estimated using the vessels are extrapolated to the entire image. The method has been tested on images simulating large displacement, tumor resection, and partial occlusion by surgical instruments and on 21 video sequences comprising several thousand frames acquired from three patients. Qualitative results show that the method is accurate, robust to the appearance and disappearance of surgical instruments, and capable of dealing with large differences in images caused by resection. Quantitative results show a mean Vessel Tracking Error (VTE) of 2.4 pixels (0.3 or 0. 6 millimeters, depending on the spatial resolution of the images) and an average Target Registration Error (TRE) of 3.3 pixels (0.4 or 0.8 millimeters).

5.1. Introduction

Most image-guided surgery systems in current clinical use only address the rigid body alignment of preoperative images to the patient in the operating room despite the fact that substantial brain shift happens as soon as the dura is opened [2, 4, 96, 97]. The problem is even more acute for cases that involve tumor resection. A possible solution to this problem is to use models [97-99] that can predict brain shift and deformation based

on cortical surface data acquired intra-operatively such as laser range scans [40-42, 46, 93, 100], or video images [34-37, 45, 101-104].

Video images acquired with cameras attached or integrated with the operating microscope have been proposed to register pre- and intra-operative data as early as 1997 by Nakajima et al. [45]. This approach has been extended in [37] and [36] by using a pair of cameras. In 2006, DeLorenzo et al. have used both sulcal and intensity features [34, 35] to register preoperative images with intraoperative video images. However, all of those studies were carried out on data acquired just after the opening of the dura [35] or on procedures such as epileptic surgery for which brain shift is relatively small compared to tumor resection surgeries [46, 100].

The objective of the work described in this dissertation is to develop a system that can be deployed in the Operating Room (OR) to update preoperative images and thus provide deformation-corrected guidance to the surgical team. To estimate surface deformation during the surgery a tracked laser range scanner [46, 100] has been employed. This device acquires simultaneously 3D physical coordinates of scanned object surfaces using traditional laser triangulation techniques and a color image of the field of view. Because the color image and the 3D cloud of points are registered through 2D-to-3D texture calibration, the 3D coordinates of the image pixels are known. Tracking the 3D displacement of the cortical surface can thus be achieved by registering the 2D color images acquired over time. This can be achieved by placing the laser range scanner in the operating room and acquiring data during the procedure. While feasible, this approach is somewhat difficult to use in practice, at least in our OR setting, because it requires positioning the scanner above the resection site and acquiring the data, which

takes on the order of one minute. One possibility is to acquire one laser range data set just after the opening of the dura and one or more additional scans during the procedure, typically after partial tumor resection. But, because substantial changes occur during the surgery, developing automatic techniques for the registration of the 2D static images that are acquired at different phases of the procedure by the scanner is challenging. As a partial solution, we have developed a semi-automatic method that only requires selecting starting and ending points on vessel segments that are visible in the scanner images that need to be registered [100]. Using this method, we have shown that it is possible to estimate the displacement of points on cortical surfaces with a sub-millimetric accuracy. These results were obtained on images acquired from 10 patients with mean cortical shift of about 9mm and range from 2mm to 23mm. In this chapter, we describe an effort to automate the registration of the laser range scanner images that uses video streams acquired with an operating microscope.

Operating microscopes are typically used during the procedure and these are often equipped with video cameras. Clearly, the video sequences have a much higher temporal resolution than images acquired with the tracked laser range scanner. Changes occurring between video frames are thus substantially smaller and automatic tracking of vessels through the video sequence may be possible. Estimating cortical shift during the procedure could thus be done as follows: (1) acquire a 2D image/3D point cloud laser scanner data set at time t_0; (2) register the 2D image acquired with the scanner to the first frame of a video sequence started shortly after t_0; (3) estimate 2D displacement/deformation occurring in the video sequence; (4) stop the video sequence at time t_1; (5) acquire a 2D image/3D point cloud laser scanner data set shortly after time t_1;

(6) register the 2D image acquired with the scanner at time t_1 with the last frame in the video sequence to establish a correspondence between laser range scanner image 1 and laser range scanner image 2; (7) compute 3D displacements for each pixel in the images through their associated 3D coordinates.

Recently, Paul et al. [103, 104] have proposed a technique to estimate cortical shift from video sequences but their approach is substantially different from ours. In their approach a pair of microscope images is used to create a surface at time t_1. At this time, a number of points are also localized in one of the video images. These points are tracked in one of the sequences until time t_2. At time t_2 another pair of images is acquired and another surface computed. Computation of cortical displacement requires the registration of the two surfaces. This is inherently a difficult problem because the appearance and shape of the surfaces changes through the surgery. In their work, they use a similarity measure to register these surfaces that relies on intensity, inter-surface distance, and on displacement information provided by the tracked points. Because we use a laser range scanner that provides us with the 3D coordinates of the pixels in the images it acquires, we do not need to estimate the 3D surface, nor do we need to register surfaces directly. The entire problem can be handled using much simpler 2D registrations.

The remainder of this chapter is organized as follows. First, the data that has been used is described. The technique that has been used to model and track the vessels is explained next. This is followed by a discussion on how vessel displacement is used to estimate displacements over the entire image. Simulated results show the robustness of the proposed method to displacement, partial occlusions, or changes caused by the

resection. Results obtained on real images confirm the simulated results and show overall submillimetric registration accuracy.

5.2. Data

A Zeiss OPMI®Neuro/NC4 microscope equipped with a video camera was used to acquire the video sequences. The frame rate of the video is 29 fps. A total of 21 sequences were acquired from 3 patients (7sequences/patient) with IRB approval. The images of patient 1 have 352 x 240 pixels, while the images of patient 2 and 3 have 768 x 576 pixels. The approximate pixel dimension in the video images of patient 1 is .06 mm^2, while it is .01 mm^2 for the other two patients. At those resolutions, cortical capillaries and small vessels can be seen in the images and used for tracking. Between sequences acquired for a particular patient the camera can be translated, rotated or its focus adjusted to suit the needs of the neurosurgeon.

To show the feasibility of registering video and laser range scanner images, one additional data set was acquired. This data set includes a laser range scanner image and one video sequence started 5 min after the acquisition of this image.

5.3. Method

A number of methods can be used to register sequential frames in video streams. For example, non-rigid intensity-based algorithm has been used to estimate heart motion in video streams [105]. However, as also reported by Paul et al. [104], this approach is not adapted to the current problem because surgical instruments appear and disappear from the field of view. To address this issue, a feature-based method, which requires finding homologous structures in sequential frames, has been adopted in this work. These structures are used to compute transformations that are subsequently utilized to register the entire image. Because the most visible structures in the video images are the blood vessels, they are employed as tracked features.

In the approach described herein, vessel segments are identified by the user in the first frame of a video sequence. This is done by selecting starting and ending points on these segments. A minimum cost path finding algorithm is then used to join the starting and ending points and segment the vessels (more details on this approach can be found in Chapter III).

5.3.1. Features used for tracking

Once the vessels are identified, their centerline is sampled to produce a number of points, which we call active points. In the current version of the algorithm this is done by downsampling the centerlines by a factor of four, which was found to be a good

compromise between speed and accuracy. For each of the active points, a line perpendicular to the centerline passing through the point is computed as shown in Fig.V.1.

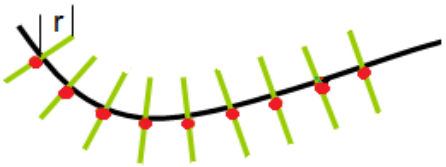

Fig.V.1: Active points along the curve.

Next, a feature matrix ***F*** (14) is associated with each point. To create this matrix, the R, G, B, and vesselness values are extracted from the image along the perpendicular lines. Vesselness, defined as in [67], is a feature computed from the Hessian of the image obtained at different scales (here scales ranging from 1 to 8 pixels have been used). It is commonly used to enhance tubular structures.

Because the R, G, and B values are intensity features while vesselness is a shape feature within the [0,1] interval, the R, G, B values are first normalized between 0-1, while the vesselness value is multiplied by 3 to avoid weighing one type of feature over another.

The length *r* of the perpendicular lines on either side of the centerline is a free parameter. Each active point is thus associated with the following matrix:

$$F_{a_i} = \begin{bmatrix} R_{-r} & R_{-r+1} & \dots & R_r \\ G_{-r} & G_{-r+1} & \dots & G_r \\ B_{-r} & B_{-r+1} & \dots & B_r \\ 3V_{-r} & 3V_{-r+1} & \dots & 3V_r \end{bmatrix} \quad (14)$$

5.3.2. Finding homologous points in consecutive frames

To match one frame to the other, homologous points need to be localized. This is done as follows. First, one feature matrix as defined above is associated with every pixel in the new frame. Second, the active points and the centerlines found in the previous frame are projected onto the new frame. Then the similarity between (a) the feature matrix of every pixel in the new frame along lines perpendicular to the centerlines and passing through the active points and (b) the feature matrix of the corresponding active point in the previous frame is computed as:

$$s(i,\ j) = 1 - \frac{1}{4(2r+1)} \sum_{c=1,d=1}^{c=4,d=2r+1} \left| \mathbf{F}_{\mathbf{a}_i}(c,d) - \mathbf{F}_{\mathbf{p}_{i,j}}(c,d) \right|, \qquad (15)$$

in which *i* refers to the *ith* point on the centerline and *j* is the position on the line perpendicular to the centerline at that point with $-s_r \le j \le s_r$, i.e., the computation is done in bands of width $2s_r+1$. $\boldsymbol{F_{a_i}}$ is the feature matrix in the previous frame of the *ith* active point and $\boldsymbol{F_{pi,j}}$ is the feature matrix in the new frame of the *jth* point along the perpendicular passing through the *ith* active point.

The point $\boldsymbol{b_i}$ with the feature matrix most similar to the feature matrix of the active point $\boldsymbol{a_i}$ in the previous frame is selected as the homologous point for this active point. However, if the maximum similarity between some $\boldsymbol{a_i}$ and all the $\boldsymbol{p_{i,j}}$ is small, it indicates that no reliable homologous point $\boldsymbol{b_i}$ can be found along the search line. When the maximum similarity falls below a threshold for a point $\boldsymbol{a_i}$, it is deactivated and not used to estimate the transformation that registers consecutive frames.

This process is illustrated in Fig.V.2. In this figure, the dotted line represents the projection of the centerline from the previous frame to the current frame. The red dots are

the active points. The lines perpendicular to the dotted lines are the search direction for each active point. The continuous line represents the position of the vessel in the new frame. In the left image, all the active points found their homologous points, which are shown as red star. In the right image, an object appears and covers part of the vessel. For some active point $\boldsymbol{a_i}$, this results in

$$\max_{j=-s_r}^{s_r} s(i,j) < \text{Similarity threshold.} \tag{16}$$

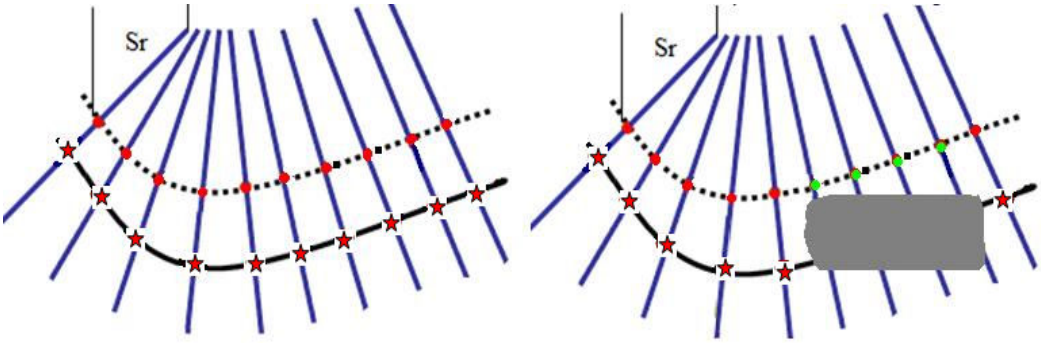

Fig.V.2: Strategy used to search for homologous points in the next frame.

5.3.3. Smoothing TPS

Smoothing Thin Plate Splines (TPS) are regularized TPS, which minimize the following functional

$$E(\mathbf{f}) = \min_{\mathbf{f}} \sum_{i=1}^{l} \left\| \mathbf{b}_i - \mathbf{f}(\mathbf{a}_i) \right\|^2 + \lambda \iint \left[\frac{\partial^2 \mathbf{f}}{\partial x^2} + 2\left(\frac{\partial^2 \mathbf{f}}{\partial x \partial y}\right) + \frac{\partial^2 \mathbf{f}}{\partial y^2} \right] dxdy \tag{17}$$

Here, smoothing TPS are used to compute the transformation that registers the active points $\{\boldsymbol{a_1}, \boldsymbol{a_2},\ldots,\boldsymbol{a_l}\}$ in one frame to the corresponding points $\{\boldsymbol{b_1},\boldsymbol{b_2},\ldots,\boldsymbol{b_l}\}$ in the next frame. For a fixed λ there exists a unique minimizer $\boldsymbol{f}$. To solve this variational problem, QR decomposition as proposed by Wahba [106] has been used. The parameter λ is used to control the rigidity of the deformation. When $\lambda \to \infty$, the transformation is constrained the most and is almost affine. Through experimentation, λ = 1 has been shown to produce transformations that are smooth, regular, and forgiving to local errors in point correspondence while being able to capture the observed inter-frame deformations/displacements. The transformation computed with the homologous points is then extrapolated over the entire frame. The algorithm developed is summarized in Table.V.1. All the results obtained have been computed with tracking one out of every 5 frames in the sequence to speed up the process. This downsampling did not affect the results.

Table.V.1: Automatic intra-video tracking in intraoperative videos

---

Step 1. Select features $\boldsymbol{C_k}$ in the first frame. $k = 1$; $r = 15$; $s_r = 75$; $\lambda = 1$.

Step 2. Downsample $\boldsymbol{C_k}$ into active points $\boldsymbol{a_i}$. For each active point, compute $\boldsymbol{F_{a_i}}$,

Step 3. In frame $k + 1$, search for the homologous point $\boldsymbol{b_i}$ for each active point $\boldsymbol{a_i}$.

If $\max_{j=-s_r}^{s_r} s(i,j) < 0.92$, deactivate $\boldsymbol{a_i}$ for the current frame.

Step 4. Calculate the transformation $\boldsymbol{T_k}$ that registers the active $\boldsymbol{a_i}$, $\boldsymbol{b_i}$ pairs.

Step 5. $\boldsymbol{C_{k+1}} = \boldsymbol{T(C_k)}$; $k = k+1$.

If k is not the last frame n, go to step 2, else end the tracking.

5.4. Results

5.4.1. Registration of laser scanner and microscope images

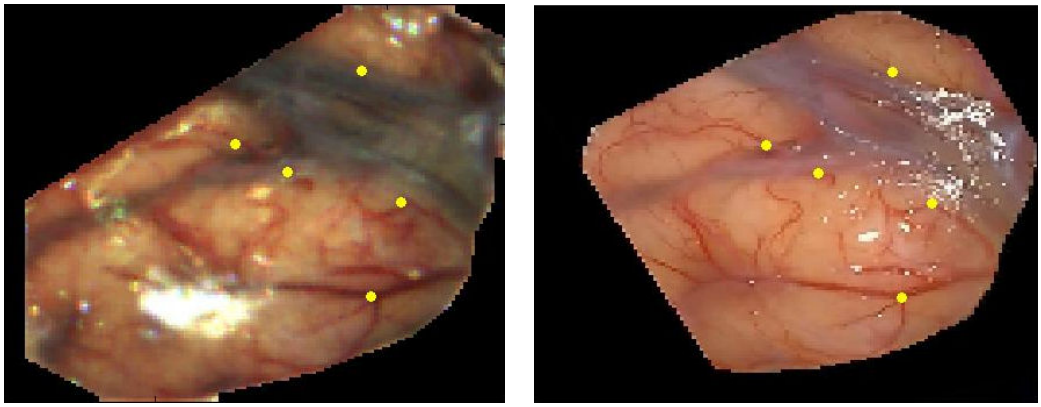

Fig.V.3: Example of registration of a 2D laser range scanner image (left panel) and one microscope image (right panel).

Fig.V.3 illustrates the feasibility of registering 2D images acquired with our laser range scanner (left panel) to a microscope image (right panel) acquired 5min after the scanner image. These images have been registered non-rigidly using vessels segmented semi-automatically. Yellow points have been selected on the microscope image and projected onto the laser image through the computed transformation.

5.4.2. Simulated results

To show the robustness of the algorithm to various challenging situations observed in clinical images, we have generated simulated sequences. First, we show its robustness to translation; then to occlusion and to changes produced by resection.

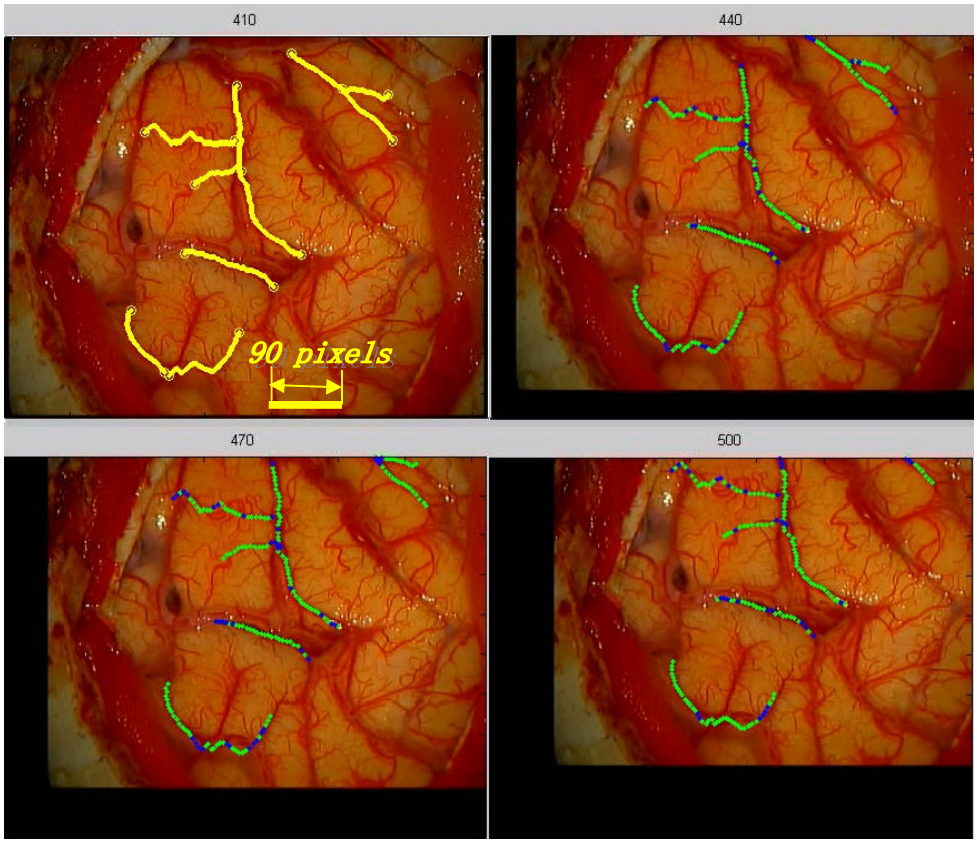

Fig.V.4: Simulation of a diagonal translation of 90 pixels in the *x* and *y* directions over 90 frames. Selected vessels are shown in yellow. Estimated vessel location produced by our algorithm is shown in green.

In clinical sequences, translation is observed when parts of the brain sag, causing portions of the cortical surface initially visible through the craniotomy to disappear under the skull. To simulate this situation, we have selected one video frame in one of patient #3 sequences, and we have translated it by 90 pixels in the *x* and *y* direction over 90 frames. Fig.V.4 shows four frames in this sequence. Tracked vessels are selected in frame

410 and shown in yellow in the top left panel of Fig.V.4. The location of the tracked vessels estimated by our algorithms on the frames 440, 470, and 500 are shown in green. Blue segments in the green traces are segments over which homologous active point were not found. When active points fall outside the image, they are deactivated and not used to compute the transformations.

Surgical instruments appear in the video sequence from time to time during the surgery. In order to show the robustness of the approach to the sudden appearance of objects in the field of view, one video sequence was selected and simulated instruments were inserted into the field of view to mask various parts of the image during portions of the sequence. The top left panel of Fig.V.5 shows frame 410 of patient #3. The vessels selected in frame 410 are shown in yellow. Tracking results are shown in green on the other frames. One point shown in white and indicated by an arrow on the first frame has been selected in the image to show overall displacement. The bottom right panel shows the Euclidean distance of the point to its original position in consecutive frames.

The oscillations observed in this plot are caused by small displacements of the cortical surface caused by brain pulsatility. In these simulations, an object is inserted on the left side of the image at frame 420 and disappears at frame 430, another object appears on the right side of the image at frame 470 and disappears at frame 480, and a third object appears in the top at frame 520 and disappears at frame 530. In the same sequence, a cavity induced by the resection has also been simulated. This was achieved by placing a small cavity in an incision visible in the image and progressively growing it. To achieve this, the image was expanded linearly within the cavity. Outside the cavity the magnitude of the deformation was reduced exponentially. The radius of the cavity was

increased from frame to frame. This results in images in which tissues surrounding the cavity are both displaced and compressed.

As was the case in the previous figure, vessel segments that appear in blue are segments over which active points were not found. The transformation used to register the frames was thus computed without them. But because the remaining segments are sufficient to compute a transformation that is accurate enough over the entire image, the computed position of the vessel during occlusion is approximately correct. As soon as the instrument disappears, the algorithm reacquires the vessels. This is possible because the vesselness component of the feature matrix is defined on the first frame and fixed for the entire sequence. When a surgical instrument appears in the field of view, it dramatically changes the vesselness value of the pixels it covers. Because of this, the similarity between these pixels and the centerline pixels projected from the previous frame falls below the threshold and no correspondence is found. As soon as the vessels become apparent again, the similarity value is above the threshold and the vessels are used. This will work well as long as the transformation computed without the covered vessels is a reasonable approximation over the covered regions, i.e., the vessel remains within the search window of the purple trace. One also observes that the presence of the cavity does not affect tracking results.

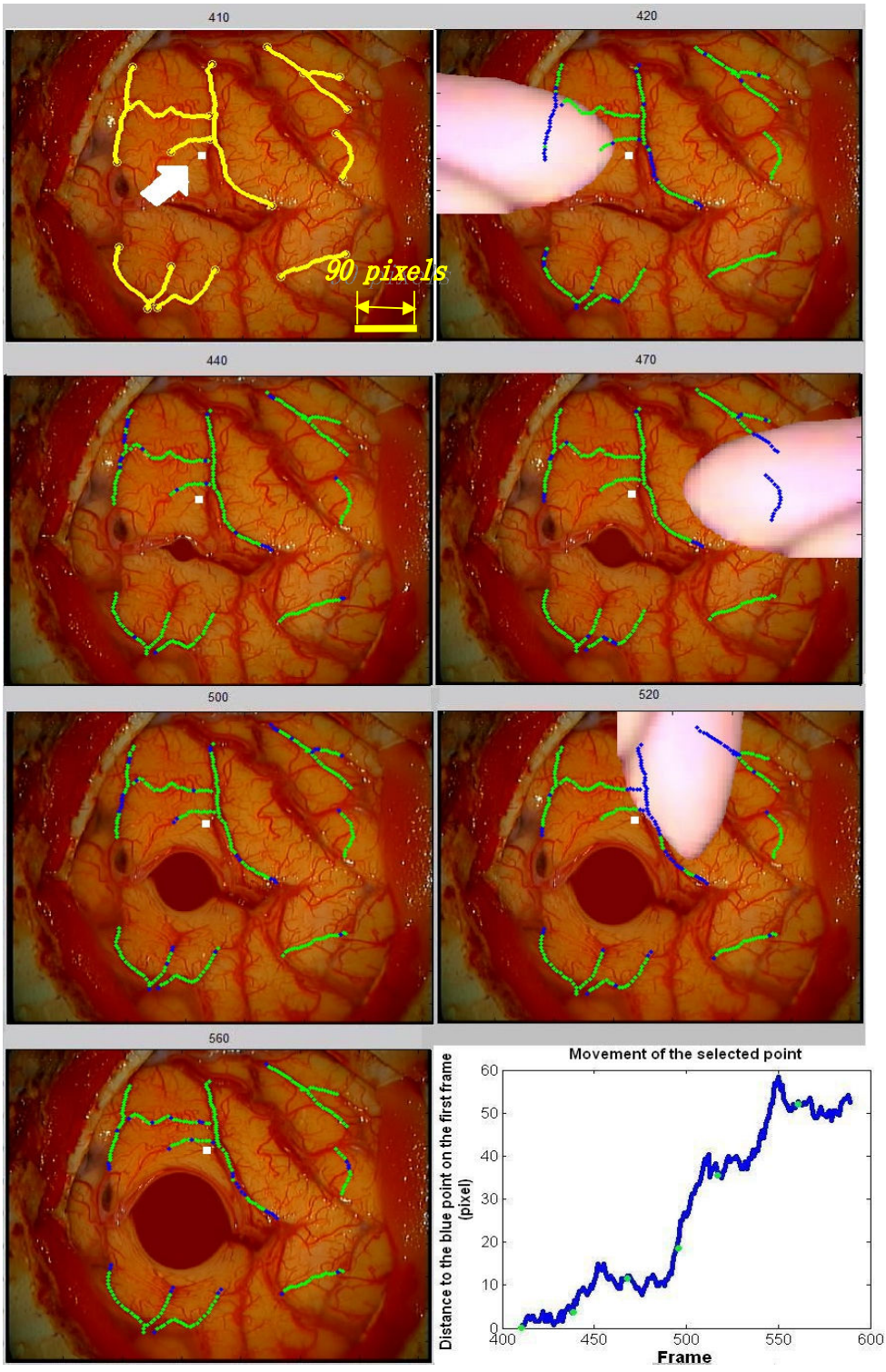

Fig.V.5: Simulation of occlusions caused by surgical instruments entering and leaving the field of view and of a cavity caused by a resection. Selected vessels are shown in yellow on the first frame. Estimated vessel location is shown in green on the other frames. The blue segments indicate segments for which no correspondence was found. The bottom right panel shows the displacement of the white point indicated by an arrow on the upper left frame.

5.4.3. Qualitative results obtained on real image sequences

In this section results obtained for selected patient sequences are presented to illustrate the type of images included in the study. Fig.V.6 shows several frames in one sequence acquired for the first patient. In this sequence, a surgical instrument appears in the field of view. The vessels selected in the first frame are shown in yellow. Tracking results are shown in green in the other frames. Points shown in yellow are points that are not used for registration purposes but define targets used in the quantitative study (see next section). As was the case in the simulated images, the algorithm is capable of tracking selected vessels despite the partial occlusion caused by the surgical instruments and the cortical deformation caused by the resection. A close inspection of frame 120 in Fig.V.6 shows a light yellow square on the right corner of the image. This is the logo of the Zeiss microscope, which is occasionally projected onto the image and causes artifacts. As discussed above, the vesselness component of the feature matrix is evaluated on the first frame of the video sequence and fixed for the entire sequence. This is done because it is assumed that the shape characteristics of the vessels do not change from frame to frame. The R, G, and B values, on the other hand, are updated as the algorithms moves from one frame to the other. This permits the adaptation of the color characteristics to, for instance, change in lighting conditions. Here, the algorithm is immune to the artifact caused by the Zeiss logo because it appears in the video gradually and the R, G, and B values of the similarity matrix are adapted.

Fig.V.7 shows several frames in one of the second patient's sequences. In this sequence, a relatively fast, medium amplitude motion was observed between frames. Vessel segments identified on the first frame and shown in yellow are tracked over 400

frames. Here, the algorithm was able to track all the active points and tracking results are shown in green. Again, the yellow points designate the intersection of small vessels not used in the registration process. Visual inspection shows that the yellow target points are tracked accurately and demonstrate the accuracy of the method over the entire frame. As was the case in the previous sequence, a surgical instrument appears in the last sample frame without affecting the tracking process.

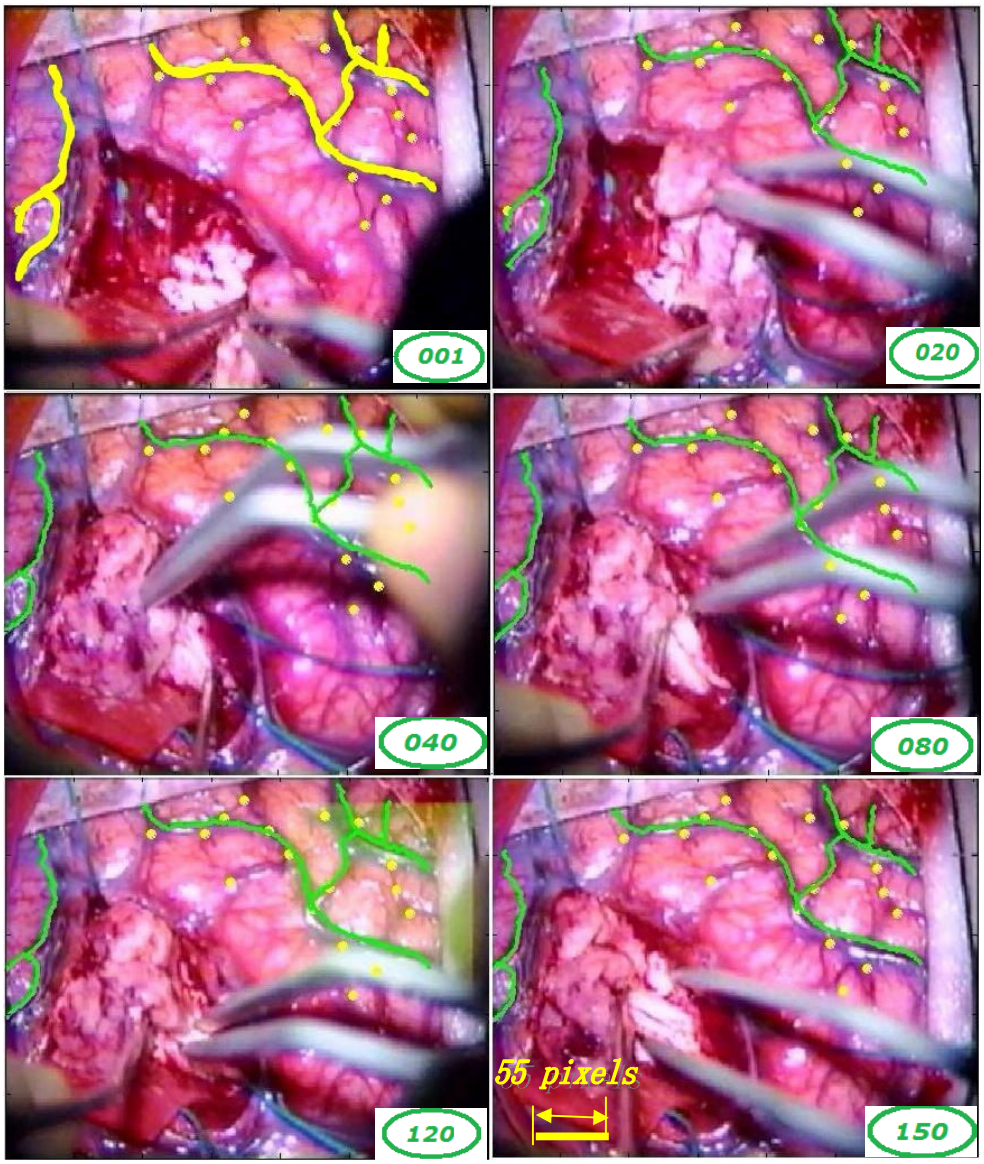

Fig.V.6: Tracking of sample frames in one video sequence of patient 1.

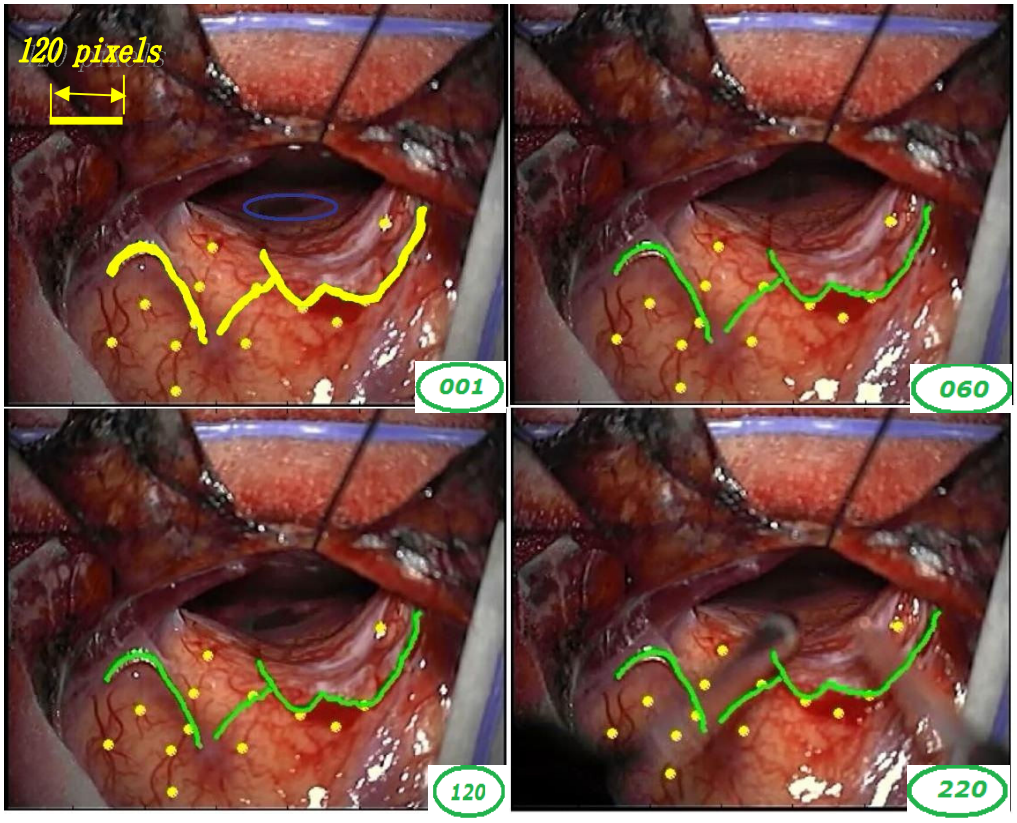

Fig.V.7: Tracking of sample frames in one video sequence of patient 2.

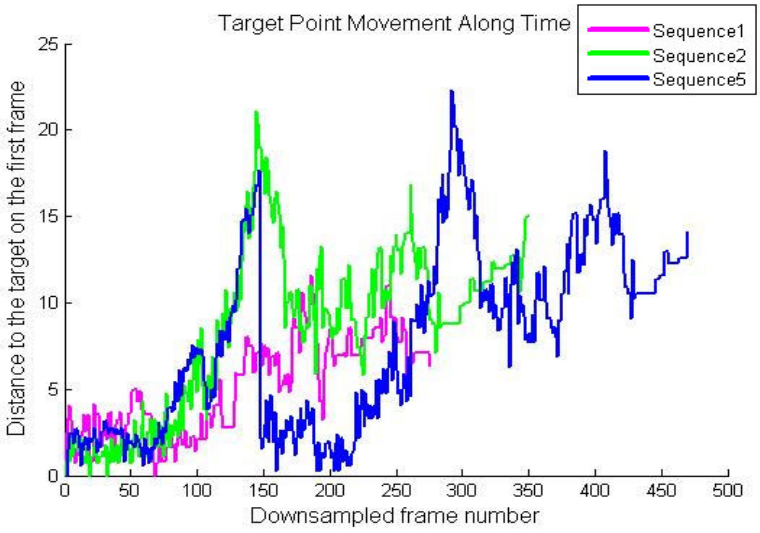

Fig.V.8: Frame-to-frame displacement of one landmark point in three sequences pertaining to patient 1 (sequences 1, 2, and 5).

To provider the reader with a sense of the inter-frame and total motion observed in the sequences used herein, which is difficult to convey with static images, Fig.V.8. plots the displacement of one voxel in each of three sequences pertaining to patient 1 (sequences 1, 2, and 5).

5.4.4. Quantitative evaluation

To evaluate the approach quantitatively, two measures have been used: the Vessel Tracking Error (VTE) and the Target Registration Error (TRE). The vessel tracking error is computed for vessel segments tracked from frame to frame and is defined as the average distance between the true vessel position and the position of the vessel found by the algorithm. To compute this error, a human operator first selects starting and ending points of vessels segments in the first frame of the sequence. These vessel segments are chosen such that they cover a major portion of the image. The vessel segmentation algorithm in Chapter III connects the starting and ending points to create the set of vessel segments that are tracked. The human operator also selects the starting and ending points for the same vessel segments in four additional frames positioned at 25%, 50%, 75%, and 100% of the sequence. Both the vessel segments selected by the human rater and those produced by the algorithm on these frames are then parameterized. N equidistant samples with N equal to the number of active points for a segment are subsequently selected on corresponding segments. This produces two sets of homologous points V_i and U_i. The Vessel Tracking Error is defined as

$$VTE = \frac{1}{n}\sum_{i=1}^{n}\sqrt{(\mathbf{V_i}-\mathbf{U_i})^T(\mathbf{V_i}-\mathbf{U_i})}, \quad (18)$$

i.e., it is the mean Euclidean distance between homologous points on vessel segments. The target registration error [86] is the registration error obtained for points that are not used to register the frames. These are points, typically intersections of small vessels, which are selected by the human operator in the first frame and then in the four other frames in which the vessels have been selected (see selected points in Fig.V.6 and Fig.V.7). While selecting the target points, magnification of the images was allowed. To evaluate target localization error, a few sequences were selected on which landmarks were selected several time. Target localization error was sub-voxel and considered to be negligible. For those points, the target registration error is defined as follows:

$$TRE_i = \sqrt{(\mathbf{T}(\mathbf{X_i})-\mathbf{Y_i})^T(\mathbf{T}(\mathbf{X_i})-\mathbf{Y_i})}, \quad (19)$$

in which $\boldsymbol{X_i}$ and $\boldsymbol{Y_i}$ are the points selected in the first frame and the four sampled frames, respectively. $\boldsymbol{T}$ is the transformation obtained by concatenating all the elementary transformations obtained from tracking each frames.

Table.V.2 lists the vessel tracking errors computed for the 21 video sequences. Sequences 1 to 7 pertain to patient 1, sequences 8 to 14 are to patient 2, and sequences 15 to 21 to patient 3. Results pertaining to patient 3 have been computed differently than those of patient 1 and 2. Rather than parameterizing vessel segments, we computed correspondence between manually segmented and automatically localized vessel segments using closest point distance. This metric is not sensitive to vessel translation. Unfortunately, data pertaining to patient 3 was lost and could not be reprocessed. Based on our observations for the other two patients, our current distance measure adds, in average, one pixel to our previous measure. Overall statistics have thus been reported in

two groups. The first contains patient 1 and 2, the other contains patients 3. The tracking error for each video sequence reported in the "mean" column is computed as the mean of the vessel tracking errors in the 4 sampled frames.

Across the 14 sequences for which we compute the VTE as described above, the mean VTE is 2.45 pixels with a standard deviation of 0.58 pixels. With the spatial resolution of the images, this leads to a mean VTE of 0.3 (high resolution sequences) or 0.6 (low resolution sequences) mm. The second column from the right shows the number of vessel segments tracked in each of the video sequences. This number varies from 11 in sequences in which a large number of vessels are visible, e.g., sequence 3, to 5 in sequences in which only a few vessels are visible, e.g., sequence 13. The number of vessel segments across sequences for a particular subject may change, e.g., from sequence 1 to sequence 7. This is due to the fact that videos are taken over long periods of time at different phases of the procedure. Because of this, some vessels may disappear because of the resection or be covered by cotton pads during the entire sequence; these vessels cannot be tracked in the sequence. The last column in the table is the number of frames in each video sequence.

In Table.V.3, the target registration error is reported for all the video sequences. As was done above, the average TRE for each video sequence reported in the "mean" column is computed as the mean of the target registration errors in the 4 sampled frames. The overall mean (3.34 pixels), median (2.88 pixels), standard deviation (1.52 pixels) TRE are also reported. The overall mean TRE is thus approximately 0.4 or 0.8 mm, depending on the spatial resolution of the images. As expected, the TRE is larger than the VTE because it is computed with points that are not used to estimate the transformations

used to register the frames. The last column of the table shows the number of target points that have been selected for each of the video sequences. Again, more points have been selected on some sequences than others because some sequences have more vessels and thus identifiable target points than others. As many as 15 points have been selected for some sequence, e.g. sequence 19. The lowest number of target points is 6 for sequence 10. For this sequence, one also observes that the TRE is relatively large. In this sequence, the microscope was focused on the bottom of the cavity left after the resection. The cortical surface was thus blurry, which affected the accuracy of the tracking algorithm.

Table.V.2: VTE (IN PIXELS) for 21 video sequences

	25 %	50 %	75 %	100 %	Mean	Std	# V	# Frames
1	2.26	2.47	2.78	2.55	2.51	0.21	9	285
2	1.48	2.48	2.09	2.67	2.18	0.52	10	350
3	2.46	1.89	2.46	2.93	2.43	0.42	11	680
4	2.03	2.18	3.18	2.48	2.46	0.51	9	520
5	1.6	2.50	3.52	2.36	2.49	0.78	6	470
6	1.84	3.64	3.00	2.54	2.75	0.75	8	435
7	1.84	2.67	3.19	2.56	2.56	0.55	6	485
8	2.71	2.14	2.35	2.00	2.3	0.39	8	990
9	1.42	2.11	2.22	1.73	1.87	0.36	7	1190
10	2.46	2.0	3.64	4.54	3.16	1.15	6	585
11	2.79	2.83	2.14	2.63	2.59	0.31	6	815
12	2.40	2.12	1.44	1.71	1.91	0.42	6	945
13	2.11	2.56	2.95	2.29	2.47	0.36	5	925
14	3.11	2.04	2.58	2.71	2.61	0.44	8	1275
15	1.18	1.15	1.71	1.59	1.41	0.29	7	160
16	0.44	0.84	1.37	1.31	0.99	0.35	7	210
17	1.16	1.24	1.65	1.36	1.35	0.39	7	180
18	1.54	1.42	1.79	3.39	2.04	0.15	5	165
19	0.85	1.49	2.08	1.15	1.38	0.53	6	180
20	1.02	1.69	1.05	1.17	1.23	0.17	7	220
21	0.82	0.94	1.04	0.97	0.94	0.32	8	340
patient 1 and 2			Overall mean		**2.45**	overall std		0.58
patient 3			Overall mean		**1.33**	overall std		0.54

Table.V.3: TRE (IN PIXELS) for 21 video sequences

	25%	50%	75%	100%	Mean	Std	# Targets
1	1.77	2.1	2.54	2.29	2.18	0.32	11
2	1.85	2.19	2.9	2.09	2.26	0.45	13
3	1.97	2.36	2.83	1.43	2.15	0.59	11
4	3.32	4.2	2.76	5.5	3.95	1.19	8
5	1.97	2.3	2.61	2.37	2.31	0.26	8
6	2.34	4.17	2.94	3.28	3.18	0.76	10
7	2.13	2.74	2.33	2.57	2.44	0.27	10
8	2.05	5.91	5.11	4.06	4.28	1.67	8
9	1.86	2.91	3.72	4.79	3.32	1.24	9
10	7.79	9.7	8.62	6.26	8.09	1.45	6
11	3.24	3.03	2.77	3.09	3.03	0.2	7
12	2.18	2.57	2.62	2.7	2.52	0.23	9
13	2.88	5.09	4.88	3.72	4.14	1.04	8
14	2.04	3.46	5.82	5.34	4.17	1.74	6
15	1.86	2.11	2.91	2.84	2.43	0.52	13
16	2.55	3.64	2.3	2.39	2.72	0.62	13
17	3.67	1.67	3.49	4.13	3.24	1.08	13
18	3.52	2.81	2.85	3.44	3.16	0.38	13
19	4.51	3.99	1.98	1.99	3.12	1.32	15
20	3.47	3.13	2.88	2.71	3.05	0.33	14
21	2.95	5.04	4.88	4.79	4.42	0.98	13
overall mean		3.34	overall median				2.88
overall std		1.52	average # of targets				10

5.4.5. Parameter sensitivity test

Three main parameters need to be selected in our approach, i.e., the profile radius r, the searching threshold s_r, and the similarity threshold. These were selected heuristically on a few sequences and then used without modifications on the others. To illustrate the sensitivity of the results on the parameter values one sequence was first selected (sequence # 3). The algorithm was then applied to this sequence with parameter values ranging from 80% to 120% of the original values. Parameter values were perturbed sequentially. Fig.V.9 shows the TRE values that were obtained on the four

evaluation frames used for this sequence. These results show that, albeit some variations can be observed when the parameters are adjusted, the results remain within a tight range.

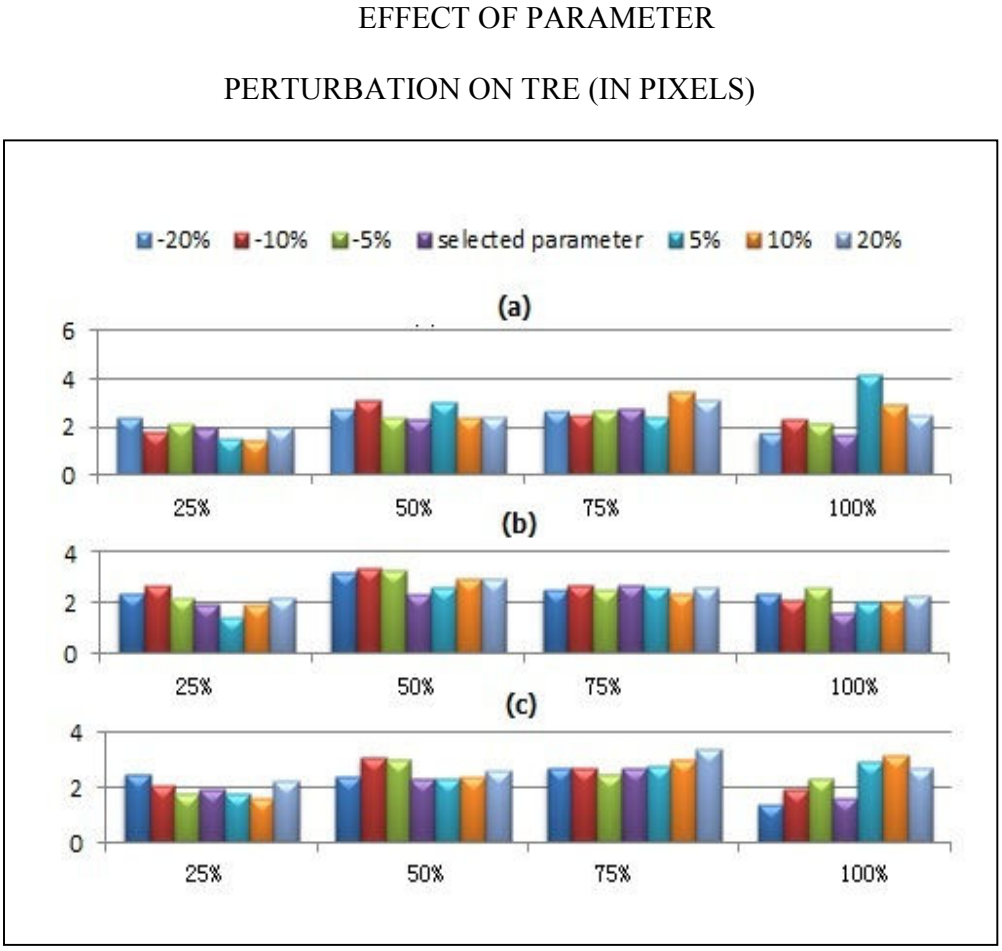

Fig.V.9: TRE values obtained for sequence #3 when perturbing the value of the three main parameters used in the algorithm: the profile radius (top panel), the searching radius (middle panel), and the threshold (bottom panel). In each case values were perturbed in a 80%-120% range.

5.5. Discussion

In this chapter, a method has been proposed to track brain motion in video streams. Coupled with a laser range scanner, this could permit estimating intraoperative brain shift automatically. The results we have presented indicate that this method is capable of tracking vessels even when surgical instruments obscure parts of the images. It is relatively simple, which makes it fast and applicable in real time (a MATLAB implementation takes about 1sec./frame but the algorithm does not need to be applied to every frame). The method has been used on 21 video sequences comprising 11405 frames. As the results demonstrate, the method is able to track the features in all of these sequences accurately. Tracking was less accurate in one of the sequences in which the cortical surface was blurry because the microscope was focused on deeper brain structures.

The closest work to ours is the work by Paul et al. [103, 104] and comparison with published work is difficult without being able to apply techniques on the same data sets. But, as discussed in the introduction section, their approach and ours is substantially different. They need to create a surface from video pairs and then register surfaces acquired at different times. We circumvent the need for surface registration by using a laser range scanner that provides us with both a 2D image and the 3D coordinates of the pixels in this image. Another difference is the fact that we rely on the entire vessels and on frame to frame registration for tracking rather than on a few isolated pixels. The fact that we register the entire frame based on the available information allows us to compute a transformation that is relatively accurate over occluded regions and wait for points to become visible again to refine the transformation over these regions. Paul et al. report

that their method is robust to occlusion. Again, we found it difficult to compare their results with ours because we could not ascertain from the results they report which points were occluded and for how long.

As discussed in the background section, the goal of this work is to use intraoperative video sequences to register laser range scanner images obtained at somewhat distant intervals during the procedure. To the best of our knowledge, this is the first attempt at doing so and the method described herein is a step in that realization but work remains. For example, while it has been shown that tracking vessels within a continuous video stream is achievable, tracking discontinuous sequences that are separated by relatively long intervals may require an additional inter-sequence registration step. Because the intraoperative microscope is currently not tracked, inter-sequence registration necessitates first computing a transformation to correct for differences in pose or magnification between sequences, which can be done by localizing a few common points in both sequences and computing a global transformation. If the last frame in a sequence and the first frame in the next sequence are very different, e.g., if the first sequence is acquired with the cortex intact and the next one after tumor resection, manual localization of a few vessels visible in both sequences may also be required.

While challenges remain, the results presented in this chapter suggest the value of intraoperative surgical microscope data. Coupling the tracking of microscope video sequences with 3D laser range scan data to characterize deformation during surgery could provide a detailed understanding of the changes in the 'active surgical' surface that are at the focus of therapy.

CHAPTER VI

SUMMARY AND FUTURE WORK

This dissertation presents several innovative methods in the area of intraoperative brain shift estimation. In Chapter II, it starts by showing, on five image volumes, that a 2D registration method is preferable to a 3D registration method when LRS data is used to estimate displacement. Then, it proposes a semi-automatic method for the registration of images acquired before and after tumor resection. This method, which relies on the registration of vessels that can be visualized in the pre- and the post-resection images, only requires the identification of starting and ending points for each vessel segment. An optimal path finding algorithm connects those vessel segments automatically using a cost map built with intensity information. Once vessels are identified, they are registered using a robust point-based nonrigid registration algorithm. The transformation computed with the vessels is then applied to the entire image. This permits to establish a complete correspondence between the pre- and post-resection three-dimensional LRS data. Experiments show that this semi-automatic method is robust to operator errors in localizing homologous points and a quantitative evaluation performed on 10 surgical cases show submillimetric registration accuracy. In Chapter IV, a method is presented to

automate the vessel segmentation process further. This method involves several steps: (1) correction of lighting artifacts, (2) vessel enhancement, and (3) vessels' centerline extraction. Results obtained on 5 images acquired in the operating room suggest that our method is robust and is able to segment vessels reliably. Although the original purpose of this technique was to permit the fully automatic registration of the pre- and post-resection images, it was realized that the very large differences in these images caused by the surgical process made their registration very difficult. A possible solution is to use intraoperative video images as a means to establish correspondence between static LRS images because inter-frame differences are relatively small in the video sequences, which facilitates vessel tracking. In Chapter V, a new video tracking algorithm is designed to track automatically cortical vessels in intraoperative microscope video sequences. This method works in three steps. First, models of vessels selected in the first frame of the sequence are built. These models are then used to track vessels across frames in the video sequence. Finally, displacements estimated using the vessels are extrapolated to the entire image. This tracking method has been tested on images simulating large displacement, tumor resection, and partial occlusion by surgical instruments and on 21 video sequences comprising several thousand frames acquired from three patients. Qualitative results show that it is accurate, robust to the appearance and disappearance of surgical instruments, and capable of dealing with large differences in images caused by resection. Quantitative results show a mean vessel tracking error of 2.4 pixels (0.3 or 0. 6 millimeters, depending on the spatial resolution of the images) and an average target registration error of 3.3 pixels (0.4 or 0.8 millimeters).

Even though we have made substantial progress towards developing a method that will permit the estimation of intraoperative cortical brain shift, work remains. In current practice, videos are not acquired as a continuous stream throughout the procedure. Between video segments, the appearance of the images may change greatly, i.e., some of the vessels may have been resected, cotton pads or other surgical instrument may obscure parts of the tracking vessels permanently, or the color of the images may change because of bleeding. All these differences make the registration of inter-video sequences difficult and the automation of this process has not been achieved. As a partial solution, a graphical user interface described below has been developed to permit the semi-automatic registration of these sequences.

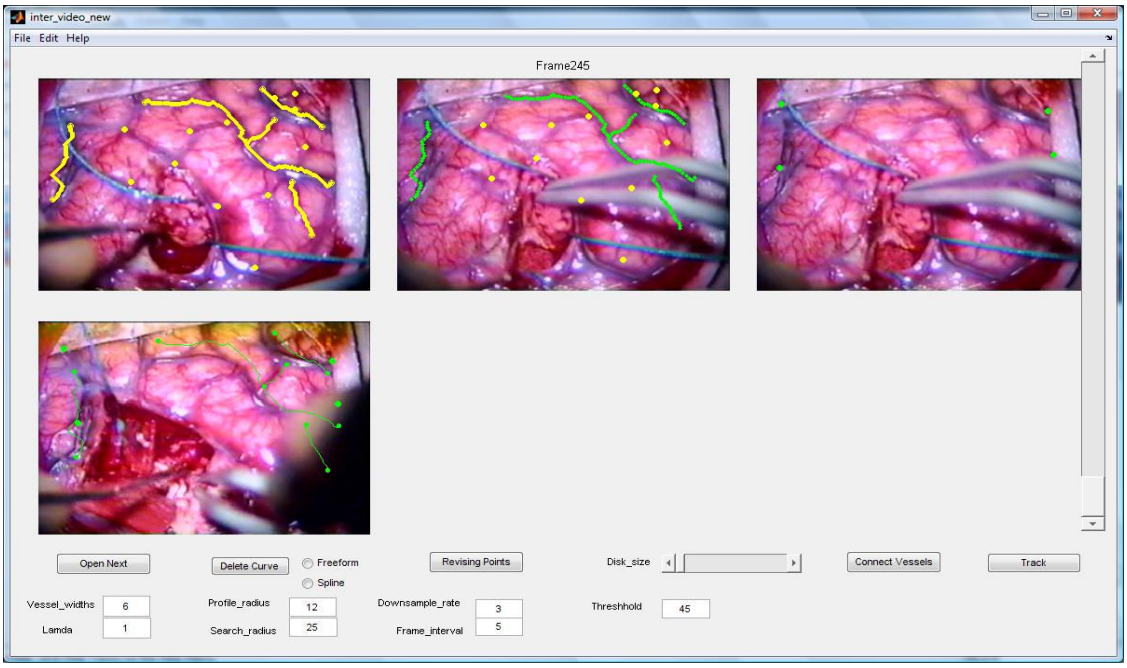

Fig.VI.1: Vessel tracking in the inter-video tracking GUI.

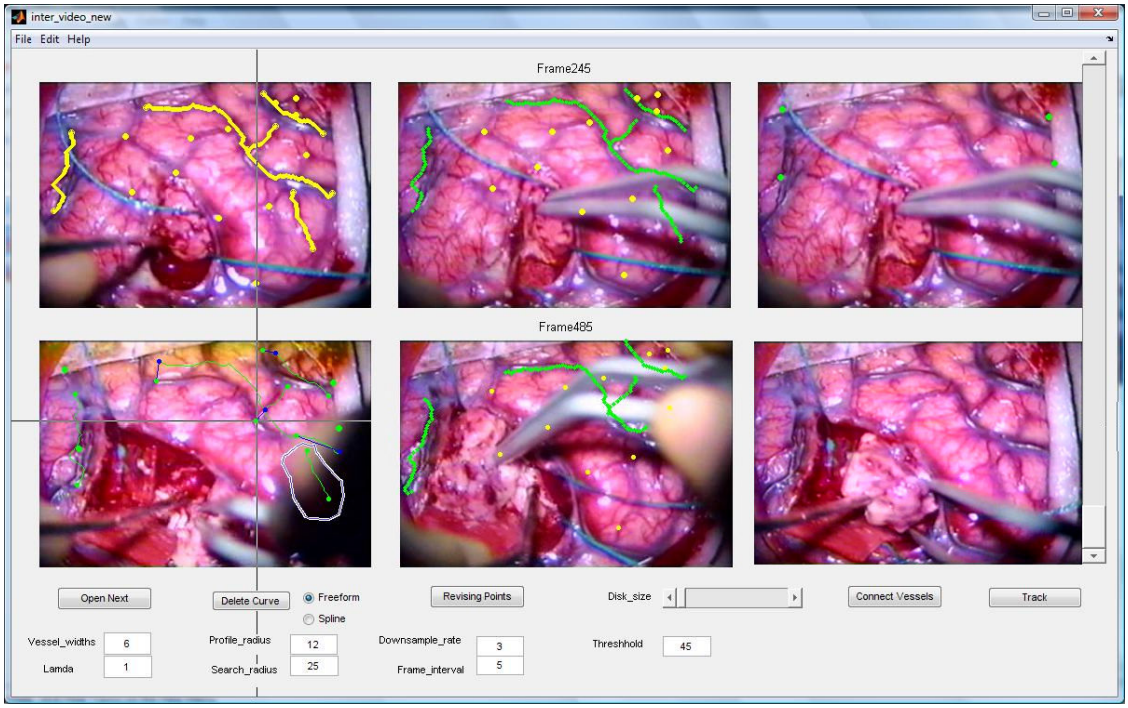

Fig.VI.2: Editing vessels in the inter-video tracking GUI.

Fig.VI.1 shows a screenshot of the semi-automatic inter-video registration system. The top left panel shows the first frame in a video sequence. Starting and ending points for the vessels are localized and the vessels are segmented. Yellow points are the target points used for evaluation. The top middle panel shows the results of the tracking, i.e., it is a dynamic panel that shows the tracked vessels on successive frames as the algorithm progresses through the sequence. The top right panel shows the last frame of this sequence and the bottom left panel shows the first frame of the next video sequence. Four points visible both in the top right and the bottom left panels are selected. A projective registration is computed between the 4 points shown on the top right panel and the 4 points shown on the bottom left panel. The vessels used for tracking are projected from the last frame in the first sequence to the first frame on the next one using this projective transformation, and displayed on the bottom left panel. But the projective registration is

not always sufficient to compensate for the nonrigid deformation occurring between video sequences. In addition, parts of some vessel may be occluded, or new ones may appear in the field of view. To compensate for these differences, starting and ending points for the vessels can be adjusted, vessel segments can be deleted, or new ones added using GUI tools developed for this purpose.

The bottom left panel of Fig.VI.2, illustrates the process. To delete a curve or part of a curve, one simply draws a closed contour around. If the curve is translated, one can drag the starting or ending point to a new position (blue points and lines) and reconnect them using the minimal cost path method presented in Chapter III. The bottom middle panel in this image shows the progress of the algorithm as it works from frame to frame in video sequence 2. The bottom right panel shows the last frame of this sequence. The interface permits scrolling to accommodate the third sequence, and the process is repeated until the end of the last sequence in a series.

In Fig.VI.3, we illustrate tracking across seven video sequences for one of patients. The top left image shows the tracked vessels in yellow. Those vessels are successfully tracked until the very last frame of that sequence, which is shown in the top middle panel. The top right panel is also the last frame of that sequence with four green points chosen to compute the projective transformation to register the first sequence to the next. The second row shows the second video sequence. A cotton pad enters the craniotomy, and one of the vessels is occluded so it could be deleted from tracking. The middle image in that row shows the last frame in sequence two with the vessels that have been tracked. In the third row, another cotton pad and a retractor appear and occlude more vessels, but one more vessel is spotted and added to the set of tracked vessels. The

fourth sequence tracks the same vessels the third sequence does, but this sequence is a little bit out of focus, as one could tell from the images. In the fifth row, two more vessels are added. In the last row, three vessels could be deleted but two more vessels could be added, as shown in the figure.

Although such an interface shows the feasibility of tracking vessels through long periods of time it is not ideal for clinical use. Several things could be done to improve the process further. First, the microscope could be tracked. This would alleviate the need to localize homologous points on successive sequences to register those. Another possibility is to gather a continuous video stream. In current practice, recordings are not made during the entire procedure even when the microscope is. This is so because videos are stored in the microscope and capacity of the storing device is limited. A possibility is to connect a computer with a frame grabber to the video output of the microscope. This approach is currently being investigated.

Before they become clinically useable, the various methods proposed in this work also need to be better integrated and the complete process validated. In particular, the accuracy of the complete LRS-video-LRS process for cortical displacement estimation needs to be assessed. This could be done, for instance, by using a tracked probe in the operating room. This would permit localizing a few points on the cortical surface prior to resection and the same points after resection. Displacements measured with the tracked probe could thus be compared to the displacements measured with the method we propose.

Even though, the solution that has been presented in this work is not the final one, it is hoped that it will be a valuable contribution toward solving the problem of intraoperative brain shift estimation and to the broader image-guided therapy field.

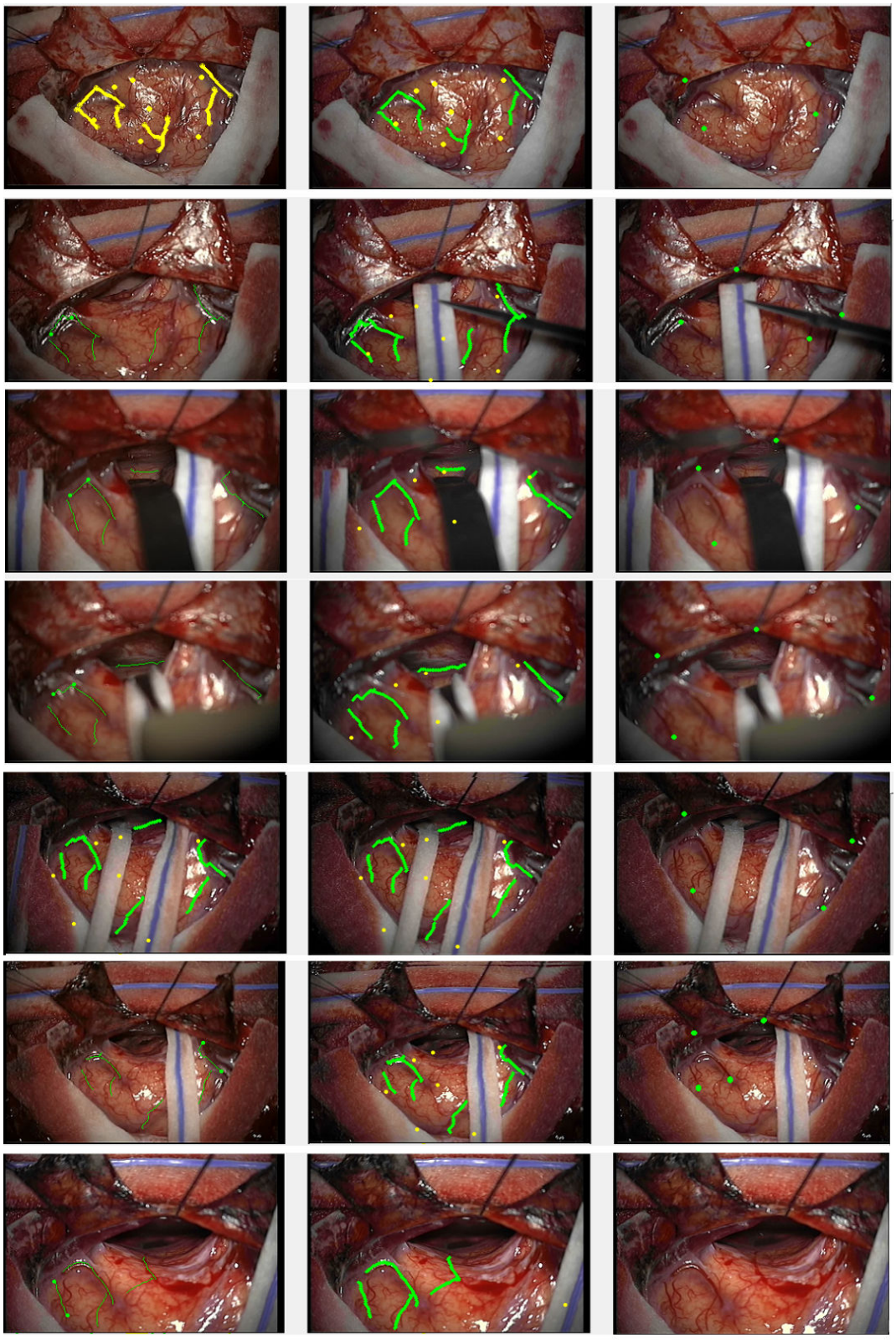

Fig.VI.3: Inter-video tracking of 7 video sequences acquired for a subject.

REFERENCES

[1] M. J. Horner, L. A. G. Ries, M. Krapcho, N. Neyman, R. Aminou, N. Howlader, S. F. Altekruse, E. J. Feuer, L. Huang, A. Mariotto, B. A. Miller, D. R. Lewis, M. P. Eisner, D. G. Stinchcomb, and B. K. Edwards, "SEER Cancer Statistics Review," N. C. Institute, Ed., 1975-2006.

[2] H. J. Nauta, "Error assessment during 'image guided' and 'imaging interactive' stereotactic surgery," *Computerized Medical Imaging and Graphics,* vol. 18, pp. 279-87, Aug. 1994.

[3] C. Nimsky, O. Ganslandt, S. Cerny, P. Hastreiter, G. Greiner, and R. Fahlbusch, "Quantification of, visualization of, and compensation for brain shift using intraoperative magnetic resonance imaging," *Neurosurgery,* vol. 47, pp. 1070-1079, 2000.

[4] D. W. Roberts, A. Hartov, F. E. Kennedy, M. I. Miga, and K. D. Paulsen, "Intraoperative brain shift and deformation: A quantitative clinical analysis of cortical displacements in 28 cases," *Neurosurgery,* vol. 43, pp. 749-760, 1998.

[5] C. Davatzikos, D. Shen, A. Mohamed, and S. K. Kyriacou, "A framework for predictive modeling of anatomical deformations " *IEEE Transactions on Medical Imaging,* vol. 20, pp. 836-843, Aug. 2001.

[6] M. Ferrant, A. Nabavi, B. Macq, F. A. Jolesz, R. Kikinis, and S. K. Warfield, "Registration of intraoperative MR images of the brain using a finite-element biomechanical model," *IEEE Transcations on Medical Imaging* vol. 20, pp. 1384-1397, Dec. 2001.

[7] A. Hagemann, K. Rohr, H. S. Stiehl, U. Spetzger, and J. M. Gilsbach, "Biomechanical modeling of the human head for physically based, nonrigid image registration," *IEEE Transactions on Medical Imaging,* vol. 18, pp. 875-884, Oct. 1999.

[8] M. I. Miga, K. D. Paulsen, P. J. Hoopes, F. E. Kennedy, A. Hartov, and D. W. Roberts, "In vivo quantification of a homogeneous brain deformation model for updating preoperative images during surgery," *IEEE Transactions on Biomedical Engineering,* vol. 47, pp. 266-273, Feb. 2000.

[9] M. I. Miga, K. D. Paulsen, F. E. Kennedy, P. J. Hoopes, A. Hartov, and D. W. Roberts, "In vivo analysis of heterogeneous brain deformation computations for model-updated image guidance " *Computer Method in Biomechanics and Biomedical Engineering,* vol. 3, pp. 129-146, Feb. 2000.

[10] M. I. Miga, D. W. H. Roberts, A, S. Eisner, J. Lemery, F. E. Kennedy, and K. D. Paulsen, "Updated neuroimaging using intra-operative brain modeling and sparse data," in *Proceedings of the Meeting of the American Society for Stereotactic and Functional Neurosurgery* Snowbird, Utah, 1999, pp. 103-106.

[11] K. D. Paulsen, M. I. Miga, F. E. Kennedy, P. J. Hoopes, A. Hartov, and D. W. Roberts, "A computational model for tracking subsurface tissue deformation during stereotactic neurosurgery," *IEEE Transactions on Biomedical Engineering,* vol. 46, pp. 213-225, Feb. 1999.

[12] N. Archip, O. Clatz, S. Whalen, D. Kacher, A. Fedorov, A. Kot, N. Chrisochoides, F. Jolesz, A. Golby, P. M. Black, and S. K. Warfield, "Non-rigid alignment of pre-operative MRI, fMRI, and DT-MRI with intra-operative MRI for enhanced visualization and navigation in image-guided neurosurgery," *NeuroImage,* vol. 35, pp. 609-624, Apr. 2007.

[13] O. Clatz, H. Delingette, I. Talos, A. J. Golby, R. Kikinis, F. A. Jolesz, N. Ayache, and S. K. Warfield, "Robust non-rigid registration to capture brain shift from intra-operative MRI," *IEEE Transactions on Medical Imaging,* vol. 24, pp. 1417-1427, Nov. 2005.

[14] M. Ferrant, A. Nabavi, B. Macq, P. M. Black, F. A. Jolesz, R. Kikinis, and S. K. Warfield, "Serial registration of intra-operative MR images of the brain," *Medical Image Analysis,* vol. 6, pp. 337-59, Dec. 2002.

[15] A. Nabavi, P. M. Black, D. T. Gering, C. F. Westin, V. Mehta, R. S. Pergolizzi, M. Ferrant, S. K. Warfield, N. Hata, R. B. Schwartz, W. M. Wells, R. Kikinis, and F. A. Jolesz, "Serial intra-operative magnetic resonance imaging of brain shift," *Neurosurgery,* vol. 48, pp. 787-97, Apr. 2001.

[16] M. N. Pamir, S. Peker, M. M. Özek, and A. Dinçer, *Intra-operative MR imaging: preliminary results with 3 tesla MR system* vol. 98: Springer Vienna, 2006.

[17] "http://neurosurgery.mgh.harvard.edu/NeuroScience/mobileCT.htm."

[18]"http://www.brainlab.com/scripts/website_english.asp?menuDeactivate=0&articleID=2259&articleTypeID=261&pageTypeID=4&article_short_headline=BrainSUITE%AE%20iCT."

[19] "http://www.xorantech.com/contentHTML/xCAT.php."

[20] L. D. Lunsford, D. Kondziolka, and D. J. Bissonette, "Intraoperative imaging of the brain," *Stereotactic and Functional Neurosurgery,* vol. 66, pp. 58-64, 1996.

[21] T. Arbel, X. Morandi, M. Comeau, and D. L. Collins, "Automatic nonlinear mri-ultrasound registration for the correction of intra-operative brain deformations," in *Medical Image Computing and Computer-Assisted Intervention-MICCAI.* vol. 2208/2010 Netherlands: Springer-Verlag, 2001, pp. 913-922.

[22] R. M. Comeau, A. F. Sadikot, A. Fenster, and T. M. Peters, "Intra-operative ultrasound for guidance and tissue shift correction in image-guided neurosurgery," *Medical Physics,* vol. 27, pp. 787-800, Apr. 2000.

[23] P. Coupé, P. Hellier, X. Morandi, and C. Barillot, "A probabilistic objective function for 3d rigid registration of intra-operative US and pre-operative MR brain images," in *IEEE International Symposium on Biomedical Imaging: From Nano to Macro* Washington DC, USA, 2007, pp. 1320-1323.

[24] D. G. Gobbi, R. M. Comeau, and T. M. Peters, "Ultrasound/MRI overlay with image warping for neurosurgery," in *Medical Image Computing and Computer-Assisted Intervention-MICCAI*, Pittsburgh, PA, USA, 2000, pp. 29-53.

[25] N. S. Hata, M, T. Dohi, H. Iseki, K. Takakura, and D. Hashimoto, "Registration of ultrasound echography for intra-operative use: a newly developed multiproperty method," in *Visualization in Biomedical Computing*, Rochester, MN, USA 1994, pp. 251-259.

[26] A. P. King, J. M. Blackall, G. P. Penney, P. J. Edwards, D. L. G. Hill, and H. D. J, "Bayesian estimation of intra-operative deformation for image-guided surgery using 3-D ultrasound," in *Medical Image Computing and Computer-Assisted Intervention-MICCAI*, Pittsburgh, PA, USA, 2000, pp. 588-597.

[27] M. M. J. Letteboer, M. A. Viergever, and W. J. Niessen, "Rigid registration of 3D ultrasound data of brain tumors," in *Computer Assisted Radiology and Surgery*, London, UK, 2003, pp. 433-439.

[28] M. M. J. Letteboer, P. W. A. Willems, M. A. Viergever, and W. J. Niessen, "Brain shift estimation in image-guided neurosurgery using 3-D ultrasound," *IEEE Transactions on Medical Imaging,* vol. 52, pp. 268-276, Feb. 2005.

[29] B. C. Porter, D. J. Rubens, J. G. Strang, J. Smith, T. S, and P. K. J, "Three-Dimensional registration and fusion of ultrasound and mri using major vessels as fiducial markers," *IEEE Transactions on Medical Imaging,* vol. 20, pp. 354 - 359, Apr. 2001.

[30] I. Reinertsen, M. Descoteaux, K. Siddiqi, and D. L. Collins, "Validation of vessel-based registration for correction of brain shift," *Medical Image Analysis,* vol. 11, pp. 374-684, Aug. 2007.

[31] I. Reinertsen, F. Lindseth, G. Unsgaard, and D. L. Collins, "Clinical validation of vessel-based registration for correction of brain-shift," *Medical Image Analysis,* vol. 11, pp. 673-684, Dec. 2007.

[32] A. Roche, X. Pennec, G. Malandain, and N. Ayache, "Rigid registration of 3D ultrasound with MR images: a new approach combining intensity and gradient information," *IEEE Transactions on Medical Imaging,* vol. 20, pp. 1038-1049, Oct. 2001.

[33] J. Trobaugh, W. Richard, K. Smith, and R. Bucholz, "Frameless stereotactic ultrasonography: Methods and applications," *Computerized Medical Imaging and Graphics,* vol. 18, pp. 235-246, Jul-Aug 1994.

[34] C. DeLorenzo, X. Papademetris, K. P. Vives, D. Spencer, and J. S. Duncan, "Combined feature/intensity-based brain shift compensation using stereo guidance," in *IEEE International Symposium on Biomedical Imaging: From Nano to Macro* Arlington, Virginia, USA, 2006, pp. 335- 338.

[35] C. DeLorenzo, X. Papademetris, K. Wu, K. P. Vives, D. Spencer, and J. S. Duncan, "Nonrigid 3D brain registration using intensity/feature information," in *Medical Image Computing and Computer-Assisted Intervention-MICCAI* Copenhagen, Denmark: Springer-Verlag, 2006, pp. 932-939.

[36] O. M. Skrinjar and J. S. Duncan, "Stereo-guided volumetric deformation recovery," in *IEEE International Symposium on Biomedical Imaging: From Nano to Macro* Washington DC, USA, 2002.

[37] H. Sun, K. E. Lunn, H. Farid, Z. Wu, A. Hartov, and K. D. Paulsen, "Stereopsis-guided brain shift compensation," *IEEE Transactions on Medical Imaging,* vol. 24, pp. 1039-1052, Feb. 2005.

[38] M. A. Audette, K. Siddidqi, F. P. Ferrie, and T. M. Peters, "An integrated range-sensing, segmentation and registration framework for the characterization of intra-surgical brain deformations in image-guided surgery," *Computer Vision and Image Understanding,* vol. 89, pp. 226-251, Feb. 2003.

[39] A. Cao, P. Dumpuri, and M. I. Miga, "Tracking cortical surface deformations based on vessel structure using a laser range scanner," in *IEEE International Symposium on Biomedical Imaging: From Nano to Macro* Washington, DC, USA, 2006.

[40] A. Cao, R. C. Thompson, P. Dumpuri, B. M. Dawant, R. L. Galloway, S. Ding, and M. I. Miga, "Laser range scanning for image-guided neurosurgery: Investigation of image-to-physical space registrations," *Medical Physics,* vol. 35, pp. 1593-1605, Apr. 2008.

[41] M. I. Miga, T. K. Sinha, D. M. Cash, R. L. Galloway, and R. J. Weil, "Cortical surface registration for image-guided neurosurgery using laser-range scanning," *IEEE Transactions on Medical Imaging,* vol. 22, pp. 973-985, Aug. 2003.

[42] T. K. Sinha, B. M. Dawant, V. Duay, D. M. Cash, R. J. Weil, R. C. Thompson, R. D. Weaver, and M. I. Miga, "A method to track cortical surface deformations using a laser range scanner," *IEEE Transactions on Medical Imaging,* vol. 24, pp. 767-781, Jun. 2005.

[43] T. K. Sinha, V. Duay, B. M. Dawant, and M. I. Miga, "Cortical shift tracking using laser range scanner and deformable registration methods," in *Medical Image*

Computing and Computer-Assisted Intervention-MICCAI, Montreal, Canada, 2003, pp. 166-174.

[44] G. L. Goualher, C. Barillot, and Y. Bizais, "Three-dimensional segmentation and representation of cortical sulci using active ribbons," *International Journal of Pattern Recognition and Artificial Intelligence,* vol. 11, pp. 1295-1315, 1997.

[45] S. Nakajima, H. Atsumi, R. Kikinis, T. M. Moriarty, D. C. Metcalf, F. A. Jolesz, and P. M. Black, "Use of Cortical surface vessel registration for image-guided neurosurgery," *Neurosurgery,* vol. 40, pp. 1201-1210, 1997.

[46] S. Ding, M. I. Miga, R. C. Thompson, P. Dumpuri, A. Cao, and B. M. Dawant, "Estimation of intra-operative brain shift using a laser range scanner," in *Engineering in Medicine and Biology Society-EMBS*, Lyon, France, 2007, pp. 848-851.

[47] P. J. Besl and N. D. McKay, "A method for registration of 3-d shapes," *IEEE Transactions on Pattern Analysis and Machine Intelligence,* vol. 14, pp. 239-256, Feb. 1992.

[48] G. K. Rohde, A. Aldroubi, and B. M. Dawant, "The adaptive bases algorithm for intensity-based nonrigid image registration," *IEEE Transactions on Medical Imaging,* vol. 22, pp. 1470-1479, Nov. 2003.

[49] S. Chaudhuri, S. Chatterjee, N. Katz, M. Nelson, and M. Goldbaum, "Detection of blood vessels in retinal images using two-dimensional matched filters," *IEEE Transactions on Medical Imaging,* vol. 8, pp. 263-269, Mar. 1989.

[50] J. Chen and A. A. Amini, "Quantifying 3-d vascular structures in MRA images using hybrid PDE and geometric deformable models," *IEEE Transactions on Medical Imaging,* vol. 23, pp. 1251-1262, Oct. 2004.

[51] A. Hoover, V. Kouznetsova, and M. Goldbaum, "Locating blood vessels in retinal images by piecewise threshold probing of a matched filter response," *IEEE Transactions on Medical Imaging,* vol. 19, pp. 203-210, Mar. 2000.

[52] T. Koller and G. Gerig, "Multiscale detection of curvilinear structures in 2d and 3d image data," in *Proceedings of the Fifth International Conference on Computer Vision* Cambridge, Massachusetts, USA, 1995, pp. 864-869.

[53] C. Lorenz and I. C. Carlsen, "Multi-scale line segmentation with automatic estimation of width, contrast and tangential direction in 2d and 3d medical images," in *First Joint Conference Computer Vision, Virtual Reality and Robotics in Medicine and Medical Robotics and Computer-Assisted Surgery* Grenoble, France: Springer-Verlag, 1997, pp. 233-242.

[54] Y. Sato and S. Nakajima, "3d multi-scale line filter for segmentation and visualization of curvilinear structures in medical images," in *First Joint*

Conference Computer Vision, Virtual Reality and Robotics in Medicine and Medical Robotics and Computer-Assisted Surgery, Grenoble, France, 1997, pp. 213-222.

[55] M. J. Cree, D. Cornforth, and J. H. F. Jelinek, "Vessel segmentation and tracking using a two-dimensional model," *Image and Vision Computing,* pp. 345-350, 2005.

[56] M. Lalonde, L. Gagnon, and M. C. Boucher, "Non-recursive paired tracking for vessel extraction from retinal images," in *Proc. Conf. Vision Interface*, Montreal, QC, Canada, 2000, pp. 61-68.

[57] I. Liu and Y. Sun, "Recursive tracking of vascular networks in angiograms based on the detection-deletion scheme," *IEEE Transactions on Medical Imaging,* vol. 12, pp. 334-341, Feb. 1993.

[58] Y. A. Tolias and S. M. Panas, "A fuzzy vessel tracking algorithm for retinal images based on fuzzy clustering," *IEEE Transactions on Medical Imaging,* vol. 17, pp. 263-273, Apr. 1998.

[59] X. Jiang and D. Mojon, "Adaptive local thresholding by verification based multithreshold probing with application to vessel detection in retinal images," *IEEE Transactions on Pattern Analysis and Machine Intelligence,* vol. 25, pp. 131-137, Jan. 2003.

[60] A. M. Mendonça and A. Campilho, "Segmentation of retinal blood vessels by combining the detection of centerlines and morphological reconstruction," *IEEE Transactions on Medical Imaging,* vol. 25, pp. 1200-1213, Sep. 2006.

[61] F. Zana and J. Klein, "Segmentation of vessel-like patterns using mathematical morphology and curvature evaluation," *IEEE Transactions on Image Processing,* vol. 10, pp. 1010-1019, Jul. 2001.

[62] M. Niemeijer, J. J. Staal, B. V. Ginneken, M. Loog, and M. D. Abramoff, "Comparative study of retinal vessel segmentation methods on a new publicly available database," in *Medical Imaging*, San Diego, CA, USA, 2004, pp. 648-656.

[63] E. Ricci and R. Perfetti, "Retinal blood vessel segmentation using line operators and support vector classification," *IEEE Transactions on Medical Imaging,* vol. 26, pp. 1357-1365, Oct. 2007.

[64] C. Sinthanayothin, J. Boyce, H. Cook, and T. Williamson, "Automated localisation of the optic disc, fovea and retinal blood vessels from digital colour fundus images," *British Journal of Ophthalmology,* vol. 83, pp. 902-910, 1999.

[65] J. V. B. Soares, J. J. G. Leandro, R. M. Cesar, J. H. F. Jelinek, and M. J. Cree, "Retinal vessel segmentation using the 2D Gabor wavelet and supervised

classification," *IEEE Transactions on Medical Imaging,* vol. 25, pp. 1214-1222, Sep. 2006.

[66] J. J. Staal, M. D. N. Abramoff, M, M. A. Viergever, and B. V. Ginneken, "Ridge based vessel segmentation in color images of the retina," *IEEE Transactions on Medical Imaging,* vol. 23, pp. 501-509, Apr. 2004.

[67] A. F. Frangi, W. J. Niessen, K. L. Vincken, and M. A. Viergever, "Multiscale vessel enhancement filtering," in *Medical Image Computing and Computer-Assisted Intervention-MICCAI*, Cambridge, MA,USA, 1998, pp. 130-137.

[68] C. M. V. Bemmel, L. J. Spreeuwers, M. A. Viergever, and W. J. Niessen, "Level-set-based artery-vein separation in blood pool agent CE-MR angiograms," *IEEE Transactions on Medical Imaging,* vol. 22, pp. 1224-1234, Oct. 2003.

[69] M. Jackowski, X. Papademetris, L. W. Dobrucki, A. J. Sinusas, and L. H. Staib, "Characterizing vascular connectivity from microCT images," in *Medical Image Computing and Computer-Assisted Intervention-MICCAI*, Cambridge, MA, USA 2005, pp. 701-708.

[70] C. Dorin and P. Meer, "Mean shift: a robust approach toward feature space analysis," *IEEE Transactions on Pattern Analysis and Machine Intelligence,* vol. 24, pp. 603-619, May 2002.

[71] M. Kass, A. Witkin, and D. Terzopoulous, "Snakes: Active contour models," in *International Conference on Computer Vision* London, UK, 1987, pp. 259-268.

[72] F. Leymarie and M. Levine, "Tracking deformable objects in the plane using an active contour model," *IEEE Transactions on Pattern Analysis and Machine Intelligence,* vol. 15, pp. 617-634, Jun. 1993.

[73] B. Lelieveldt, S. Mitchell, J. Bosch, R. V. Geest, M. Sonka, and J. Reiber, "Time-continuous segmentation of cardiac image sequences using active appearance motion models," in *Proceedings of the Information Processing in Medical Imaging*, Davis, CA, USA, 2001, pp. 446-452.

[74] T. Mcinerney and D. Terzopoulos, "A dynamic finite element surface model for segmentation and tracking in multidimensional medical images with application to cardiac 4D image analysis," *Computerized Medical Imaging and Graphics,* vol. 19, pp. 69-83, 1995.

[75] W. J. Niessen, J. S. Duncan, M. A. Viergever, and B. Romeny, "Spatiotemporal analysis of left ventricular motion," in *Medical Imaging*, San Diego, CA, USA 1995, pp. 250-261.

[76] A. Signh, L. V. Kurowski, and M. Chiu, "Cardiac MR image segmentation using deformable models," in *Medical Imaging*, Newport Beach, CA, USA, 1993, pp. 228-246.

[77] T. Cootes, C. Taylor, D. Cooper, and J. Graham, "Active shape models-their training and application," *Computer Vision and Image Understanding,* vol. 61, pp. 38-59, Jan 1995.

[78] A. M. Baumberg and D. C. Hogg, "An efficient method for contour tracking using active shape models," in *Proceeding of the Workshop on Motion of Nonrigid and Articulated Objects*, Austin, Texas, USA, 1994, pp. 194-199.

[79] Y. Su, M. H. Fisher, and R. S. Rowland, "Marker-less intra-fraction organ motion tracking using hybrid ASM," *International Journal of Computer Assisted Radiology and Surgery,* vol. 2, pp. 231-243, Feb. 2007.

[80] G. Hamarneh and T. Gustavsson, "Deformable spatio-temporal shape models: extending active shape models to 2D+ time," *Image and Vision Computing,* vol. 22, pp. 461-470, 2004.

[81] M. I. Miga, D. W. Roberts, F. E. Kennedy, L. A. Platenik, A. Hartov, K. E. Lunn, and K. D. Paulsen, "Modeling of retraction and resection for intraoperative updating of images," *Neurosurgery,* vol. 49, pp. 75-84, Jul. 2001.

[82] A. Cao, M. I. Miga, P. Dumpuri, S. Ding, B. M. Dawant, and R. C. Thompson, "Target error for image-to-physical space registration: Preliminary clinical results using laser range scanning," in *Medical Imaging*, San Diego,CA, USA, 2007.

[83] H. Chui and A. Rangarajan, "A new point matching algorithm for nonrigid registration," *Computer Vision and Image Understanding,* vol. 89, pp. 114-141, Feb. 2003.

[84] "http://www.farfieldtechnology.com/."

[85] P. Dumpuri and M. I. Miga, "Model-updated image guidance: a statistical approach to gravity-induced brain shift," in *Medical Image Computing and Computer-Assisted Intervention-MICCAI*. vol. 2878 Montreal, Canada: Springer-Verlag, 2003, pp. 375-382.

[86] J. M. Fitzpatrick, J. B. West, and C. R. Maurer, "Predicting error in rigid body point-based registration," *IEEE Transactions on Medical Imaging,* vol. 17, pp. 692-702, Oct. 1998.

[87] R. D. Bucholz, D. D. Yeh, J. Trobaugh, L. L. McDurmont, C. C. Sturm, C. Baumann, J. M. Henderson, A. Levy, and P. Kessman, "The correction of stereotactic inaccuracy caused by brain shift using an intraoperative ultrasound device," in *Proceeding 1st joint Conf. CVRMed and MRCAS*, Berlin, Germany, 1997, pp. 459-466.

[88] O. Wink, W. J. Niessen, and M. A. Viergever, "Multiscale vessel tracking," *IEEE Transactions on Medical Imaging,* vol. 23, pp. 130-133, Jan. 2004.

[89] I. Bitter, A. E. Kaufman, and M. Sato, "Penalized-distance volumetric skeleton algorithm," *IEEE Transactions on Visualization and Computer Graphics,* vol. 7, pp. 195-206, Jul. 2001.

[90] E. W. Dijkstra, "A note on two problems in connexion with graphs," *Numerische Mathematik,* pp. 269-271, 1959.

[91] "http://noodle.med.yale.edu/~chui/tps-rpm.html."

[92] S. Gold, A. Rangarajan, C. P. Lu, S. Pappu, and E. Mjolsness, "New algorithm for 2-D and 3-D point matching: pose estimation and correspondence," *Pattern Recognition,* vol. 31, pp. 957--964, 1997.

[93] P. Dumpuri, R. C. Thompson, B. M. Dawant, A. Cao, and M. I. Miga, "An atlas-based method to compensate for brain shift: Preliminary results," *Medical Image Analysis,* vol. 11, pp. 128-145, Apr. 2007.

[94] R. N. Dixon and C. J. Taylor, "Automated asbestos fiber counting," in *Inst. Physics*, Philadelphia, PA, USA, 1979, pp. 78-185.

[95] J. A. Sethian, *Level set methods and fast marching methods: evolving interfaces in computational geometry, fluid mechanics, computer vision and materials science*, 2 ed.: Cambridge University Press, 1999.

[96] D. L. G. Hill, C. R. Maurer, R. J. Maciunas, J. A. Barwise, J. M. Fitzpatrick, and M. Y. Wang, "Measurement of intraoperative brain surface deformation under a craniotomy," *Neurosurgery,* vol. 43, pp. 514-528, 1998.

[97] M. I. Miga, K. D. Paulsen, J. M. Lemery, S. Eisner, A. Hartov, F. E. Kennedy, and D. W. Roberts, "Model-updated image guidance: Initial clinical experience with gravity-induced brain deformation," *IEEE Transactions on Medical Imaging,* vol. 18, pp. 866-874, 1999.

[98] D. W. Roberts, M. I. Miga, A. Hartov, S. Eisner, J. M. Lemery, F. E. Kennedy, and K. D. Paulsen, "Intraoperatively updated neuroimaging using brain modeling and sparse data," *Neurosurgery,* vol. 45, pp. 1199-1207, Nov. 1999.

[99] O. M. Skrinjar, A. Nabavi, and J. S. Duncan, "Model-driven brain shift compensation," *Medical Image Analysis,* vol. 6, pp. 361-373, Dec. 2002.

[100] S. Ding, M. I. Miga, J. H. Noble, A. Cao, P. Dumpuri, R. C. Thompson, and B. M. Dawant, "Semiautomatic registration of pre- and postbrain tumor resection laser range scan images," *IEEE Transactions on Biomedical Engineering,* vol. 56, pp. 770-780, Mar. 2009.

[101] C. DeLorenzo, X. Papademetris, L. H. Staib, K. P. Vives, D. D. Spencer, and J. S. Duncan, "Nonrigid intraoperative cortical surface tracking using game theory," in

IEEE 11th International Conference on Computer Vision-ICCV, Rio de Janeiro, Brazil, 2007, pp. 1-8.

[102] S. Ding, M. I. Miga, R. C. Thompson, and B. M. Dawant, "Robust Vessel Registration and tracking of microscope video images in tumor resection neurosurgery," in *IEEE International Symposium on Biomedical Imaging: From Nano to Macro*, Boston, Massachusetts, USA 2009, pp. 1043-1046.

[103] P. Paul, A.Quere, E. Arnaud, X. Morandi, and P. Jannin, "A surface registration approach for video-based analysis of intraoperative brain surface deformations," in *Workshop on Augmented Environments for Medical Imaging and Computer-Aided Surgery* Copenhagen, Denmark, 2006.

[104] P. Paul, X. Morandi, and P. Jannin, "A surface registration method for quantification of intraoperative brain deformations in image-guided neurosurgery," *IEEE Transactions on Information Technology in Biomedicine,* vol. 13, pp. 976-983, Nov. 2009.

[105] G. K. Rohde, B. M. Dawant, and S. F. Lin, "Correction of motion artifact in cardiac optical mapping using image registration," *IEEE Transactions on Biomedical Engineering,* vol. 52, pp. 338-341, Feb. 2005.

[106] G. Wahba, *Spline models for observational data* SIAM: Society for Industrial and Applied Mathematics, 1990.

[107] S. Ding, M. I. Miga, R. C. Thompson, I. Garg, and B. M. Dawant, "Automatic segmentation of cortical vessels in pre- and post- tumor resection laser range scan images," in *Medical Imaging*. vol. 7261 Orlando, FL, USA: SPIE, 2009.